Integrated Silicon Photonic Circuit Simulation

by

Jonathan Leu

Submitted to the Department of Electrical Engineering and Computer Science
in partial fulfillment of the requirements for the degree of

Doctor of Philosophy

at the

MASSACHUSETTS INSTITUTE OF TECHNOLOGY

September 2018

Signature redacted

Author .....
Department of Electrical Engineering and Computer Science
August 31, 2018

Signature redacted

Certified by .....
Michael Watts
Professor of Electrical Engineering and Computer Science
Thesis Supervisor

Signature redacted

Accepted by .....
Leslie Kolodziejski
Professor of Electrical Engineering and Computer Science
Chair, Department Committee on Graduate Students

Integrated Silicon Photonic Circuit Simulation

by

Jonathan Leu

Submitted to the Department of Electrical Engineering and Computer Science
on August 31, 2018, in partial fulfillment of the
requirements for the degree of
Doctor of Philosophy

Abstract

Integrated silicon photonics is an exciting emerging technology, utilizing the high bandwidth and high timing resolution that optics provides in many applications. To maximize the benefits of these optical-electrical systems, tight integration of the electronic and photonic components are necessary. In light of this need, we've developed a Cadence toolkit library written in VerilogA that simulates both the amplitude and phase of optical signals, as well as optical-electrical interactions. The runtime is greatly improved by simulating the optical signal relative to a reference frequency, which is chosen to be close to the frequency range of interest. We have identified a set of fundamental photonic components, and described each at the physical level, such that the characteristics of a composite device will be created organically. We show that the simulated results match analytic solutions for simple devices like resonant ring filters and more complicated devices like single sideband modulators. Adding to this toolkit library, we then discuss devices that are required for handling more special cases, such as chromatic dispersion in the waveguide, and non-ideal optoelectronic devices. Finally, we demonstrate simulations of complicated systems such as WDM links and Pound-Drever-Hall loops. This will allow designers to unify our photonic device designing and modeling environment with circuit and system level design, giving us greater insight on the trade-offs that take place between the two realms.

Thesis Supervisor: Michael Watts
Title: Professor of Electrical Engineering and Computer Science

Acknowledgments

First of all I thank my wife Chen Shen, for putting up with my excuses for not finishing this years ago. She helped me realize that I've rarely had to do something that I've found challenging, and this thesis is orders of magnitude more difficult than anything I've done before. Her emotional support and constructive criticism has pushed me to engage this challenge head-on.

Next, I have great gratitude to my committee, for patiently helping me for so many years. To Vladimir, for staying long nights in the office with us prior to tapeout, for taking us out the ISSCC, for the weekly group meeting discussions, and so much more. My years in ISG gave me all the real world design experience I'm using today, and although many of our chips didn't turn out the way we've hoped, the process was an invaluable learning experience. To Mike, for orphaning me as Vladimir left to California, and guiding me towards completion. I understand that it's a lot to ask from you for accepting me as your student under such unusual circumstances, but you've willingly done so and I'm very grateful. And to Franz, although I wish we had a chance to interact more, your acceptance of my committee invitation gave me confidence that I indeed could complete this work. Much of this work was funded through DARPA EPHI.

Also, I'd like to thank my group leaders, Ted, Vyshi, Jeff, Dan, and Jon, at Lincoln Labs for accommodating my strange situation. Your interest in my progress has been helpful to me, as I often lose focus when I'm lagging behind. The interesting work I've been assigned to do at LL has also provided me motivation, to be finished with my thesis and fully concentrate on new things.

Finally, I'm thankful to my friends and family, in the US and abroad. My parents, which have been unconditionally loving to me. My close friends Samuel, Duane, Ted, and Albert for your companionship throughout the years. And special thanks to my son Jason, your arrival and constant growth reminds me daily that time is precious and doesn't stop. Every day at work I look forward to coming home and seeing you smile.

Contents

List of Figures

List of Tables

Chapter 1

Introduction

Integrated silicon photonics is an exciting emerging technology in many applications, such as photonic interconnects, telecommunication, signal processing, switched networks, imaging, displays, interferometry, photonics for millimeter-wave/radio-frequency systems, and analog-to-digital conversion, just to name a few [2] [3] [4] [5] [6].

These applications take advantage of using light signals in two closely related ways: (1) The ~200THz carrier frequency that infrared light provides, is orders of magnitude higher than what is used in electrical RF communications, and more than 10,000 times higher than what copper wires can provide for integrated circuit interconnects. This allows for communication bandwidth densities that greatly surpass electric wires, saving power, interconnect volume, die area, and cost. (2) The high frequency provides high resolution for timing purposes, that can be used to generate low phase noise frequency sources, while also reducing the required size and power.

To maximize the benefits of these optical-electrical systems, tight integration of the electronic and photonic components are necessary. Different integration approaches have been demonstrated, such as wire bond, bump bond, 3D stacking and monolithic integration [7] [8] [9], and the trade spaces and constraints vary greatly. Understanding the system as a whole allows the designer to choose the optimal integration solution, as well as guide the parameters in which individual device improvements should be made.

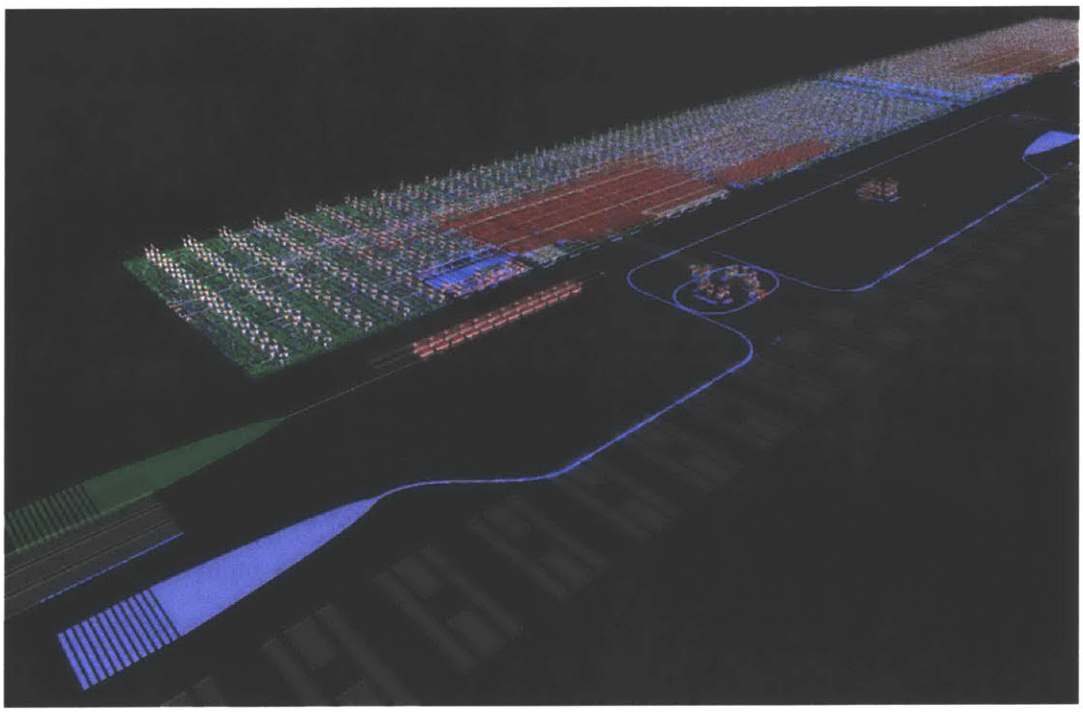

Figure 1-1: 3D rendition of CMOS circuits and photonic devices fabricated on the same wafer.

To analyze the behavior of such systems, we've developed a Cadence toolkit library written in VerilogA that simulates both the amplitude and phase of optical signals, as well as optical-electrical interactions. The runtime is greatly improved by simulating the optical signal relative to a reference frequency, which is chosen to be close to the frequency range of interest. We have identified a set of fundamental photonic components, and described each at the physical level, such that the characteristics of a composite device will be created organically. We show that the simulated results match analytic solutions for simple devices like resonant ring filters and more complicated devices like single sideband modulators, and demonstrate complicated systems such as WDM links and Pound-Drever-Hall loops. Adding to this toolkit library, we then discuss devices that are required for handling more special cases, such as chromatic dispersion in the waveguide, and non-ideal optoelectronic devices.

In the process of designing large scale silicon photonic integrated chips, we have modified existing system-on-chip design flows to accommodate the special design constraints of photonic components, and also have them compatible with our verification tools. This will allow us to unify our photonic device designing and modeling environment with circuit and system level design, giving us greater insight on the trade-offs that take place between the two realms.

Chapter 2

Electro-optical co-simulation for integrated CMOS photonic circuits with VerilogA

We present a Cadence toolkit library written in VerilogA for simulation of electro-optical systems. We have identified and described a set of fundamental photonic components at the physical level such that characteristics of composite devices (e.g. ring modulators) are created organically - by simple instantiation of fundamental primitives. Both the amplitude and phase of optical signals as well as optical-electrical interactions are simulated. We show that the results match other simulations and analytic solutions that have previously been compared to theory for both simple devices, such as ring resonators, and more complicated devices and systems such as single-sideband modulators. In later chapters we expand on this framework to include more detail, such as chromatic dispersion and non-linear behavior, to broaden the application scope.

2.1 Introduction

As integrated electronic-photonic circuits and systems increase in size and complexity, the need for a scalable design and verification infrastructure becomes imminent. In particular, the ability to jointly simulate the electrical and optical parts of large systems together, including noise and second-order effects, becomes critical. Substantial progress has been made towards a fully integrated design environment [10], but currently available simulation tools have yet to bridge the gap, in particular enabling scalable co-simulation of nonlinear, time-variant electronic-photonic devices and systems within the electronic design environment.

In particular, there is need for a joint system simulation code. Mature specialty software such as MEEP; Lumerical Device, Mode solutions, and FDTD solutions; Fimmwave; Sentaurus; and custom home-built scripts exist and are widely used to simulate photonic components at the physical, device level [11]. These programs mirror programs like Sentaurus, Atlas, and HFSS that are used to model electronic devices like MOSFETs at the physical, device level. Such programs allow for the maximum amount of detail and flexibility and the most accurate results, but are too computationally intensive to simulate the behavior of hundreds of devices, especially over "long" timescales. To solve this issue, the electronics industry has moved to code where the results from such detailed physical simulations are translated, via careful assumptions and approximations, into simple governing equations for each device - a behavioral/compact model - and used in a separate system simulation in a different programming framework - often in VerilogA or Spice. This greatly reduces the level of complexity and number of input parameters, allowing for fast simulation time and an easy way for the system designer to change the key parameters. The photonics industry is also moving in this direction. Our goal is to supplement the CMOS electronic device models with photonic device models that can be used within the IC design environment allowing for co-simulation of integrated electronic-photonic circuits and systems within the same tool. Because it is the preeminent IC design suite, we have chosen to do this in Cadence, though our code will also be compatible with any other simulator capable of using VerilogA (for

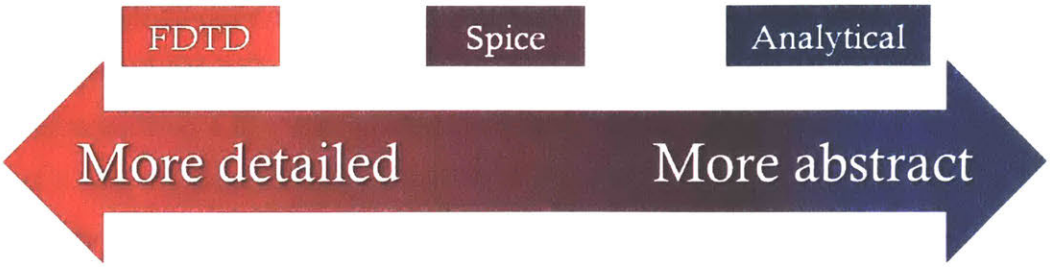

Figure 2-1: On the spectrum of models with varying levels of detail, spice simulations using behavioral models provides a balance between FDTD simulation and analytical modelling.

example, Mentor Graphic's Questa ADMS in Eldo).

Previous work has attempted to provide such behavioral macromodels for photonic devices. Several simulation tools or individual models have been presented [12–24]. Only some of these [12–15, 18, 19, 22–24] are able to properly capture transient behavior of all photonics components, handle frequency shifts and model both amplitude and phase effects (usually while removing the optical carrier for faster simulation time) and interference. Of this subset, all are written as standalone software and are therefore difficult to adapt into existing circuit design and layout infrastructures - especially with the transistor Spice or Spectre models provided in standard process design kits (PDKs). For example, OptiSpice [13, 14] is an excellent tool that correctly captures transient effects as well as amplitude and phase effects, but is written as proprietary standalone software suite. This is also true of [19, 22–24]. Lumerical's INTERCONNECT [18] is another excellent tool that that is written as proprietary standalone software. INTERCONNECT does provide hooks into Mentor's Pyxis platform, allowing for a joint electronics-photonic schematics to be laid out, but the simulator simulates the electronic and photonic parts separately - first doing one and then passing the output to the other - instead of doing a true joint simulation. Thus, making it inefficient to accurately capture feedback loops that incorporate both electronic and photonic components, or systems with a tight interplay between the electronic and photonic regimes. Such feedback is, for example, necessary when a monitor photodiode is being used to stabilize the frequency of a ring in a digital link, or in a Pound-Drever-Hall (PDH) locking loop [25] meant to stabilize the frequency of a laser. As the electronic-photonic systems grow in complexity it

becomes imperative for the modeling and simulation framework to support the co-simulation of nonlinear, time-variant electronic-photonic device interactions. This work presents a modeling and simulation framework capable of capturing these effects in a co-simulation that is not written as a standalone software suite but instead written in VerilogA [26], a language already incorporated within the standard circuit design infrastructure. By uniting these abilities it thus fills an important gap.

There have been some attempts to write photonic models into VerilogA, but all have fallen short of the designer needs listed above. [16] provides a basic framework for simulation at fixed wavelength, which is sufficient for simple links, but cannot capture the full behavior (especially phase phenomena, cross-talk, etc.) of more complex systems and devices like single-sideband modulators, coherent optics and wavelength division multiplexed waveguide links. Here, a higher fidelity representation of the underlying physics in each basic device is needed such that physical phenomena are organically generated simply from connecting basic components. [27] provides an overview of a similar approach. [28] presents an outline of a complete PDK similar to that created here, but the VerilogA models and infrastructure presented are overly simplistic for the type of models needed in many systems. For example, power and phase of the signals, are propagated around instead of real and imaginary parts. Working in power and phase creates convergence issues and prevents appropriate modeling of interference-based systems such as rings [13]. Indeed, no rings or similar systems are shown in that work. Models in [28] also do no appropriately account for the interaction of refractive and group index. The waveguide model simply outputs the input amplitude and phase delayed by a specified amount, but in reality the light output at the end of the waveguide will have an additional phase shift due to the waveguide refractive index. This effect is not captured and will lead to incorrect phases.

Probably most advanced among previous work is [21] which provides a nice set of VerilogA models for simulating a digital link, especially when it comes to underlying electrical structure for their photodiode. However, the transfer matrix approach to passives and rings is insufficient to appropriately capture non-linear or time-variant behavior of these components

that is present in many active multi-device systems.

Finally, there has been some work on models for individual devices, including [29–33]. However, it is desirable not to need to calculate the transfer functions of even moderately complicated devices by hand and program them in - it would be much nicer if such things could be automatically generated during simulation. So while, [31] provides an excellent model of a ring resonator it is not clear how useful it would be in allowing a system designer who knew little of optics to simulate a two-ring filter if need arose (for example, if lower cross talk between channels was needed). [31] also assumes that the optical frequency is passed around meaning models written in this manner cannot fully capture frequency shifts or multi-frequency interaction without additional code.

As shown in the following sections, our toolkit identifies a set of fundamental photonic components and describes each at the physical level such that the characteristics of composite devices are created automatically. It correctly captures both phase and amplitude effects and forward and backward propagating light as well as electro-optical interactions and transient effects, and can be used to model a wide variety of optical-electrical systems. Written in VerilogA, it is easily used in a wide variety of simulation types in existing electronic circuit design software and easily combined with CMOS transistor models provided by a foundry to allow for true co-simulation of electronic-photonic circuits. The next section goes through the simulation architecture and theory, and explains how the toolkit works. In section three, we demonstrate several passive device simulations and show that the simulated results match analytic solutions. Finally, section four does the same for active devices, in particular for a resonant modulator and a single sideband modulator.

2.2 Simulation Philosophy and Theory

There are a number of traits that are important for a useful, flexible, simulation platform. The first and most basic, is that it needs to be a full simulation toolkit, not simply a few device models. Strategies are therefore needed to address both how best to write specific models and how best to construct overall system architecture. On an architecture level, it is

trait #	description
1	easily combine with electronic standard cells
2	usable in a variety of simulation types (DC, ac, transient, etc)
3	computationally efficient
4	capture phase effects
5	support forward and backward propagation
6	handle arbitrary number of frequencies or WDM channels
7	capture appropriate electro-optic interactions
8	modular and flexible
9	organically generate behavior of composite devices
10	generally be elegant and easy to use

Table 2.1: Ideal traits for an integrated silicon photonic simulator.

desired that photonic models (1) easily combine with electronic standard cells, (2) be usable in a variety of simulation types (DC, ac, transient, etc), (3) be computationally efficient, (4) capture phase effects, (5) support forward and backward propagation, (6) handle arbitrary number of frequencies or WDM channels, (7) capture appropriate electro-optic interactions, (8) be modular and flexible, (9) organically generate behavior of composite devices -that is model building blocks so that, when combined, simulation outputs correctly capture complex behavior of the composite device or system without needing explicit input from the user or the creation of a new block, and (10) generally be elegant and easy to use.

2.2.1 Simulation with VerilogA

The first two goals on this list are automatically satisfied by the choice of VerilogA as the modeling language and the creation of the models in the Cadence framework. However, this choice adds a constraint of its own: (11) component models must exist only in the time domain, as VerilogA is a time domain modeling language. We next tackle desired trait number three: speed. Because optical frequencies are very large (200THz), a full Nyquist rate time domain simulation would take an extremely long time to run. However, in many applications, the bandwidth of interest is only on the order of 100GHz to a few THz. To exploit the relatively small bandwidth of interest, as shown in the equations later,

the optical responses are shifted and calculated relative to a reference frequency chosen by the user. The choice of reference frequency is arbitrary and does not need to be related to any property of the system. However, placing the reference frequency near the center of the desired bandwidth allows for the largest time steps, improving the speed of the simulation the most. Capturing the amplitude and phase effects of all the components in this smaller band is generally sufficient, and in cases where a larger bandwidth is needed that wider bandwidth can still be accurately simulated but with a corresponding increase in simulation time.

To accomplish this shift in a simple manner, the simulation is carried out using the analytic signal (that is only the positive frequency components of the real signal are retained), as it allows such a shift to be made solely by multiplying the signal by $e^{j\omega_R t}$ where ω_R is an arbitrarily chosen reference frequency. Working with the analytic signal also has the added benefit of making it easy to model phase effects, and satisfy desired trait number (4) - a phase or frequency shift is then just a multiplication by an exponential. However, it also means that the signal is no longer real. Because VerilogA usually works on the full real signal, and models phase changes by via time delays, it does not inherently support complex numbers. It is therefore necessary to add complex algebra into the program. We wrote a set of complex algebra functions as VerilogA modules for use inside our component blocks. A two signal bus is used to represent the real and the imaginary part. Real and imaginary parts are used as opposed to magnitude and phase to avoid the discontinuities in the phase signal when it wraps around 2π and the lack of a clearly defined phase at zero amplitude that can cause fatal numerical convergence issues when signals are added together during the modeling of optical inference effects, satisfying requirement (4). Expanding the representation into a four signal bus, two signals for the real and imaginary parts of the forward propagating signal and two for the backward propagating signal, allows us to satisfy requirement (5) and to capture behavior and errors caused by reflections as well as effects of having forward and backward propagation on the same waveguide if desired. To avoid passing the optical signals on these buses around as electrical voltages, an optical discipline is added to the discipline file.

The above approach to modeling signals automatically allows for multiple optical frequencies or spreads of frequencies to be modeled without any need to make explicit reference to these frequencies (desired trait (6)). Thus the optical signal can propagate through the system, including through frequency-selective components such as ring filters or frequency-changing elements such as single-sideband modulators, without any explicit reference made to the frequency of the light or the frequency transfer function of these elements. All the appropriate interactions will be generated naturally from the math in the component models. Finally, since VerilogA was developed for use in the electronics industry, adding electrical structures to optical components to model electro-optic effects (and satisfy desired trait (7)) is straightforward. The details of these implementations are described below.

The next item on our list of desired traits is for the code to be modular and flexible. While the architecture above helps with this, accurately modeling the optical components is also critical. In order to allow for maximum flexibility, applicability, and adaptability, optical devices are broken down into the most basic possible components (waveguides, couplers, phase-shifters, photodetectors, heaters, light sources, etc.), which, in turn, are modeled using simple equations that capture the important physics of the devices. This is similar to how models of diodes or transistors in the electrical domain rely on basic physical equations. The use of physical equations to capture photonic behavior allows for VerilogA blocks to be easily modified to add complexity and higher order effects. The blocks include both the optical responses, and, where appropriate, the electrical responses of these base components. More complicated structures, such as ring resonators, filters, and modulators are built out of these components, thus avoiding the need to specifically calculate a transfer function and create a model for each of these structures.

Some complex devices, such as modulators and ring resonators, may be used repeatedly within the same system. It is desirable not to have to recreate these small systems from scratch every time they appear. For combinations of components that are commonly used, schematic symbols can be created once and reused as black boxes wherever needed in a larger system. These symbols can have tunable parameters, so that the work of designing a

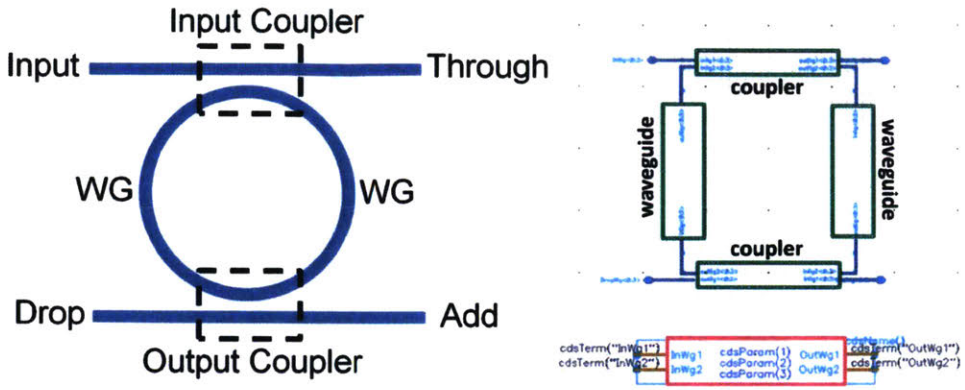

Figure 2-2: A ring resonator (left) is broken into components. The VerilogA modules for these components are laid out and connected in a schematic in Cadence (right-top). A schematic symbol is created to represent this schematic block (right-bottom). This symbol can be inserted wherever a ring is needed as opposed to having to redraw the middle block. Relevant variables are passed through this symbol to the underlying schematic.

single component can be leveraged to allow the simple use of a whole class of components in a design. Each symbol is still internally built out of our basic physical blocks - thus adaptability and flexibility is maintained. Such symbols can also be useful for holding more complicated components that might not be repeated often so that the top level design looks clearer. If necessary, the designer can drill down the hierarchy of abstract symbols to view and modify their design. Figure 2-2 illustrates the creation and inside of such a schematic symbol for a ring resonator.

2.2.2 Wave Representation and Waveguide Equation

The most basic building block of optical systems is the optical waveguide. In order to represent this component in VerilogA, it is necessary to develop a time domain representation of the waveguide transfer function. As mentioned above, the physical electric field is real, but many operations are difficult to do on the full real signal. To get around this, one can take advantage of the fact that real signals are symmetric around zero in the frequency domain. We can therefore ignore all the negative frequencies without loss of information. An inverse Fourier transform can then be done to get back to the time domain, where the result will

be a complex signal. In the signal processing literature, this is called the *analytic signal* (see [34,35]) and is formally defined in equation 2 in [36] as:

$$\mathbb{X}_a(\omega) = \begin{cases} 2\mathbb{X}(\omega) & \text{for} \quad \omega > 0 \\ \mathbb{X}(\omega) & \text{for} \quad \omega = 0 \\ 0 & \text{for} \quad \omega < 0 \end{cases} \tag{2.1}$$

where $\tilde{x}(t)$ is the analytic signal of $x(t)$, and $\mathbb{X}(\omega)$ is the Fourier transform of $x(t)$, $\mathbb{X}_a(\omega)$ is the Fourier transform of $\tilde{x}(t)$. Following this definition, it is shown that $\tilde{x}(t) = x(t) + j\hat{x}(t)$, where $\hat{x}(t)$ is the Hilbert transform of $x(t)$. As an example, if $x(t) = cos(\omega t)$, then $\hat{x}(t) = cos(\omega t - \pi/2) = sin(\omega t)$, resulting in $\tilde{x}(t) = x(t) + j\hat{x}(t) = cos(\omega t) + jsin(\omega t) = e^{j\omega t}$.

The use of the analytic signal is often simply assumed implicitly in the electromagnetic literature (see, for example, [37, 38]). At the end, to recover the real, observable signal one can simply take the real part, which happens at the input of a photodiode, for instance. Therefore, the sampled, complex, analytic signal is passed through all the components. Note that, because the light source models output the time-domain analytic signal representation of the laser output to start with, there are no Fourier transforms in the code, nor is there any explicit tracking or specification of light frequencies; all the components are operated in the time domain as required by the VerilogA infrastructure simulator.

The analytic representation of the electric field at the start of the waveguide ($z = 0$) is $\tilde{E}(0,t)$. Assuming that the signal bandwidth is much less than the laser frequency, the wave equation, derived from Maxwell's equations, says that at a location z, in the waveguide the field is equal to:

$$\begin{aligned} \tilde{E}(z,t) &= \int_{-\infty}^{\infty} \mathbb{E}(0,\omega) e^{-j\beta z + j\omega t} d\omega \\ &= \int_{0}^{\infty} \mathbb{E}(0,\omega) e^{-j\beta z + j\omega t} d\omega \end{aligned} \tag{2.2}$$

where $\beta = \beta(\omega)$ is the wavevector in the waveguide and the second equality follows

because there are no negative frequency components in our analytic representation. We note that the measurable E-field would be the real part of $\tilde{E}(z,t)$. In order to avoid simulation at the optical time step, a reference frequency ω_R is chosen such that $\omega = \omega_R + \Delta\omega$ and the signal is shifted down by this frequency. To do this, $\beta(\omega)$ is Taylor expanded to the first order around this frequency yielding:

$$\beta(\omega) \Rightarrow \beta(\omega_R) + \Delta\omega \frac{\partial\beta}{\partial\omega}\bigg|_{\omega=\omega_R} \tag{2.3}$$

For simplicity, we will ignore chromatic dispersion and higher order effects for now. Methods for handling these effects will be discussed later on. Note that $\Delta\omega\frac{\partial\beta}{\partial\omega}\big|_{\omega=\omega_R} = 1/v_g$, where v_g is the group velocity of light in the waveguide at the reference frequency and is equal to c/n_g, where n_g is the group index. This brings us to:

$$\tilde{E}(z,t) = \int_0^\infty \mathbb{E}(0,\omega_R+\Delta\omega)e^{-j\beta(\omega_R)z - j\frac{\Delta\omega}{v_g}z + j(\omega_R+\Delta\omega)t}d\omega \tag{2.4}$$

We further note that we can define a function $\mathbb{E}_{shift}(z,\Delta\omega) = \mathbb{E}(z,\omega_R+\Delta\omega)$ which down-shifts the frequency spectrum by the reference frequency. The inverse Fourier transform $\tilde{E}_{shift}(z,t) = \mathcal{F}^{-1}\{\mathbb{E}_{shift}(z,\Delta\omega)\}$ is also known as the *complex envelope* or *complex baseband* of $E(z,t)$. In one special case, the reference frequency can be thought of as a carrier frequency and $\tilde{E}_{shift}(z,t)$ as the complex envelope/baseband, but it is important to remember that the reference frequency does not have to be the center (or necessarily any) frequency of the propagating light. Also, if down-shifted by too much, we might introduce non-zero values in the negative frequencies of $\mathbb{E}_{shift}(z,\Delta\omega)$. Although there is no loss of information, restoring the real-valued original signal is no longer a simple matter of just extracting the real component of the analytic signal. To avoid this situation, ω_R is chosen such that the entire bandwidth of $\mathbb{E}_{shift}(z,\Delta\omega)$ is positive.

Replacing $\mathbb{E}$ with $\mathbb{E}_{shift}$, and the variable of integration changed to $\Delta\omega$, we arrive at:

$$\begin{aligned}\tilde{E}(z,t) &= e^{-j\beta(\omega_R)z+j\omega_R t}\int_{-\omega_R}^{\infty}\mathbb{E}_{shift}(0,\Delta\omega)e^{-j\frac{\Delta\omega}{v_g}z+j\Delta\omega t}d\Delta\omega \\ &= e^{-j\beta(\omega_R)z+j\omega_R t}\int_{-\infty}^{\infty}\mathbb{E}_{shift}(0,\Delta\omega)e^{-j\frac{\Delta\omega}{v_g}z+j\Delta\omega t}d\Delta\omega \end{aligned} \tag{2.5}$$

where, again, the second equality follows from the fact that there are no frequency components between $-\omega_R$ and $-\infty$. As can be seen, this integral is just the Fourier transform of $\tilde{E}_{shift}(z,t)$. Thus:

$$\tilde{E}(z,t) = e^{-j\beta(\omega_R)z+j\omega_R t}\tilde{E}_{shift}(0,t-z/v_g) \tag{2.6}$$

The field at a point, z, in the waveguide can also be expressed as:

$$\tilde{E}(z,t) = \int_{-\infty}^{\infty}\mathbb{E}(z,\omega)e^{j\omega t}d\omega = \int_{0}^{\infty}\mathbb{E}(z,\omega)e^{j\omega t}d\omega \tag{2.7}$$

via the definition of a Fourier transform and remembering that we are ignoring the negative frequencies. The reference frequency can be pulled out in this case as well, as was done above:

$$\begin{aligned}\tilde{E}(z,t) &= \int_{0}^{\infty}\mathbb{E}(z,\omega_R+\Delta\omega)e^{j(\omega_R+\Delta\omega)t}d\Delta\omega \\ &= e^{j\omega_R t}\int_{-\infty}^{\infty}\mathbb{E}(z,\omega_R+\Delta\omega)e^{j\Delta\omega t}d\Delta\omega \\ &= e^{j\omega_R t}\int_{-\infty}^{\infty}\mathbb{E}_{shift}(z,\Delta\omega)e^{j\Delta\omega t}d\Delta\omega \end{aligned} \tag{2.8}$$

Again, at the result is a Fourier transform of $\tilde{E}_{shift}(z,t)$, yielding:

$$\tilde{E}(z,t) = e^{j\omega_R t}\tilde{E}_{shift}(z,t) \tag{2.9}$$

Combining equations 2.6 and 2.9 and recalling that $v_g = c/n_g$ gives:

$$\tilde{E}_{shift}(z,t) = e^{-j\beta(\omega_R)z}\tilde{E}_{shift}(0, t - \frac{zn_g}{c}) \tag{2.10}$$

We note that $\tilde{E}_{shift}$ is the analytic signal passed around in our code, and it has been downshifted by the reference frequency. So, the output at time t of a waveguide of length L is the input at time $t - n_g L/c$, and phase shifted by $e^{-j\beta(\omega_R)L}$. Or in other words, the waveguide takes whatever signal is coming in, phase shifts it by $e^{-j\beta(\omega_R)L}$, and delays it by $t - n_g L/c$ before sending it out. A propagation loss term, α_{field}, is also added and thus the waveguide is modeled in VerilogA as shown in Figure 2-3.

2.2.3 Other Basic Devices

The equations governing other components can be similarly derived. Phase-shifters can be modeled as waveguides where the effective group and refractive index, as well as the loss, vary, possibly nonlinearly, with applied voltage. The code for such an optically non-ideal, but electrically ideal phase shifter is, thus, very similar to that derived for a straight waveguide. The main section of this code is given in Figure A-1 in the Appendix.

Here, the wavevector is given by $\beta(V) = (2\pi/\lambda)n_r(V)$, where n_r is the refractive index as a function of voltage, and is given, for example, by: $n_r(V) = n_0 + n_1 V + n_2 V^2 + n_3 V^3 + n_4 V^4 + n_5 V^5$, and where the loss as a function of voltage is similarly given by $\alpha_r(V) = \alpha_0 + \alpha_1 V + \alpha_2 V^2 + \alpha_3 V^3 + \alpha_4 V^4 + \alpha_5 V^5$. Such a phase-shifter definition is general and can be used regardless of what electrical or thermal effect is being used to generate the index and loss change. However, in practice, the response of the underlying electrical structure, in addition to the optical response, is often critical for simulations, particularly when driving

```
`include "../../../../cad/constants.vams"
`include "../../../../cad/disciplines.vams"

module Optical_Waveguide(inLight, outLight);
    inout  [0:3]  leftLight; // [0:1] is left side input, [2:3] is left side output
    inout  [0:3]  rightLight; // [0:1] is right side output [2:3] is right side input. optical
    [0:3] rightLight, leftLight;

    // Physical Design Parameters, all units in SI
    parameter real L = 0.0005;          // length
    parameter real ng  = 4.1963;        // group index
    parameter real np = 2.1;            // refractive index
    parameter real alphaA = 287.6;      // loss
    parameter real G_freq = 1.93e14;    // reference frequency parameter passed in from
    top level simulation

    // initialize intermediate points
    optical [0:1] rightOutput;
    optical [0:1] leftOutput;
    optical [0:1] transfer; // for calculated phase-shift and amplitude change
    optical [0:1] transferCart; // for above in real and imaginary forms

    pol2cart convs1(transfer, transferCart); // convert waveguide effect to real and
    imaginary parts
    cartmul mulout1(transferCart, leftLight[0:1], rightOutput);  //Calc outputs
    cartmul mulout1B(transferCart, rightLight[2:3], leftOutput);

    analog begin
        //calculate phase-shift and amplitude change in polar coordinates
        E(transfer[0]) <+ (-L*np*2*`M_PI*G_freq/`P_C)%(2*`M_PI);
        E(transfer[1]) <+ exp(-alphaA*L);

        // Output delayed signals
        E(rightLight[0]) <+ absdelay(E(rightOutput[0]), L*ng/`P_C);
        E(rightLight[1]) <+ absdelay(E(rightOutput[1]), L*ng/`P_C);
        E(leftLight[2]) <+ absdelay(E(leftOutput[0]), L*ng/`P_C)
        E(leftLight[3]) <+ absdelay(E(leftOutput[1]), L*ng/`P_C);
    end
endmodule
```

Figure 2-3: VerilogA waveguide model code. "pol2cart" is used to convert the waveguide transfer function from the amplitude and phase representation to the real and imaginary one. Note that the input and output optical signals are never converted to the amplitude and phase representation, thus avoiding any convergence issues. "cartmul" is used to do complex multiplication on the real and imaginary signals.

circuitry is being designed. Reverse bias silicon diode phase shifters that rely on the plasma dispersion effect to create a phase shift are commonly used in integrated photonic platforms. These phase shifters can be modeled like the non-ideal phase shifter above, but with the addition of the underlying electrical diode structure, as shown in the Figure A-2 code in the Appendix. This allows for the capture of electrical effects (such as speed limitations due to diode resistance and capacitance), as well as optical effects (such as speed limitations due to the optical lifetime of signals in resonances).

Resistance based phase-shifters, in which resistive heating is used to generate a phase-shift are also common. Electrically the device can, of course, be modeled as a resistor. Optically, the correct way to implement such an integrated heater is to first integrate the electrical power put into the device minus the thermal power dissipated from the device, then proceed to calculate the phase shift as a function of the device's temperature. To do this we create a thermal discipline that keeps track of temperature. Here the index change is given by:

$$\Delta n = n_T T \tag{2.11}$$

where $n_T = \frac{\partial n}{\partial T}$ is the refractive index change with temperature, and T is the temperature, calculated by:

$$T(t_1) = T_0 + \frac{\int_0^{t_1} Z_T P(t) - h(T(t) - T_0)dt}{C_{thermal}} \tag{2.12}$$

where Z_T is the thermal impedance, P is the electrical power (given by $P = V^2/R_0$ where V is the applied voltage and R_0 is the electrical resistance), T_0 is the temperature when the potential across the resistor is zero, h is a heat transfer coefficient, and $C_{thermal}$ is the thermal capacitance. This method correctly takes into account the transient behavior of the heating element, which limits the thermal bandwidth of the device. The relevant lines of code are reproduced in the Figure A-3 in the Appendix. The above phase-shifters as well as several other flavors (e.g a forward-biased diode shifter) have been implemented in our code. Alternatively, if multiple devices are thermally coupled (intentionally or parasitically),

the heat generation can be brought out of the device and be represented by the thermal equivalent of an RC network.

Waveguide couplers are modeled in our code as point couplers: a fraction of the light is transferred, with appropriate phase shift, to the adjacent waveguide and the rest remains behind. Both adiabatic 3dB couplers and directional or ring couplers, where the field coupling fraction is specified, have been implemented. The code for a directional coupler is shown in Figure A-4 in the Appendix. In this case the light entering through one port is split into two output ports, with field coupling, kappa, and implements the well known equations given in [39], which are valid in the time domain: $E_{out,top} = \frac{E_{in,top}}{\sqrt{2}} + \frac{E_{in,bottom}e^{-j\pi/2}}{\sqrt{2}}$.

More information on the theory of directional couplers can be found in [39], and on adiabatic couplers can be found in [40]. Our model does not currently include any propagation delays or loss through the coupler, but these could easily be added either directly into the model or by placing an appropriate waveguide block before or after the device ports.

Similar principles are used to write models for photodetectors. In the ideal photodetector, the instantaneous optical intensity is simply measured and transferred to the electrical domain. Such an ideal diode can be modeled by specifying a responsivity, R, and setting $I_{out} = RP$, where I_{out} is the output current, and P is the input optical power. Photodiodes form a common class of integrated photodetectors. In this non-ideal case, the underlying diode structure is included to allow for electrical responses such as frequency roll-off and dark current to be captured. Due to the short length of the device, which can be as little as $4\mu m$ [41], it does not make sense to include the optical delays in the device model. The code for such a photodiode including electronics is shown in Figure A-5 in the Appendix.

We note that parameters like photodiode quantum efficiency are folded into the responsivity term and therefore do not need to be specified explicitly [42]. We further note that, while the included diode limits the electrical bandwidth of the device, the above code specifies a photodiode of infinite optical bandwidth as it captures the input power at all optical frequencies. Because of this infinite optical bandwidth, it is not necessary to consider the absolute frequency in this first order model. In order to place an optical limit on the bandwidth

of light detected, one can place an additional filter in the code between the original calculation of the optical power and the specification of the electrical current. This filter, which can also be shifted down in frequency and specified in relation to the reference frequency, can cut out wavelengths to which the detector is not sensitive.

Other useful components, such as continuous-wave (CW) lasers and Gaussian pulse emitting lasers, as well as debugging components, such as phase detectors, are also included in our toolkit. Once this simulation framework has been established and these simple component models, which we will now refer to as optical primitives, have been implemented, complex optical systems can be built and combined with CMOS device cells to model complicated systems in a truly-joint fashion.

2.3 Verification with Basic Composite Devices

Because the optical components are implemented as basic physical primitives they must be combined together to create full devices. Our simulation technique can be used to model very complicated devices and systems that are beyond the capabilities of more traditional optical simulation techniques. To validate our technique, however, we also modeled several devices simple enough for existing optical simulation techniques to handle and found that our results matched. Since our codes using these traditional techniques have previously been validated against experiments (see, for example, [43]), this is equivalent to experimentally validating our technique.

The first of these devices is a ring resonator, which is created out of a waveguide connected in feedback between two ports of a coupler. A diagram showing this system is given in Figure 2-4(a). The frequency response of the ring resonator is shown in Figure 2-4(c). Because this is a time domain code, to get the frequency response it was necessary to sweep the input CW laser frequency. This is done by having a voltage controlled phase ramp inside the laser (as a phase ramp in the time domain corresponds to a frequency shift in the frequency domain) and running multiple DC simulations with different voltage inputs to this phase ramp. A diagram of the full simulated system is shown in Figure 2-4(b) The

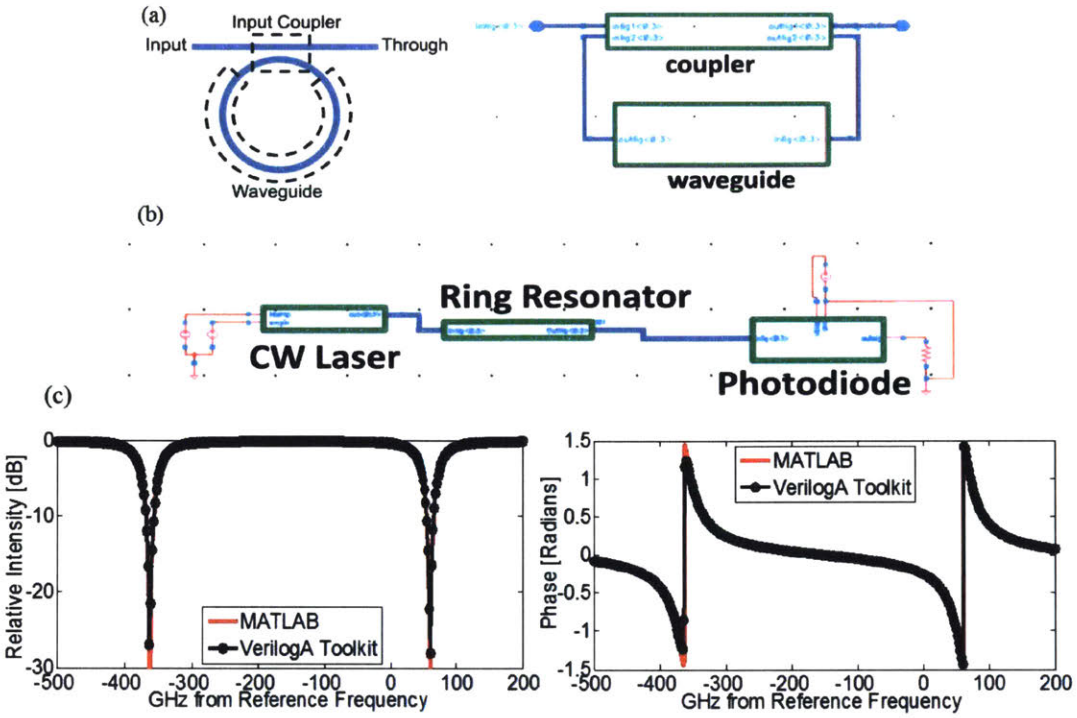

Figure 2-4: (a) Diagram showing the components of a ring resonant filter and accompanying layout using our toolkit in Cadence Virtuoso. (b). A full link schematic including laser and photodetector is created to simulate the performance of the device. (c). Amplitude and phase response of the ring showing good agreement between VerilogA simulations and MATLAB transfer function code.

obtained spectral response of the ring is compared and shown to match well to the results from an existing transfer matrix code implemented in MATLAB.

We can further compare the results to theoretical expectations. The free spectral range (FSR) of a ring resonator can be analytically found to be $FSR = \frac{c}{n_g L}$, where c is the speed of light in vacuum, n_g is the group index, and L is the effective waveguide path length. The results in Figure 2-4(c) are for a SiN waveguide 200nm tall and 1μm wide that has a group index of 1.72 and is formed into a ring with a 66μm radius. The expected FSR is therefore 423GHz, as it is in the simulation. The effective refractive index of this waveguide is 1.516. We therefore expect the closest resonant frequency to 1550nm (=193THz), the reference frequency used in this simulation, to be at $\lambda = n_{eff}L/m$ =1549.5nm or 60.9GHz above the reference frequency. This value is also the same as that seen in Figure 2-4(c). Finally, the half

width at half maximum (HWHM) of the resonance was found to be 17.4GHz, also exactly what is expected given the input waveguide field loss, α, or 312.7m^{-1} and that HWHM$= \frac{c\alpha}{n_g \pi}$. Moreover, not only does the amplitude response of the ring match that expected, but the phase response (measured using a debug block that outputs the instantaneous phase), shown in Figure 2-4(c) also matches, going to $\pm\pi/2$ as the laser frequency approaches the resonant frequency. Thus, it can be seen that our VerilogA toolkit also captures phase effects correctly.

To further expand on this example we can consider the case where the ring has a drop port and the case of a two ring filter. Both modifications are very simple to make using our toolkit, making it easy for designers to change systems on the fly. We compare both cases below to the results of transfer matrix codes implemented in MATLAB. No new calculations or equations were required when using our VerilogA toolkit; however, the new transfer matrices needed to be calculated and input into our MATLAB codes.

To add a drop port, we simply add an output coupler as shown in Figure 2-5(a). One can then use this model in a system or to explore how to best optimize the component for a desired application. For example, in a single ring resonator with drop port, it has been shown [44] that, given a target HWHM, the drop port output intensity is maximized when the input and output coupler coefficients are equal. On the other hand, the through port intensity is minimized at critical coupling where the input coupler coefficient equals the sum of the waveguide and output coupler loss. VerilogA simulations of both cases are shown in Figure 2-5(b) and compared to transfer matrix codes, where we observe excellent agreement.

The two-ring series filter case is shown in Figure 2-6(a). As can be seen, creating this case with our toolkit is similarly straightforward. One simply adds a second ring to the bottom of the first. Further, basic schematic symbol of this and other ring filters exist in our tool kit making it even easier for a designer to switch filters to tune the roll-off, ripple, passband width, or other figures of merit, and re-simulate. Two-ring filters are often helpful in systems such as switching matrices where having a wider and flatter passband allows for a wider bandwidth signal to propagate through. However, because two resonances are combined to make the larger resonance, ripples are often introduced into the passband. All

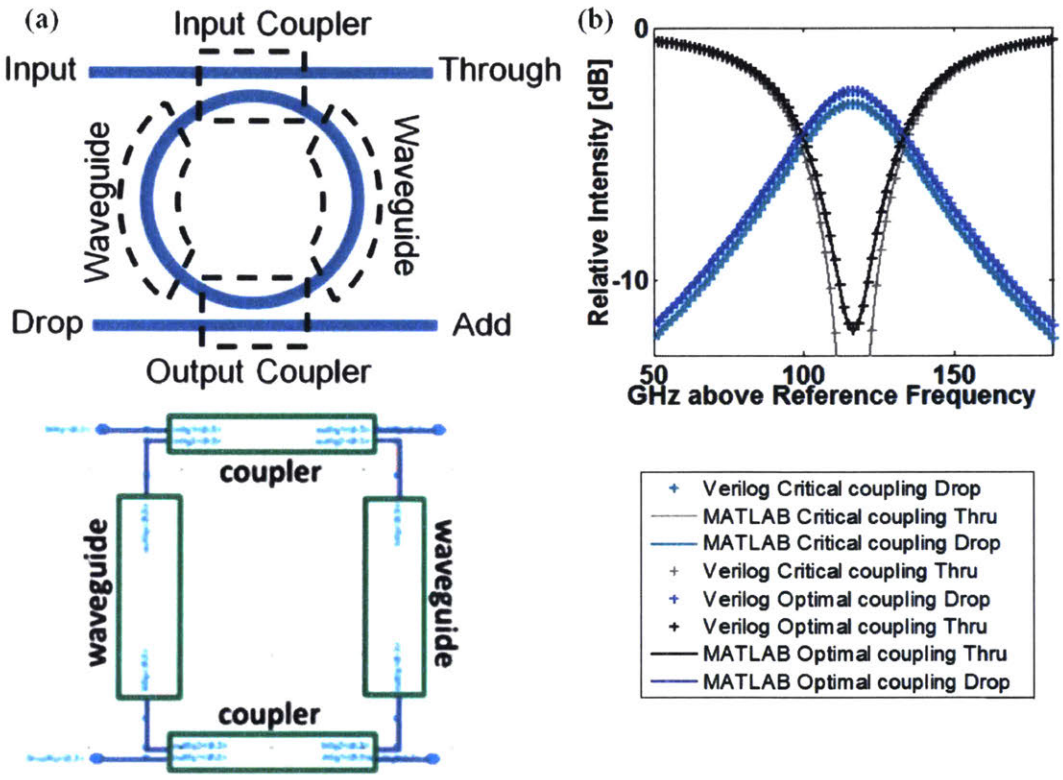

Figure 2-5: (a). Diagram showing the components of a ring resonant filter with drop port and accompanying layout using our toolkit in Cadence Virtuoso. (b). Amplitude response of the ring showing output intensity in the through and drop port. One can see that the critical coupling has better extinction in the through port but less power in the drop port output, while matched coupling has worse extinction and higher drop port output power, as expected. Note that the waveguide loss was exaggerated in these cases to highlight the difference.

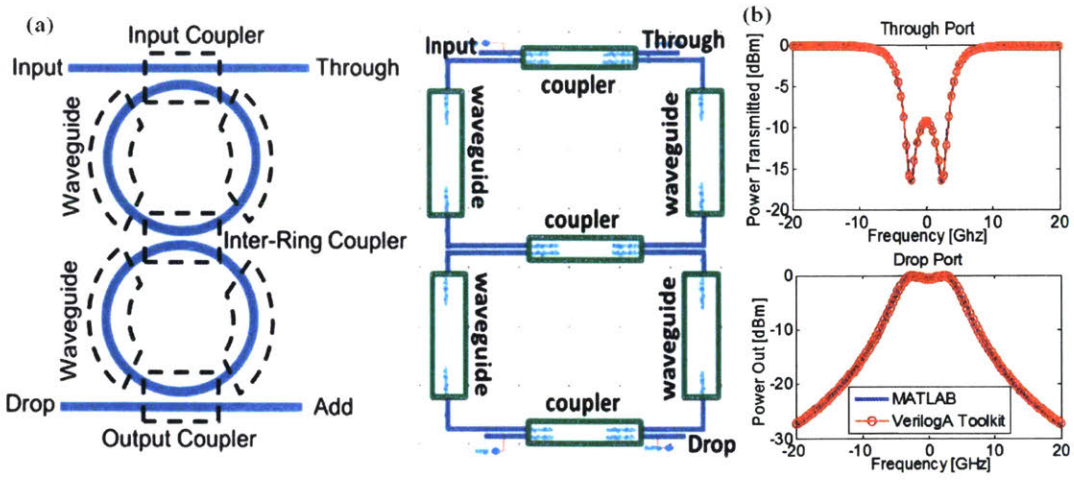

Figure 2-6: (a). Diagram showing the components of a two ring series filter with drop port and accompanying layout using our toolkit in Cadence Virtuoso. (b). Amplitude response of the ring showing output intensity in the through and drop port showing good agreement between VerilogA simulations and MATLAB transfer function code.

these effects are captured in the simulation output which is shown in Figure 2-6(b) and also matches exactly the expected output calculated via transfer matrices in MATLAB.

The above demonstrations all involve passive devices, but simulating active devices in our toolkit is equally straightforward as is illustrated in the next section.

2.4 Verification with Active Devices

Active devices can be built in our tool kit in a way exactly analogous to the passive devices described above. In this section we will demonstrate the design and simulation of a ring modulator of the type often proposed for digital communication links [43]. We will also demonstrate the simulation of a single sideband modulator. Single sideband modulators are often used to create frequency shifts, and are important for both analog applications, such as arbitrary waveform generators, and digital applications, like dense wavelength division multiplexing systems.

A ring modulator can be made in our toolkit by replacing the waveguide component with a phase shifter in the resonant ring (see Figure 2-7(a)). As described above, the phase

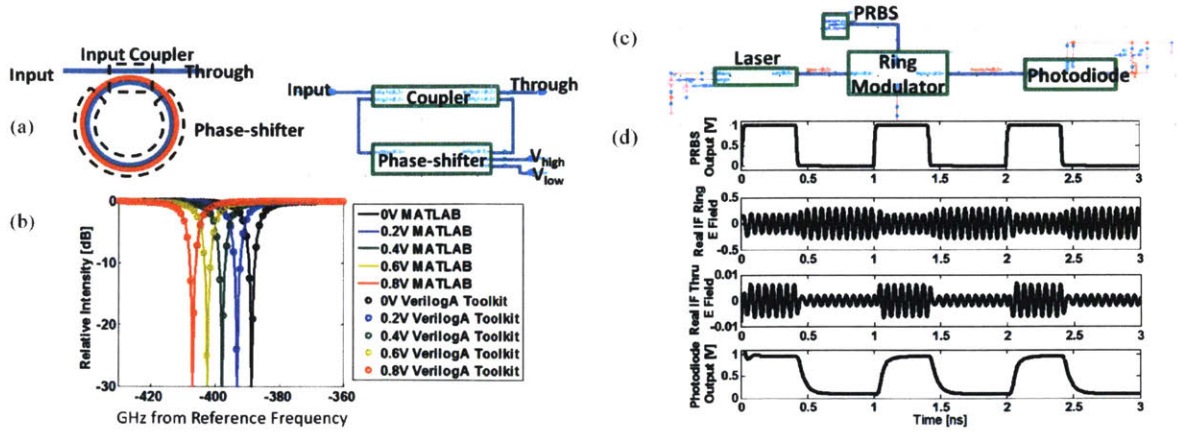

Figure 2-7: (a) . Diagram showing the components of a single ring modulator and accompanying layout using our toolkit in Cadence Virtuoso. (b). Modulator amplitude transfer function as a function of applied phase-shifter bias, showing good agreement between VerilogA simulations and MATLAB transfer function code. (c). Schematic of full single-wavelength digital link. Output from a CW laser is fed into a ring modulator driven by a PRBS source. The output of the modulator is sent to a photodiode. (d). Simulation output, showing electrical driving voltage, field amplitude inside the ring, through port field amplitude, and output of photodiode.

shifter allows an input voltage to change the refractive index, group index, and loss of the waveguide, and thus the location of the resonance frequencies in a ring modulator. The shift in frequency of the resonance location of the modulator with voltage is shown in Figure 2-7(b). The simulation is done for a five micron radius disk modulator made in a 220nm tall silicon layer. The output is compared to calculations done in MATLAB. Again, it matches the expected output.

However, the transient output, and not the DC output, is often what is of real interest in modulators. It is easy to simulate this using our toolkit: the input laser is simply set at one wavelength and the input voltage to the phase shifter changed from a DC to a pseudo-random-bit-sequence (PRBS) source. The layout of this link is shown in Figure 2-7(c), and the output in Figure 2-7(d). As can be seen, when the input voltage is low, the optical amplitude inside the ring modulator is high and the through port output is low. Conversely, when the input voltage is high, and the resonance is shifted away from the laser frequency, the amplitude inside the ring is low, and the through port output is high, as expected.

Further, we can clearly see the usefulness of a transient simulation by noting the roll-off in the output through the modulator.

In this simulation, it is the optical time constant (the speed at which the optical mode in the resonator can ring down), and not the electrical time constant of the modulator or photodetector diodes (the speed at which the index can be changed or the intensity detected) that ultimately limits device speed. If the optical time constant were shorter (the ring were lower Q), or the electrical circuit slower, the frequency roll-off would be caused by the electronics instead, and this would also be captured by the simulation. Because the code models the optical interference inside the ring with each time step, all these transient phenomena are neatly captured without any explicit modeling. No changes to the inside of the blocks or the overall system code are needed; we just have to draw the schematic for the desired systems and run the preferred simulation.

An example of a device where phase and frequency effects are of importance is a single sideband modulator (SSB). SSBs are important for many analog applications as well as for high density WDM communication systems as they allow for closer channel spacing and lower power [45]. Additionally, the same topology can be used to transmit data using more complicated modulation formats (BPSK, QAM, etc). Correctly modeling the phase effects and delays of components is vital to simulating single sideband operation, and as we will demonstrate below, our VerilogA Toolkit is capable of doing this. We note again that the transfer function of the SSB is never calculated explicitly; instead the correct output is generated automatically from the combination of basic optical blocks.

A schematic layout of the SSB topology using our VerilogA toolkit is shown in Figure 2-8(a). The SSB is made from two nested Mach-Zehnder modulators (MZMs), with each MZM composed of the coupler and phase-shifter primitives, and generates a single sideband carrier suppressed signal. To do so each individual MZM is biased using a heater at the zero output point (thereby suppressing the carrier), and driven in push-pull. The electrical RF input signals to each modulator are out of phase by $\pi/2$, such that one arm receives a cosine modulation and the other a sine modulation. An extra $\pi/2$ phase added by heaters

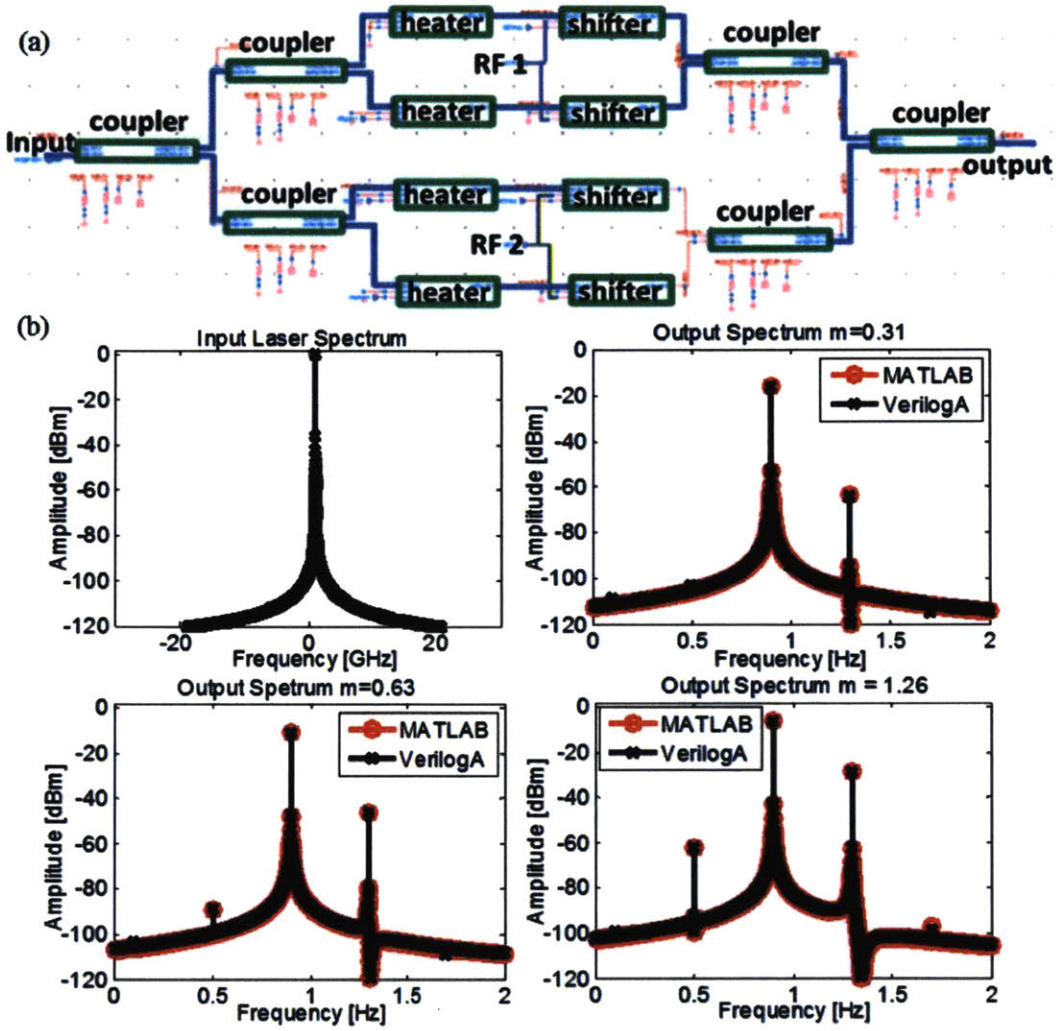

Figure 2-8: (a.) Diagram of single side band modulator component system and accompanying layout using our toolkit in Cadence Virtuoso using basic components (couplers, heaters, phase-shifters). (b) Fourier transform of SSB output as a function of modulation amplitude. Input CW signal is shown in black in upper left. Following graphs show steadily increasing modulation depth. Increase in power transferred to desired sideband and accompanying increase in power in undesired harmonics is seen. VerilogA and MATLAB code show good agreement.

to one of the MZM signals therefore allows one sideband to cancel and the other to add. Which sideband is kept depends on which arm receives the extra $\pi/2$ phase relative to which receives the sine (vs. the cosine) RF input signal. For more detail about SSB operations see [45]. This surviving sideband is the output of the device, and is given by $f_{out} = f_{opt} - f_{rf}$ or $f_{out} = f_{opt} + f_{rf}$, where f_{opt} is the original optical frequency and f_{rf} is the modulation frequency. We choose to keep the lower sideband.

The output of the simulation using our VerilogA toolkit is shown in Figure 2-8(b). Here a CW laser block inputs a CW signal to the SSB. Since our code operates entirely in the time domain, the Fourier transform was computed in a post-processing step. In a real system model, the time domain output samples would simply be passed on to the next block with no transform necessary. To verify that the VerilogA model is in fact working correctly, we compare it to the output of our MATLAB system code for this device. As above, we have previously verified this MATLAB code against experimental results, and it has been found to match well. Figure 2-8 shows the case of a 0dBm laser output that is 1GHz from the reference frequency and is modulated at 100MHz to yield a sideband frequency of 900MHz. The presence of a single, frequency shifted tone at the output can clearly be seen -the carrier and unwanted sideband are well suppressed in all cases. As the modulation depth, m, increases the amount of power transferred to the desired sideband increases as does the relative height of the higher harmonic distortions. These last are caused by the increasing interaction with the nonlinear portion of the MZM transfer function and are given by the Bessel function expansion for the sine within the sine [45]. All these expected effects can be clearly seen in the output spectra shown in Figure 2-8(b). Further, there is very good agreement between the MATLAB and the VerilogA models in all cases, indicating that our VerilogA framework is working correctly. It is worth noting that writing and running the MATLAB code took more time and was more complicated than setting up and running the SSB modulator schematic in VerilogA, thus demonstrating the convenience and one of the benefits of having a single, flexible simulation platform.

2.5 Conclusions

A Cadence toolkit, written in VerilogA, for simulating optical devices in conjunction with electronic circuits has been presented and verified. To correctly capture phase-phenomena and interference effects while avoiding numerical instabilities, the optical electric field is represented by the real and imaginary parts of both a forward and backward propagating signal. Relevant optical electrical interactions are captured. To minimize run time and simplify coding, the analytic signal representation is used, and the simulations are carried out relative to an arbitrarily chosen reference frequency. A set of fundamental photonic components are identified, and each is described at the physical level, such that the characteristics of any composite device will be created organically. We show that resonant effects in composite devices such as ring filters and modulators, and phase-effects in composite devices like single sideband modulators are correctly, organically captured by these models.

Building upon this foundation, we can include device variants that incorporate more detailed physical attributes to its behavioral equations. Adding complexity into device models also adds to the simulation run-time, so the user can decide which level of detail is sufficient for each device in a given system. Electro-optical device models have been discussed [46], and for lumped components, the behavioral equations are a straight forward application of the device physics involved. Modeling difficulty arises when we wish to represent a distributed component (such as a waveguide, or a traveling-wave modulator [47]) with a lumped model. We have shown here that a waveguide with no dispersion can be represented as a lumped model without any approximation, and how we handle chromatic dispersion will be shown in the next section. This is important for the modeling of WDM links and other coherent optic systems, where chromatic dispersion compensation methods are required for achieving the target performance. [48].

Chapter 3

Chromatic Dispersion Simulation with VerilogA

Accurate modeling of dispersion in integrated photonic systems is important to capture how light propagates through integrated chips and can be particularly important when modeling pulses and pulse-shapers; highly dispersive components such as slow light waveguides; or systems, such as DWDM systems, where second-order effects start to play a role. Dispersion modeling is well understood in more physics-based applications, but there has been relatively little work aimed at including it into behavioral models.

3.1 Wave Representation and Waveguide Equation

As explained in the previous section, the analytic representation of the electric field relative to the reference frequency ω_R at location z and time t is $\tilde{E}_{shift}(z,t)$. Considering the linear partial differential equation governing chromatic dispersion [49]:

$$\frac{\partial \tilde{E}_{shift}(z,t)}{\partial z} = j\frac{D\lambda^2}{4\pi c}\frac{\partial^2 \tilde{E}_{shift}(z,t)}{\partial t^2} \tag{3.1}$$

With a Fourier transform on both sides, we arrive at the same solution:

$$\mathbb{E}_{shift}(z, \Delta\omega) = \mathbb{E}_{shift}(0, \Delta\omega)e^{\frac{1}{2}(\Delta\omega)^2\beta_2 z} = \mathbb{E}_{shift}(0, \Delta\omega)\mathbb{G}(z, \Delta\omega) \tag{3.2}$$

Since we simulate in time domain, we require the impulse response of the chromatic dispersion, which can be obtained by performing inverse Fourier transform on $\mathbb{G}(z, \omega)$, resulting in:

$$g(z, t) = \sqrt{\frac{c}{jD\lambda^2 z}}e^{j\frac{\pi c}{D\lambda^2 z}t^2} = \sqrt{\frac{c}{jD\lambda^2 z}}e^{j\phi(t)} \tag{3.3}$$

As chromatic dispersion is a linear process, the waveguide can be modeled as two lumped transfer functions; one handling the phase shift and time delay as discussed in the previous chapter, and one handling the chromatic dispersion discussed here. We will verify this to be true by splitting the waveguide into segments, and obtaining the same result.

3.2 Discrete-Time and other Numerical Considerations

3.2.1 Discrete-Time Finite Impulse Response

As explained in [50], the impulse response in equation 3.3 is infinite in duration, non-causal, and passes all frequencies, so for us to be able to simulate this in discrete-time, we need to truncate the impulse response to a finite duration. To determine the length of the truncation window for a given waveguide length L, we need to limit the angular frequency of the impulse response $\omega = \frac{\partial\phi(t)}{\partial t} = \frac{2\pi ct}{D\lambda^2 L}$ to be within the Nyquist frequency given by $\omega_n = \pi/T_s$ where T_s is the simulation time step. This results in an upper bound and lower bound on t:

$$-\omega_n \leq \omega \leq \omega_n \Rightarrow -\frac{|D|\lambda^2 L}{2cT_s} \leq t \leq \frac{|D|\lambda^2 L}{2cT_s} \tag{3.4}$$

When we implement the impulse response over the entire range in equation (3.4), the

chromatic dispersion is constant over the entire simulation frequency range F_s, which spans $-0.5/T_s$ to $0.5/T_s$. With a finite duration and fixed time step, we can implement $g(L,t)$ with a discrete-time finite impulse response (FIR) filter $g(L,k)$ with N taps in VerilogA, whose taps have the following expression:

$$a_k = \sqrt{\frac{cT_s^2}{jD\lambda^2 L}} e^{\frac{j\pi cT_s^2 k^2}{D\lambda^2 L}} \text{ where } -\left\lfloor \frac{N}{2} \right\rfloor \leq k \leq \left\lfloor \frac{N}{2} \right\rfloor \text{ and } N = 2\left\lfloor \frac{|D|\lambda^2 L}{2cT_s^2} \right\rfloor + 1 \qquad (3.5)$$

To gain some intuition on how D, L, or T_s impact the FIR filter, we consider the following properties of the discrete-time FIR filter: frequency range F_s is inversely proportional to time-domain sample period T_s, and frequency resolution is proportional to the time-domain filter length NT_s. When we increase D or L, the filter length is increased to resolve more dispersion in the given frequency range. When we reduce T_s, the Nyquist frequency range increases, which also increases the FIR filter length constraint as described by equation 3.5, thus N is inversely proportional to T_s^2.

When running a simulation, if the frequency range is somewhat known, the user can choose T_s to be the maximum size to still encompass any important phenomena, thus minimizing the total time steps in the simulation, and also minimizing N. On the other hand N must be large enough such that the sampling error doesn't distort the simulation result too much. For example, if $D * L$ is small to begin with, T_s must be smaller to keep N sufficiently large. Empirically, N greater than a few hundred is sufficient. If we only need constant chromatic dispersion over a smaller segment of the frequency range $B \leq F_s$ in our simulations, then we can scale down the array length by a factor of BT_s. This allows us to lighten the numerical load even more.

3.2.2 Causality Constraints

To ensure the overall waveguide model of length L is causal, we have an additional requirement that the non-causal half of the impulse response be shorter than the group

delay of the waveguide itself. This gives us the following constraint:

$$\frac{|D|\lambda^2 L}{2cT_s} \leq \frac{n_g L}{c} \Rightarrow \frac{|D|\lambda^2}{2n_g} \leq T_s \tag{3.6}$$

At the same time, for the FIR filter to have any function, $N/2$ must be greater than one (and even greater for better accuracy), thus producing the following constraint:

$$\frac{N}{2} \geq 1 \Rightarrow \frac{|D|\lambda^2 L}{2c} \geq T_s^2 \tag{3.7}$$

Combining equations 3.6and 3.7 results in the following constraint:

$$(\frac{|D|\lambda^2}{2n_g})^2 \leq \frac{|D|\lambda^2 L}{2c} \Rightarrow |D| \leq \frac{2n_g^2 L}{c\lambda^2} \tag{3.8}$$

3.2.3 Windowing

We notice here that the cutoff at the ends of the finite impulse response is rounded to a discrete-time step. This causes a simulation artifact corresponding to the length of the FIR filter, especially when simulating a high-frequency pulse, as shown in the top half of Fig. 3-1. We can eliminate this discretization problem by adding a window function which trades-off between amplitude resolution and frequency resolution. We choose the Nuttall window, given by the following:

$$\begin{aligned} w(n) &= a_0 - a_1 cos(\frac{2\pi n}{N-1}) + a_2 cos(\frac{4\pi n}{N-1}) - a_3 cos(\frac{6\pi n}{N-1}) \\ a_0 &= 0.355768; \quad a_1 = 0.487396; \quad a_2 = 0.144232; \quad a_3 = 0.012604; \end{aligned} \tag{3.9}$$

This window function goes to zero at $n = 0$ and $n = N - 1$, and its first derivative is continuous throughout, making it suitable for our purposes. To add this filter, we simply set N to equal the length of our FIR filter $2\left\lfloor \frac{|D|\lambda^2 z}{2cT_s^2} \right\rfloor + 1$, and perform element-wise multiplication between the original FIR filter and the window function to create the windowed FIR filter. Windowing doesn't add to the simulation time as this operation is only done once at the initial step. This eliminates the simulation artifact, at the cost of a little distortion, shown

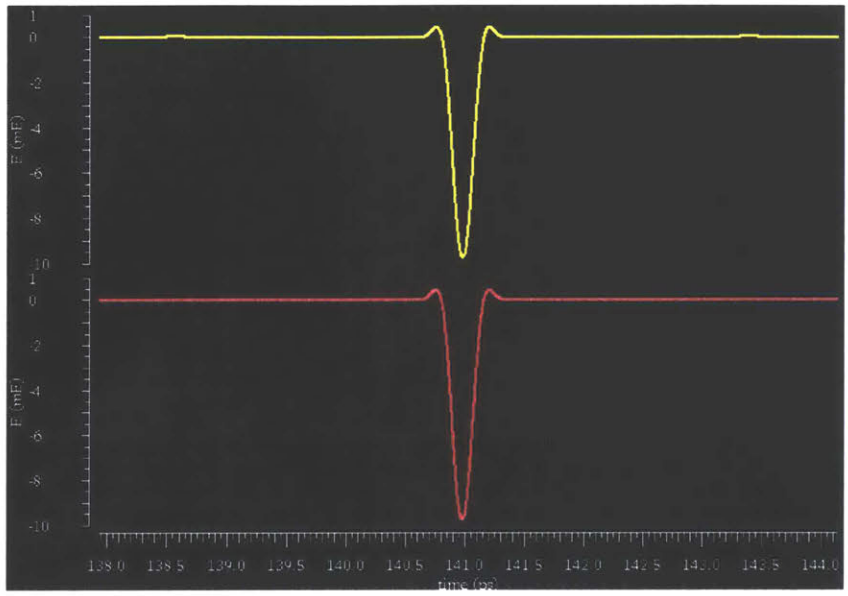

(a)

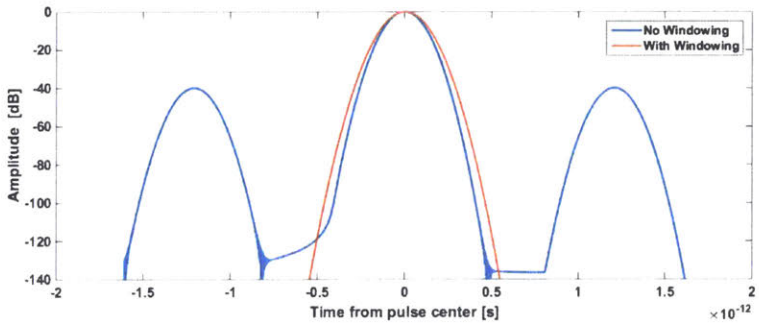

(b)

Figure 3-1: (a) $\mathbb{R}\mathrm{e}\{\tilde{E}\}$ of a Gaussian pulse passing through a dispersive waveguide with (bottom, red) and without (top, yellow) windowing. Note the simulation artifacts on each side of the main pulse without windowing. (b) Changing the y-axis to logarithmic scale shows the difference windowing makes.

in the bottom half of Fig. 3-1.

With these features in mind, we can proceed to implement the waveguide in VerilogA as shown in Figure 3-2. First we determine the array size according to equation 3.5 (the variable "ArrayL" is $\lfloor \frac{N}{2} \rfloor$ and the variable "bandwidth" is the frequency range B). As discussed in equation 3.5, N needs to be sufficiently large for the dispersive effect to be simulated accurately. In the case where ArrayL equals zero, during initialization, the simulation will throw a flag stating "Dispersion ignored as insignificant", and then proceed to simulate this waveguide as one without dispersion. If ArrayL is greater than zero, the combined impulse response (real/imaginary arrays "harrR" and "harrI") of the chromatic dispersion transfer function and the window transfer function is created to conclude initialization.

Then, at every time step, the combined impulse response is convoluted with the incoming signal's time sample array (real/imaginary arrays "EarrR" and "EarrI") producing the dispersed output, and then EarrR and EarrI are updated. Finally, the phase shift and time delay is applied to the released output.

3.3 Simulation Verification

To verify the accuracy of the waveguide model, we now present a series of scenarios to compare the simulation results with what is analytically expected in theory.

The simplest test to perform is to split the waveguide segment into two waveguide segments half the length in series, keeping the other physical properties unchanged, and check to see if we get the same results. We show this to be true in Fig. 3-3. Next we can verify that the dispersive effects of a waveguide segment is canceled out by connecting in series a second waveguide segment of identical properties, except for the dispersion coefficients having opposite signs. We see that this also holds true in Fig. 3-3. We also compare the dispersion results with matlab simulations, and we also see that the results match shown in Fig. 3-4.

```
// VerilogA for VerilogALib, Optical_Waveguide_w_Dispersion_notstep, veriloga
 include "../../../../cad/constants.vams"
 include "../../../../cad/disciplines.vams"
module Optical_Waveguide_w_Dispersion_notstep(inlig, outlig );
    inout   [0:3]           inlig;  // [0:1] is left side input, [2:3] is left side output
    inout   [0:3]           outlig; // [0:1] is right side output [2:3] is right side input
    optical [0:3]            outlig, inlig;
    parameter real L = 0.01;
    parameter real ng  = 4.1963;
    parameter real np = 2.1;
    parameter real D2 = 30e-6;
    parameter real alphaA = 0;
    parameter real G_freq = 1.93e14;
    real lambda =  P_C/G_freq ;
    parameter real tstep = 2e-15;
    parameter real bandwidth = 1000e12;
    localparam ArrayL_p = 200000;
    integer ArrayL = abs(abs(0.5*(D2*lambda*lambda*L)/( P_C*tstep*tstep))-0.5)*min(1,2*bandwidth*tstep) ;
    real holderR;
    real holderI;
    real harrR[0:ArrayL_p*2];
    real harrI[0:ArrayL_p*2];
    real EarrR[0:ArrayL_p*2];
    real EarrI[0:ArrayL_p*2];
    integer i;
    integer j;
    optical [0:1] outNodly;  // cart
    optical [0:1] outNodlyB;
    optical [0:1] transfer;
    optical [0:1] transferConv;
    optical [0:1] 0outlig;
    pol2cart conv1(transfer, transferConv);
    cartmul mulout1(transferConv, inlig[0:1], outNodly);
    cartmul mulout1B(transferConv, outlig[2:3], outNodlyB);
    analog begin
        @(initial_step) begin
            if(ArrayL > 0) begin
                for(j=0; j<2*ArrayL+1; j = j+1) begin // window function cut off from screen -->
                    harrR[j] = (0.355768-0.4873965*cos( M_PI*j/ArrayL)+0.144232*cos(2* M_PI*j/Arr
                    harrI[j] = (0.355768-0.4873965*cos( M_PI*j/ArrayL)+0.144232*cos(2* M_PI*j/Arr
                    EarrR[j] = 0;
                    EarrI[j] = 0;
                end
            end else begin
                for(j=0; j<2*ArrayL+1; j = j+1) begin
                    if(j == ArrayL) begin
                        harrR[j] = 1;
                        harrI[j] = 0;
                    end else begin
                        harrR[j] = 0;
                        harrI[j] = 0;
                    end
                    EarrR[j] = 0;
                    EarrI[j] = 0;
                end
                $strobe("Dispersion ignored as insignificant");
            end
            $strobe("ArrayL = %d",ArrayL);
            $strobe("D2 = %g",D2);
            $strobe("L*ng/C = %g", L*ng/ P_C);
            $strobe("Array*tstep = %g",ArrayL*tstep);
            holderR = 0.0;
            holderI = 0.0;
        end
        E(transfer[0]) <+ (-L*np*2* M_PI*G_freq/ P_C)%(2* M_PI);
        E(transfer[1]) <+ exp(-alphaA*L);

        @(timer(tstep, tstep)) begin
            EarrR[0] = E(outNodly[0]);
            EarrI[0] = E(outNodly[1]);
            holderR = 0.0;
            holderI = 0.0;
            for(i=0; i<2*ArrayL+1; i = i+1) begin
                holderR = (EarrR[i]*harrR[i]-EarrI[i]*harrI[i])+holderR;
                holderI = (EarrR[i]*harrI[i]+EarrI[i]*harrR[i])+holderI;
            end
            for(i=2*ArrayL; i>0; i = i-1) begin
                EarrR[i] = EarrR[i-1];
                EarrI[i] = EarrI[i-1];
            end
        end
        E(outlig[0]) <+ absdelay(holderR, (L*ng/ P_C-ArrayL*tstep));
        E(outlig[1]) <+ absdelay(holderI, (L*ng/ P_C-ArrayL*tstep));
        E(inlig[2]) <+ absdelay(E(outNodlyB[0]), (L*ng/ P_C-ArrayL*tstep));
        E(inlig[3]) <+ absdelay(E(outNodlyB[1]), (L*ng/ P_C-ArrayL*tstep));
        end
endmodule
```

Figure 3-2: Waveguide with dispertion

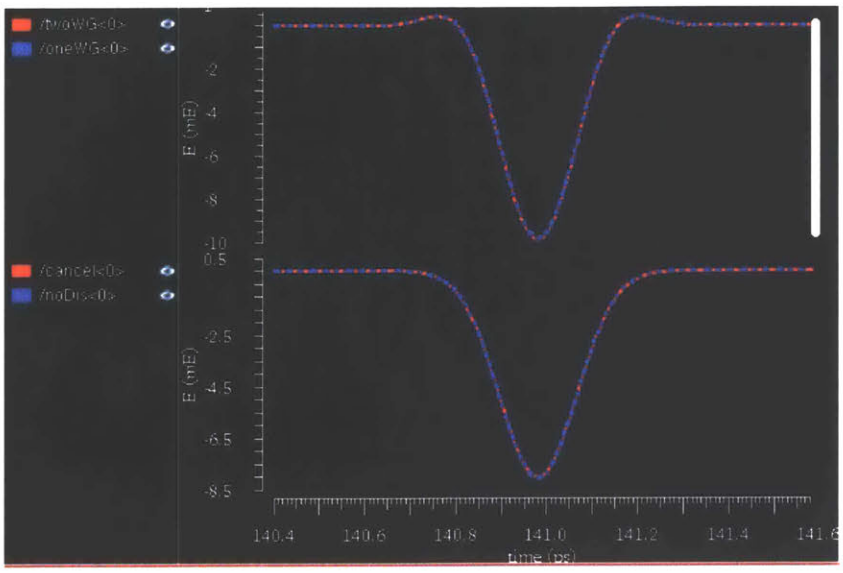

Figure 3-3: Top: $\mathbb{R}\mathrm{e}\{\tilde{E}\}$ of a Gaussian pulse passing through a dispersive waveguide (blue) and two waveguide segments of half length with other physical properties unchanged (red). Bottom: $\mathbb{R}\mathrm{e}\{\tilde{E}\}$ of a Gaussian pulse passing through a non-dispersive waveguide (blue) and two waveguide segments of half length with dispersion coefficient of opposite sign (red), canceling out the dispersive effects.

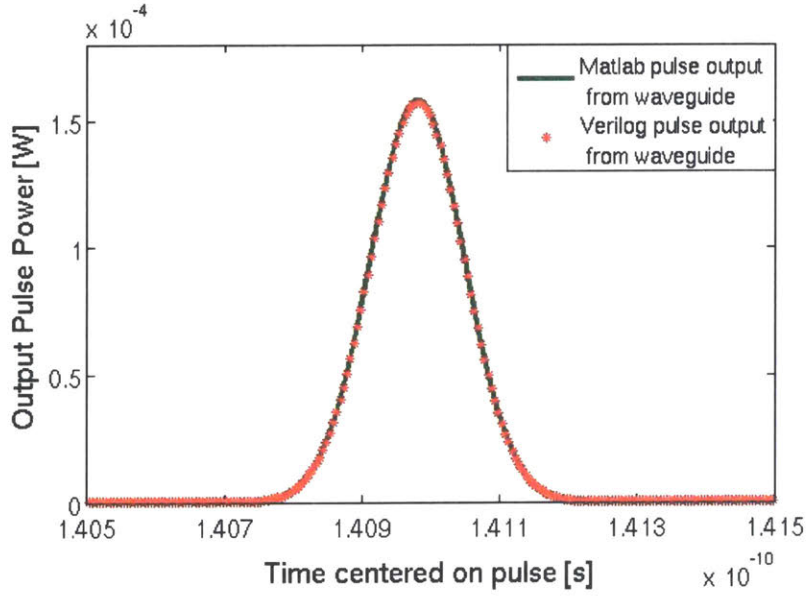

Figure 3-4: Intensity of a Gaussian pulse passing through a dispersive waveguide, simulated with VerilogA and Matlab, producing the same result.

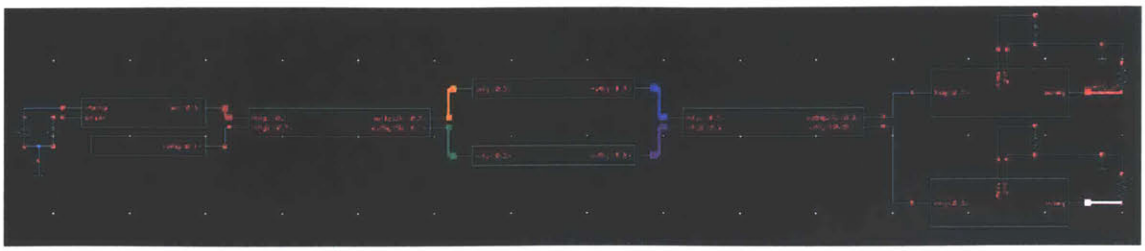

Figure 3-5: Schematic of Mach-Zehnder(MZ) interferometer for chromatic dispersion measurement. On the left is a continuous wave laser with a sweeping frequency. In the center is an MZ structure with the top arm representing the dispersive waveguide under test, and the bottom arm representing an air path with adjustable length. We detect the intensity output of the interferometer using photodiode models.

3.4 Chromatic Dispersion Simulation in Systems

Now that we have verified the correctness of the dispersive waveguide model, we can apply it into a few systems and check if the results remain consistent.

3.4.1 Chromatic Dispersion Coefficient Measurement

Many methods exist for measuring the chromatic dispersion coefficient in optical waveguides, we choose to implement the interferometric method [51] [52] in this paper to show that the simulated measurement result is identical to the coefficient value we assign as a design parameter. This method is ideal for measuring short waveguide lengths.

To setup the simulation, we assemble a Mach-Zehnder interferometer as shown in Fig. 3-5. The chromatic dispersion coefficient of the waveguide is set to be 10^3ps/nm/km or 10^{-3}s/m^2, and its length is 1mm. If we sweep the frequency of the laser source, the intensity should have a profile described [52] in the following equation:

$$I_{out}(\lambda) = I_{air}(\lambda) + I_{WG}(\lambda) + 2V(I_{air}(\lambda)I_{WG}(\lambda))cos\frac{2\pi}{\lambda}(l_{air} - l_{WG}n(\lambda)) \tag{3.10}$$

where λ is the wavelength of the laser light, l_{air} is the length of the air path, l_{WG} is the

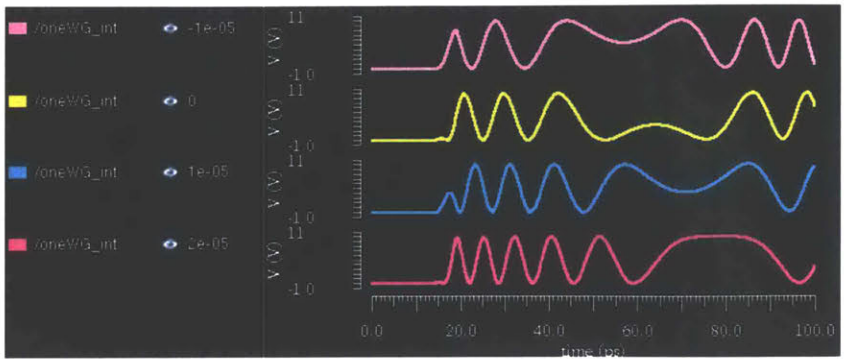

Figure 3-6: Each waveform is a transient simulation sweeping the laser frequency from -30THz to 30THz, and the air path length differs from a nominal length by -10μm, 0μm, 10μm, and 20μm from top to bottom.

length of the test waveguide, V is the coherence function, and $n(\lambda)$ is the effective refractive index of the waveguide. If we measure the center wavelength (which happens at zero path-length imbalance), for different air path lengths, we can calculate the chromatic dispersion coefficient with the following equation:

$$D = \frac{1}{l_{WG}} \frac{\Delta l_{air}}{c\Delta\lambda} \tag{3.11}$$

Running the simulation result in the waveforms showed in Fig. 3-6. We see that for a 30μm difference in air path length, the center frequency varies by 1.25×10^{13}Hz, which means the wavelength varies by 100nm as our simulation reference wavelength is 1550nm. Putting these measured results back into equation 3.11 gives us $D = 10^{-3}\text{s/m}^2$, which is exactly what we put in the first place.

3.4.2 Chromatic Dispersion in Data Link

The total dispersion in a waveguide is determined by the product $D2 * L$, if we wish to transmit data across this waveguide, inter-symbol-interference caused by dispersion limits the rate at which data can be sent and still have an open eye. In this simple example, we send a 25Gbps data stream to a mach-Zehnder device, and observe the output after waveguides with varying $D2 * L$ values, shown in Figure 3-7.

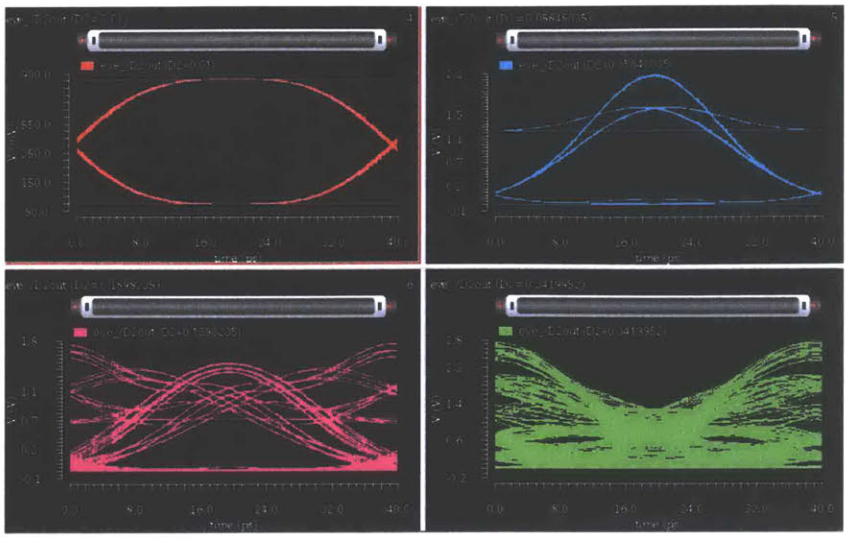

Figure 3-7: From top left to bottom right: output observed after 25Gbps data stream sent through waveguide with $D2 * L$ of $0.01, 0.058, 0.19, 0.34(s/m)$.

Since dispersion is a linear process, we can use the inverse of the FIR filter shown in equation 3.5 to improve our eye opening. Here we show that as little as 2X oversampling (50Gsps) is sufficient to open the eye even at $D2 * L = 20(s/m)$, shown in Figure 3-8.

3.5 Conclusions

We present an expansion on a Cadence toolkit library written in VerilogA for simulation of electro-optical systems [53], to include chromatic dispersion (CD) in waveguides. We discuss the different approaches to implement these effects, and the simulation testbenches for verification. We show that the results match other simulations and analytic solutions that have previously been compared to theory for both simple devices, and demonstrate complicated systems that utilize these effects.

In the following section, we will discuss nonlinear modeling of the waveguide. The high index contrast of silicon allows waveguides with very small cross-sections, resulting in high intensities in the material. Combined with the significant third-order susceptibility $\chi^{(3)}$ in silicon waveguides, it is important to model nonlinear processes such as the optical Kerr

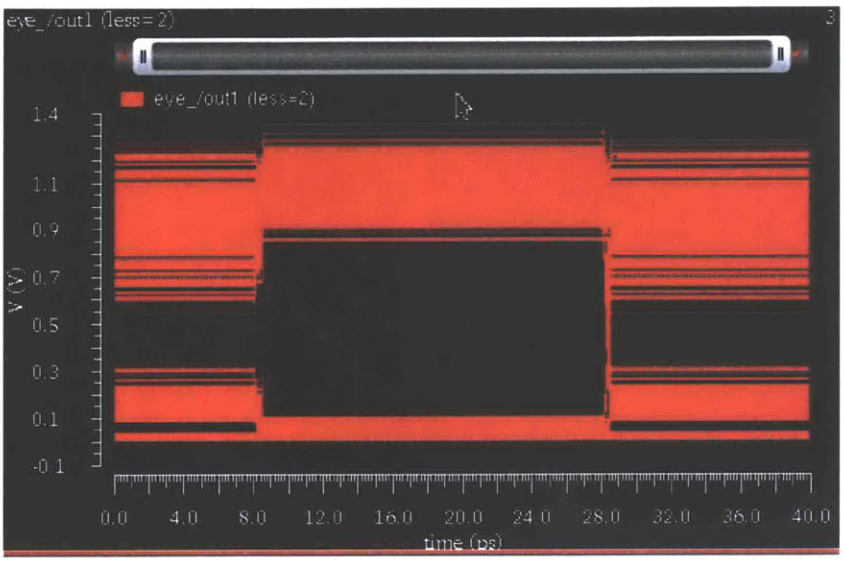

Figure 3-8: Output after inverse FIR filter taps implemented at 50G samples per second. Waveguide $D2 * L = 20(s/m)$

effect, two-photon absorption (TPA), and free-carrier dispersion [54].

Chapter 4

Nonlinear Waveguide Simulation with VerilogA

The high index contrast of silicon allows waveguides with very small cross-sections, resulting in high intensities in the material. Combined with the significant third-order susceptibility $\chi^{(3)}$ in silicon waveguides, it is important to model nonlinear processes such as the optical Kerr effect, two-photon absorption (TPA), and free-carrier dispersion [54]. Here we will discuss our methods in modeling these effects using our platform.

4.1 Nonlinear Processes

4.1.1 The Optical Kerr Effect

Due to the optical Kerr effect, high optical intensity in a material will cause a proportional change in the refractive index $\Delta n = n_2 I(t)$ where n_2 is the nonlinear index of the material. n_2 is related to the real part of $\chi^{(3)}$ through $n_2 = \frac{3\chi^{(3)}}{4c\epsilon_0 n_0^2}$. Depending on the waveguide design, the effective cross sectional area A_{eff} determines its nonlinear coefficient $\gamma = \frac{2\pi n_2}{\lambda A_{eff}}$. So for a given waveguide length L and optical intensity I the nonlinear phase change obtained is $\phi_{nonlinear} = \gamma I L$.

4.1.2 Two-Photon Absorption

When the total energy of two photons is greater than the bandgap energy of silicon, they can both be absorbed by exciting an electron from the valence band to the conduction band. (Here we do not distinguish between degenerate and non-degenerate two-photon absorption (TPA).) TPA induces a linear intensity dependance on the total absorption of the material $\Delta\alpha(I) = \beta I$, where β is the TPA coefficient which ranges from $5 \times 10^{-12} mW^{-1}$ to $9 \times 10^{-12} mW^{-1}$.

4.1.3 Free-Carrier Absorption and Dispersion

Free carriers (electrons and holes) generated by TPA cause free-carrier absorption (FCA) and free-carrier dispersion (FCD), which change both the real and imaginary parts of the refractive index. The free carrier density $N(t)$ in a silicon waveguide is related to the input optical intensity as described by the following equation:

$$\frac{dN(t)}{dt} = \frac{\beta I^2(t)}{2h\nu} - \frac{N(t)}{\tau} \tag{4.1}$$

where τ is the recombination lifetime, which can be designed to range from picoseconds to $200ns$.

The empirical relation between FCA and FCD to $N(t)$ for 1550nm are shown below [55]:

$$\begin{aligned} \Delta\alpha &= -[8.5 \times 10^{-18} \Delta N_e + 6 \times 10^{-18} \Delta N_h] \\ \Delta n &= -[8.8 \times 10^{-22} \Delta N_e + 8.5 \times 10^{-18} \Delta N_h^{0.8}] \end{aligned} \tag{4.2}$$

Note that in this case, the number of holes and electrons generated by TPA are equal, $\Delta N_e = \Delta N_h = N(t)$

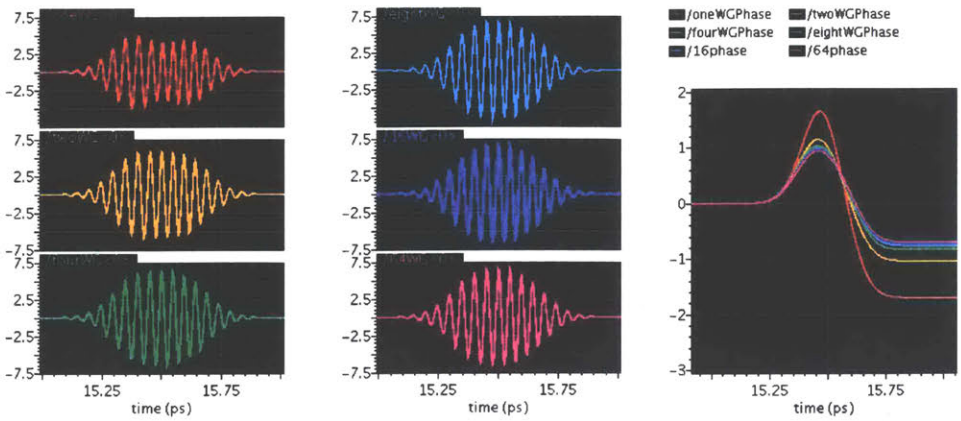

Figure 4-1: Left and Center: $\mathbb{R}\mathrm{e}\{\tilde{E}\}$ output of a nonlinear waveguide split into increasing number of segments. Right: Corresponding phase shift of those waveguides. The units for power and free carrier density are chosen such that the simulator (spectre in our case) won't experience very large numbers and throw a warning flag.

4.2 Nonlinear Waveguide Simulation

The nonlinear processes described above can be simulated by describing the absorption coefficient α and index of refraction n as variables:

$$\begin{aligned} \alpha &= \alpha_{lin} + \beta I + \Delta\alpha_{FC}(N) \\ n &= n_0 + n_2 I + \Delta n_{FC}(N) \end{aligned} \tag{4.3}$$

Note that this is a lumped model, so in order to model the self-induced change in intensity and phase accurately, the waveguide is split into smaller steps. We can see how the simulation results converge to the accurate solution as we split the waveguide more finely in Fig. 4-1.

This method is also necessary for simultaneously simulating dispersion along with the nonlinear effects. Different ways of splitting the steps (uniform, logarithmic, dynamic) are discussed in [56]. Uniform step sizes are used in this code for simplicity, but more complex methods can be used to achieve the same accuracy with less computation. The amount of computation saved also depends on the target system and its inputs. The logarithmic split-step method is comparatively straight forward to implement, and will be done in the next iteration of the code.

```
// VerilogA for VerilogALib, Optical_Waveguide_nonlin_heat, veriloga
 include "../../../../cad/constants.vams"
 include "../../../../cad/disciplines.vams"
module Optical_Waveguide_nonlin_heat(inlig, outlig, heat);
    inout   [0:3]           inlig;  // [0:1] is left side input, [2:3] is left side output
    inout   [0:3]           outlig; // [0:1] is right side output [2:3] is right side input.
    optical [0:3]            outlig, inlig;
    inout heat;
    electrical heat;
    parameter real L = 0.01;
    parameter real ng  = 4.1963;
    parameter real np = 2.1;
    parameter real alphaA = 0;
    parameter real n2 = 4e-18; //m^2 W^-1
    parameter real G_freq = 1.93e14;
    real lambda =  P_C/G_freq ;
    parameter real tau = 5e-9;
    parameter real beta = 7e-12;
    parameter real tstep = 1e-12;
    parameter real nt = 1.86e-4;
    parameter real heatco = 1;
    real power;
    real FCDn;
    real FCDa;
    real NfreeC;
    integer i;
    integer j;
    optical [0:1] outNodly;//cart
    optical [0:1] outNodlyB;
    optical [0:1] transfer;
    optical [0:1] transferConv;
    pol2cart convs1(transfer, transferConv);
    cartmul mulout1(transferConv, inlig[0:1], outNodly);
    cartmul mulout1B(transferConv, outlig[2:3], outNodlyB);
    analog begin
        @(initial_step) begin
                power = 0;
                NfreeC = 1e-30;
        end
        $bound_step (tstep);
        power = (E(inlig[0])*E(inlig[0])+E(inlig[1])*E(inlig[1]));
        //"Efield" input is in units of sqrt(1TW/m^2), "power" is in units of 1TW/m^2
        NfreeC = idt(1e-30*beta*power*power*1e24/(2* P_H*G_freq) - NfreeC/tau, 1e-30);
        // units in per cubic angstrom or 1e-30 m^-3 or 1e24*NfreeC = N in cm^-3
        // power^2 needs to multiplied by 1e24
        FCDa = - (8.5e6)*NfreeC*100 - (6e6)*NfreeC*100;
        FCDn = - (8.8e2)*NfreeC - (8.5e-18)*pow((NfreeC*1e24),0.8);
        //first set inputs and outputs for forward propagating wave:
        // using equations in "ultrafast nonlinear all-optical processes in silicon-on-insulator waveguides"
        E(transfer[0]) <+ (-L*(np + n2*power*1e12 + FCDn + V(heat)*nt)*2* M_PI*G_freq/ P_C)%(2* M_PI);
        E(transfer[1]) <+ exp((-alphaA - beta*power*1e12 + FCDa)*L);
        E(outlig[0]) <+ absdelay(E(outNodly[0]), (L*ng/ P_C));
        E(outlig[1]) <+ absdelay(E(outNodly[1]), (L*ng/ P_C));
        E(inlig[2]) <+ absdelay(E(outNodlyB[0]), (L*ng/ P_C));
        E(inlig[3]) <+ absdelay(E(outNodlyB[0]), (L*ng/ P_C));
        I(heat) <+ power*heatco*-1*(1-exp((-alphaA - beta*power*1e12 + FCDa)*L));
        end
endmodule
```

Figure 4-2: Waveguide with nonlinear behavior and self-heating

The nonlinear waveguide code is shown in figure 4-2. As it is a lumped model, all of the variables are derived based on the input E field. The variable "power" calculates the incident radiation power, next the free carrier density "NfreeC" is calculated as the integral form of equation 4.1. With this, we can then derive "FCDa" and "FCDn" based on the equations in 4.3, which then in turn modify the index of refraction and absorption coefficient terms in the original waveguide equation. Lastly, we add in a "heat" term to output how much heat is generated by all mechanisms of absorption. This allows us to add thermal resistors and capacitors representing the thermal environment of the device, and simulate self heating effects as shown later in this chapter.

4.3 Simulation Verification

4.3.1 Self-phase Modulation

Now let us examine self-phase modulation of a Gaussian pulse caused by the Kerr effect. The rising edge should see a positive $d(\Delta\phi)/dt$, and the trailing edge sees a negative one, causing a spectral spread. By implementing this scenario, we get the expected results as shown in Fig. 4-3

For a full verification of all three nonlinear processes described in equation 4.3, we can implement the test cases in [54] and compare the results, seen in Fig. 4-4.

4.3.2 Resonant Ring Example

Now to test the nonlinear behavior in a system, let us use a resonant ring as a simple example. At frequencies close to resonance, as the intensity of the light inside the ring increases, the index of refraction changes due to the Kerr effect and FCD, which cause a shift in the resonant frequencies. In figure 4.3.2 (a) we see that as we increase the input intensity, the resonance frequency shifts as expected.

Furthermore, when keeping the CW laser intensity at a high enough constant value, the resonance peak "folds back", resulting in three valid transmissions levels, of which two are

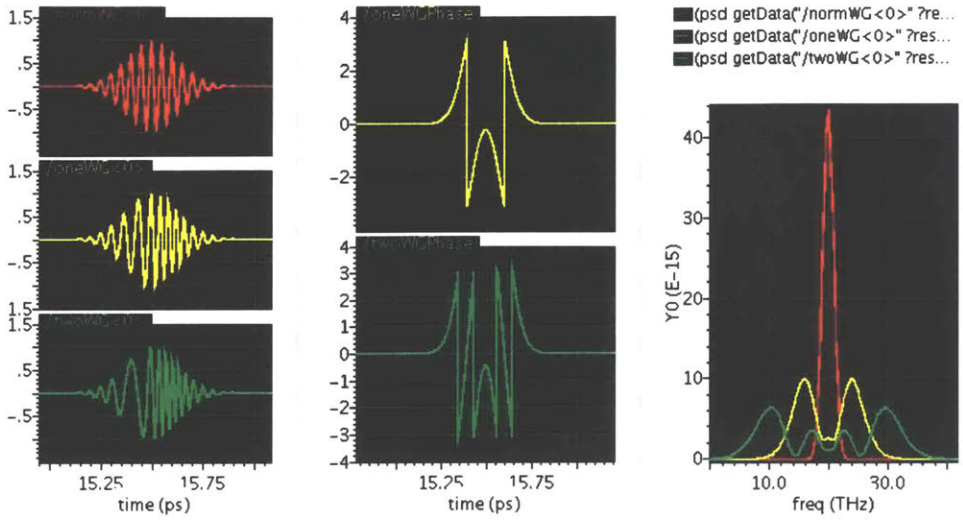

Figure 4-3: Left: $\mathbb{R}\mathrm{e}\{\tilde{E}\}$ output of a linear waveguide (red), nonlinear waveguide with different n_2 values (yellow and green). Center: Phase shift of nonlinear waveguide output relative to the linear waveguide output. Right: Spectrum of the waveguide output.

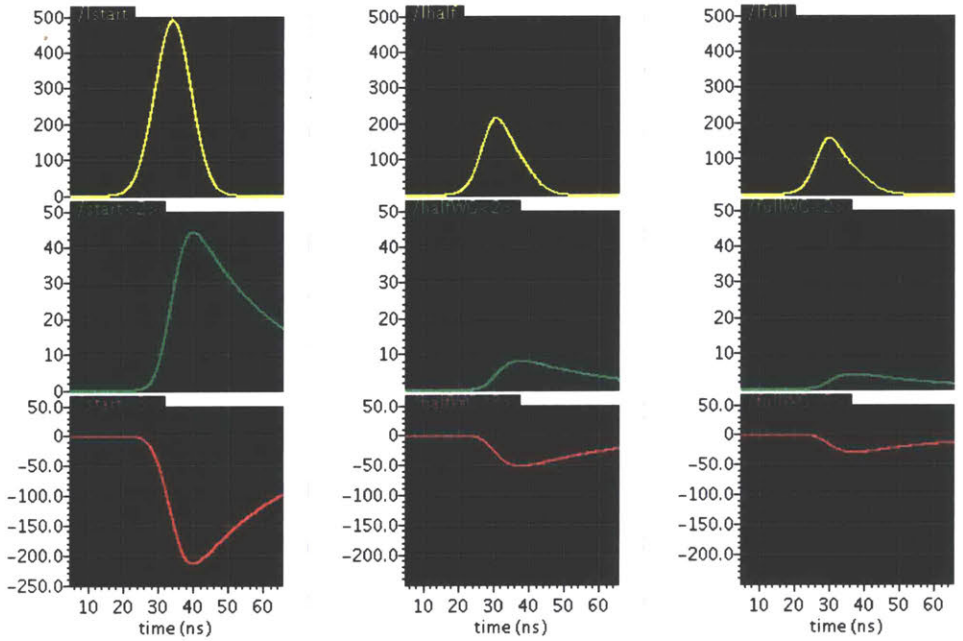

Figure 4-4: Left to right columns: Simulation results taken at z=0mm, 24mm, 48mm. Top to bottom rows: Intensity ($10^9 W/m^2$), free carrier density N ($10^{21} m^{-3}$), and refractive index change Δn (10^{-6}).

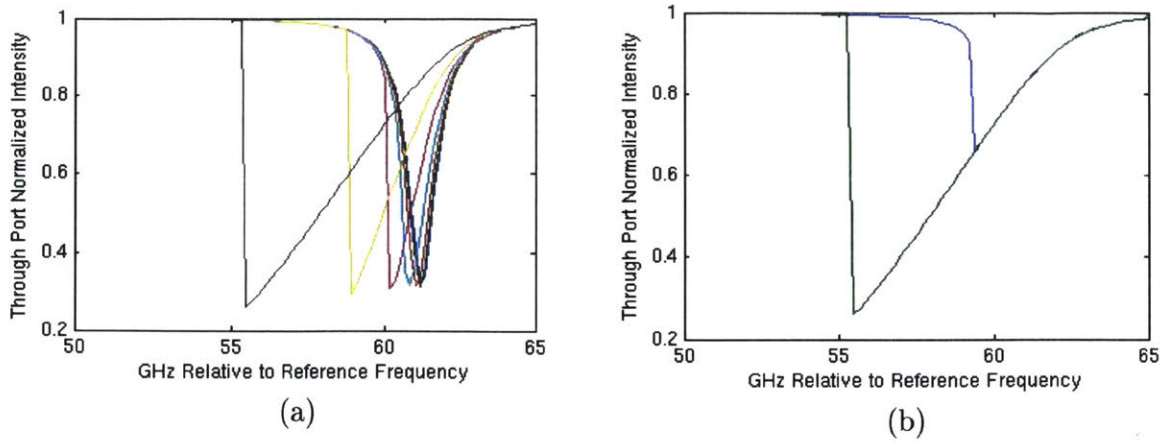

Figure 4-5: (a) Self heating is not considered in this short time-scale simulation, so the resonance frequency shifts lower as input laser intensity increases. (b) Bistable behavior shown: Blue curve is sweeping the laser frequency low to high, green curve is sweeping the laser frequency from high to low.

stable solutions [57]. This means that the spectrum measured at the through port will differ between sweeping the laser frequency from low to high vs. from high to low. Figure 4.3.2 (b) shows this behavior.

It is important to note that the energy lost to absorption generates heat, which modifies the index of refraction through thermal-optic effects mentioned in 2.11 and 2.12. Normally the thermal effect is greater than the Kerr effect and FCD, but at a much slower time constant, so if the laser frequency is swept slowly, then the resonance frequency shifts in the opposite direction.

In certain conditions, self-pulsing behavior can be created [58]. As explained in the paper, when the input CW laser frequency f_{CW} is tuned to be slightly higher than the resonance frequency of the ring f_{ring} at nominal temperature, the laser intensity in the ring increases, thus creating free-carriers due to TPA, causing a brief blue-shift in f_{ring}, to the point where $f_{ring} > f_{CW}$. Then the subsequent heat generation from FCA reverses the blue-shift, and red-shifts the resonance frequency past the CW laser frequency, further increasing the amount of free-carriers and heat generation. When the temperature is sufficiently raised, f_{ring} falls much lower than f_{CW}, rapidly reducing the laser intensity and free-carriers. With the lack of

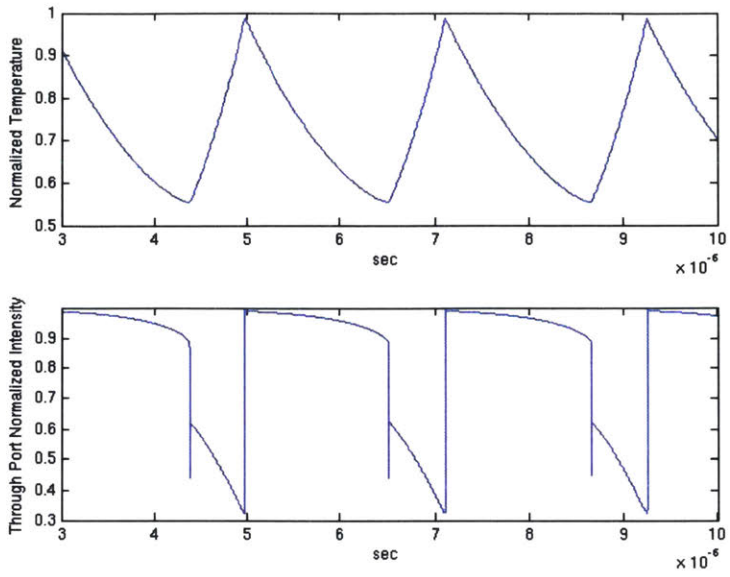

Figure 4-6: Self-pulsing behavior demonstrated in ring resonator. Free-carrier effects and temperature effects take turns in shifting the resonance frequency of the ring across the input laser frequency.

heat generation, the temperature gradually returns to normal, bringing us back to the start of the cycle. This behavior is shown in figure 4-6.

4.4 Conclusions

We present an expansion on a Cadence toolkit library written in VerilogA for simulation of electro-optical systems [53], to include nonlinear effects in waveguides. We discuss the different approaches to implement these effects, and the simulation testbenches for verification. We show that the results match other simulations and analytic solutions that have previously been compared to theory for both simple devices, and demonstrate complicated systems that utilize these effects.

Chapter 5

Electro-optical Systems

In the preceding sections, we demonstrated the ability of our system to correctly simulate simple, composite components, and basic devices. The ultimate goal of our work is to be able to simulate complex systems, particularly ones that include the electrical driving circuitry and noise models. In this section we will take the basic and composite device blocks and use them to build full heterogeneous electrical and optical systems. Note how similar the process is to building circuits out of transistors, by simply instantiating components, setting parameters, and connecting the waveguides and electrical wires, further allowing for easy combination with existing electrical simulation infrastructure and ease of use by designers familiar with such. While the toolkit can of course be used to build a multitude of different systems and simulate them at numerous operating points under a myriad of conditions, we will focus on two examples here: a wavelength division multiplexing(WDM) link and a Pound-Drever-Hall (PDH) laser stabilization loop.

5.1 Wavelength Division Multiplexing Link

One of the driving forces for integrated silicon photonics is to use WDM over optical waveguides to replace copper wires and solve the bandwidth density/energy consumption problem for data transmission links. The emergence of multi-core processors creates an

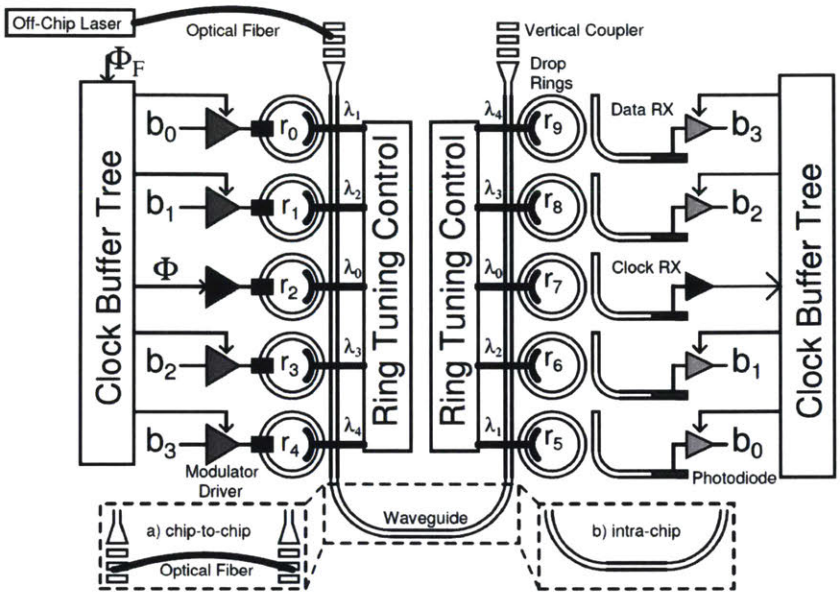

Figure 5-1: An integrated WDM photonic link.

increasingly complex routing environment for long interconnects. With traditional copper interconnects, area is expensive, as each wire is only able to carry one data signal at maximum bandwidth. Although the I/O circuits are improving in bandwidth as technology scales, the channels are not. Since each core must be able to communicate with a set of other cores and off-chip memory, the total bandwidth required is harder to reach under the overall die power constraint, set by power delivery and cooling requirements. If copper wires are not replaced, we will quickly reach a point where it is simply infeasible to add more cores.

To address this problem, this work investigates the shift to an optical paradigm, where by exploiting wavelength-division multiplexing (WDM), multiple channels of data can be transmitted along a single optical waveguide without interference. This allows a much greater bandwidth density for both on-chip and off-chip channels. Also, with low loss waveguides which are theoretically possible, the total power consumption for interconnects can be greatly reduced. With WDM, we can use architectures that have fewer routers, hence lower latency. At a macro level, the design-space of a WDM link has been explored in [59]. These results were obtained by using simple equations to model the relation between design parameters

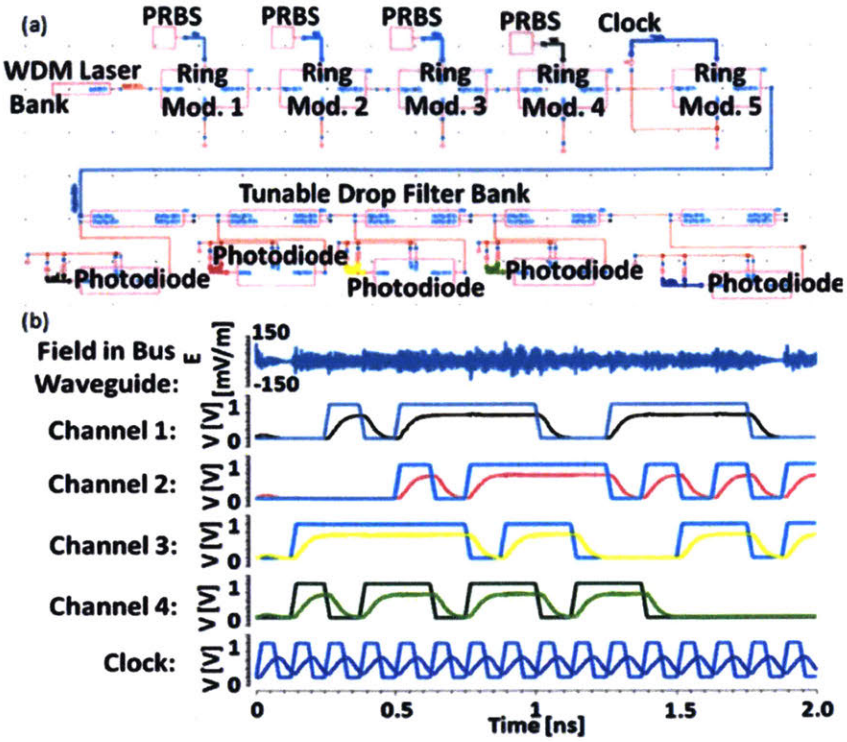

Figure 5-2: (a). Schematic of WDM link with four PRBS channels and one clock channel. (b) real part of signal on WDM waveguide (top), input and output of modulator channels (middle four channels) and clock (bottom).

and performance, giving us very useful insight, such as the optimal number of channels for a given total throughput. But if we wish to have a more detailed analysis, we need to include more physical phenomena, such as optical crosstalk, clocking jitter/skew or modulator self heating. This VerilogA framework allows the designer to include these phenomena into the simulation of such a system.

The schematic layout of a WDM link simulation using our toolkit is shown in Figure 5-2(a). To simulate the link we pass the output of a WDM laser block, which simultaneously outputs five CW frequencies, through five modulators and five ring filters in series on a single waveguide. The drop port of each ring filter is connected to a photodiode. Four of the ring modulators are driven by four different PRBS data streams. The fifth is driven by a clock stream. The simulated input and output electrical waveforms are shown in Figure 5-2(b). Note that the optical rise and fall times and signal delays are neatly captured.

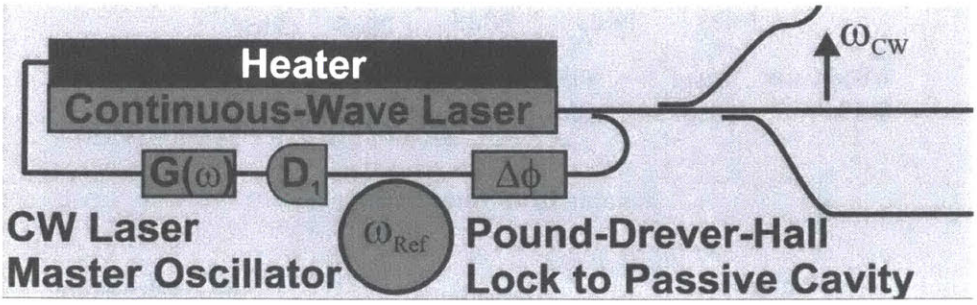

Figure 5-3: Block diagram of an integrated PDH loop.

Since all five channels are represented as one complex field signal in the waveguide, very subtle crosstalk can also be seen. That is because in this design, the channels are spaced to be 100GHz apart, while the ring modulator FWHM is 13.8GHz. Depending on other tradeoffs, the optimal channel spacing might be even closer, and this simulation toolkit will allow the designer to inspect the resulting bit-error-rates (BER) in the presence of channel crosstalk. Other non-idealities, such as thermal effects, thermal noise, transistor noise, can be added to the simulation to provide a more realistic prediction of a systems behavior.

5.2 Pound Drever Hall Loop

We next explore the operation of a purely analog, and extremely phase sensitive system, a Pound-Drever-Hall (PDH) locking loop for laser frequency stabilization, using our code. Stabilized narrow-linewidth lasers are critical for metrology, low-noise microwave sources, frequency-comb locking, and narrow-linewidth applications such as coherent communications and ranging. Pound Drever Hall(PDH) laser frequency stabilization improves an existing laser's frequency stability, by measuring the laser's frequency with a resonant structure, and this measurement is fed back to the laser to suppress frequency fluctuations. This set of simulations is also more complex as it additionally makes use of noise blocks and of standard CMOS cells to model more complicated electrical driving circuits.

5.2.1 Pound Drever Hall Loop Concept

The theory of PDH operation is described in [25]. To summarize the concept briefly: the output of a laser is sent through a phase modulator modulated by a sine wave from an RF oscillator and then past a resonant cavity, in our case a ring resonator. The optical carrier picks up a different phase-shift in relation to the modulation sidebands depending on its frequency relative to the ring reference frequency. The carrier and the sidebands are beat together on a photodiode and the resulting RF signal is mixed down to baseband using the same, equally delayed, signal from the RF oscillator. The DC component of the output is the PDH error function and its sign indicates whether the laser frequency needs to be adjusted up or down to match that of the cavity. The error function is fed back on the laser and decreases laser phase noise by locking the laser frequency to that of the resonant cavity. The PDH scheme has two operation regimes: a low modulation frequency regime where both the laser and the modulation sidebands fall within the cavity resonance, and a high modulation frequency regime where the sidebands remain outside of the cavity.

5.2.2 Pound Drever Hall Loop Simulation

A schematic layout of this system, using ideal photonic and electronic components, is shown in Figure 5-4(a). The error function output in both the low modulation and high modulation regimes is shown in Figure 5-4(b), where they are compared to, and show excellent agreement with, results generated using analytical calculated transfer-functions and joint time and frequency domain simulations in MATLAB. As in the SSB case writing and running the MATLAB code to simulate the output of the PDH took more time and was more complicated than setting up the schematic and running the VerilogA code. Note that the VerilogA output closely matches the MATLAB output.

To predict the performance of a real system with non-ideal components, a new schematic is created using accurate, non-idealized blocks for the photonics components and the actual CMOS driving circuitry in a 65nm 10LPe CMOS process. The parameter values in blocks for the photonics components are based on measured results from devices our group has designed

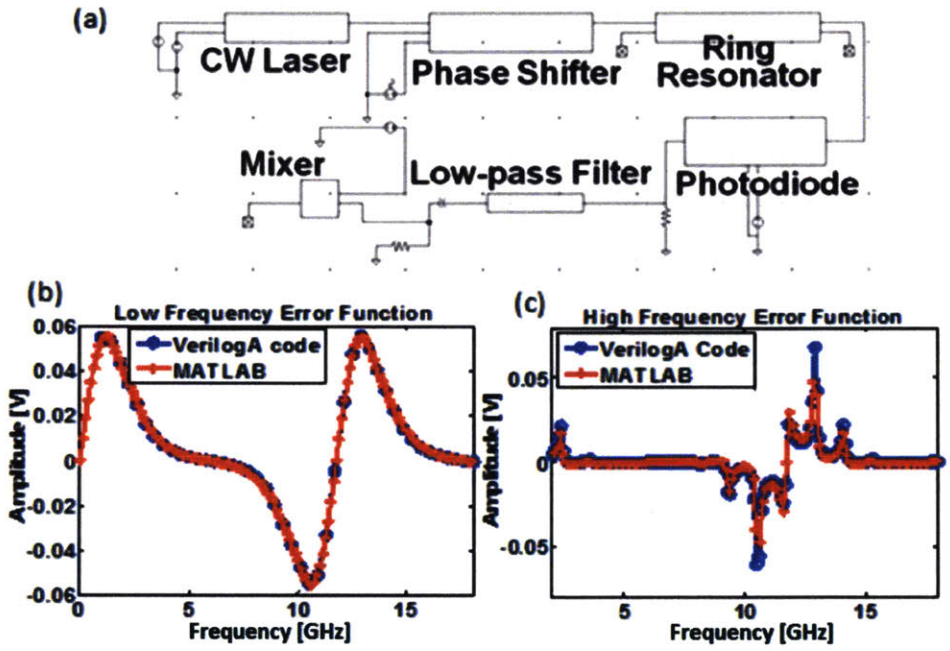

Figure 5-4: (a) Schematic layout in Cadence Virtuoso of PDH loop. (b) PDH error function in low and high frequency regimes, showing excellent agreement between MATLAB and VerilogA code.

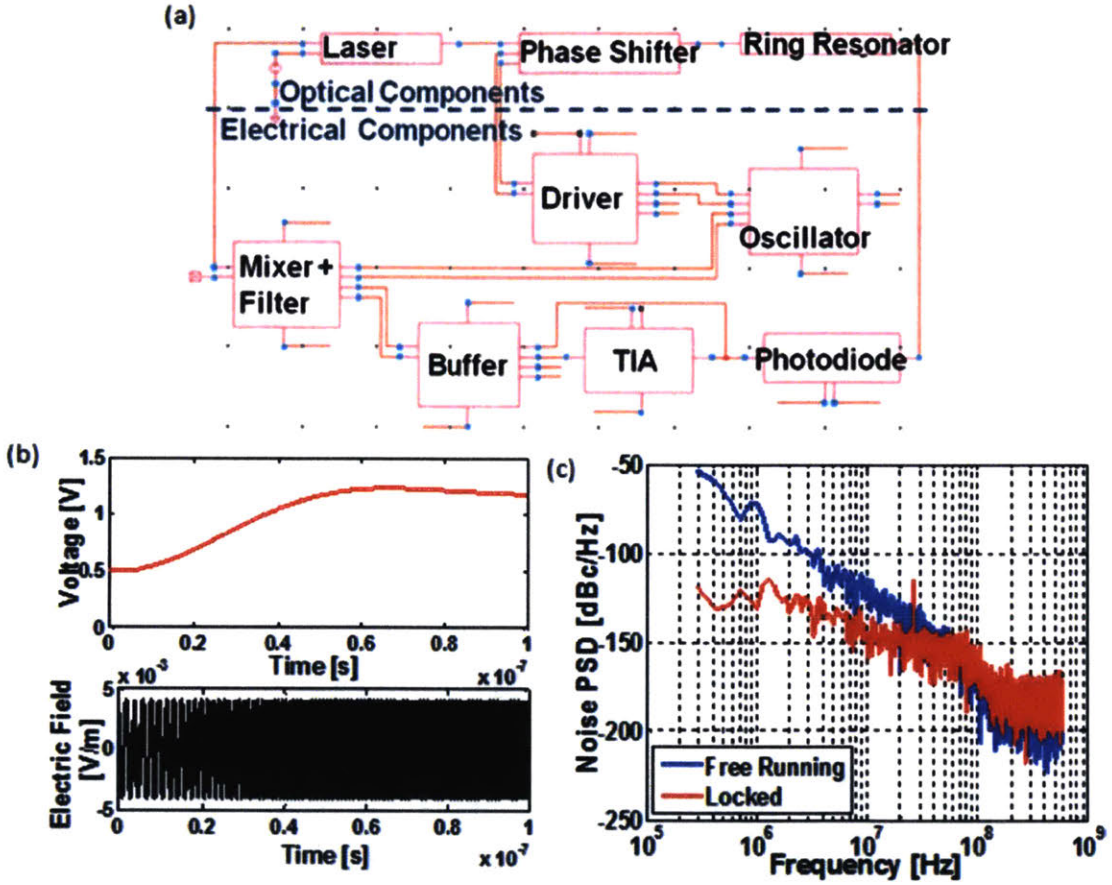

Figure 5-5: (a) Schematic layout of PDH loop using non-ideal photonics and full driving circuitry in Cadence Virtuoso. (b) Laser frequency locks to cavity reference in 100ns (red), real part of laser electric field as locking occurs (black). (c). Phase noise simulation done using our toolkit showing noise of the free-running CW laser (blue) and of the laser locked to a cavity (red) showing successful phase-noise suppression.

and tested in the lab. The driving circuitry blocks shown in the schematic are designed in-house using the CMOS component models provided by the CMOS foundry, to satisfy the needs and constraints of the photonic components and of the full system. Figure 5-5(a). shows a schematic of this full system. As can be seen, this schematic is significantly more complex that the idealized schematic in Figure 5-4.

Simulations of the whole system can then be run, and performance achievable in the lab can be predicted. Furthermore, sensitivity to operating point, operating conditions, fabrication variations, various optical and electronic noise sources, and changes in component type or design can be explored. This allows for a much better understanding of system performance and robustness than previously possible. A closed loop simulation shows the PDH in transient operation, as the feedback signal from the PDH loop changes the laser frequency to the cavity frequency (Figure 5-5(b).) To further demonstrate the code, we add phase noise to our laser using standard VerilogA noise blocks. A noise analysis is performed in Cadence Virtuoso, as would be done for purely electrical circuits. The resulting laser phase noise in both the open loop (unsuppressed) and closed loop (suppressed) case are shown in Figure 5-5(c). For this particular set of loop parameters, the PDH lock is successful and mid-frequency phase noise is suppressed by >50dB.

5.2.3 Phase Shifter non-Idealities

We can use our simulator to predict how the design parameters of each device in the loop impact the overall performance. For example, the error function of the PDH feedback signal displays different characteristics at different modulation frequencies [25]. A low-power small-area CMOS oscillator might have multiple harmonics, and the designer would like to know how that might impact the error function and PDH performance. In CNSE's photonic process, we have fabricated a phase shifter connected to a CMOS driving circuit. The CMOS driver introduces some non-linearity, hence generating harmonics in addition to the original desired sinusoid modulation. By measuring the transfer curve from input of the CMOS driver, to the output of the phase shifter, we are able to fit the parameters in the

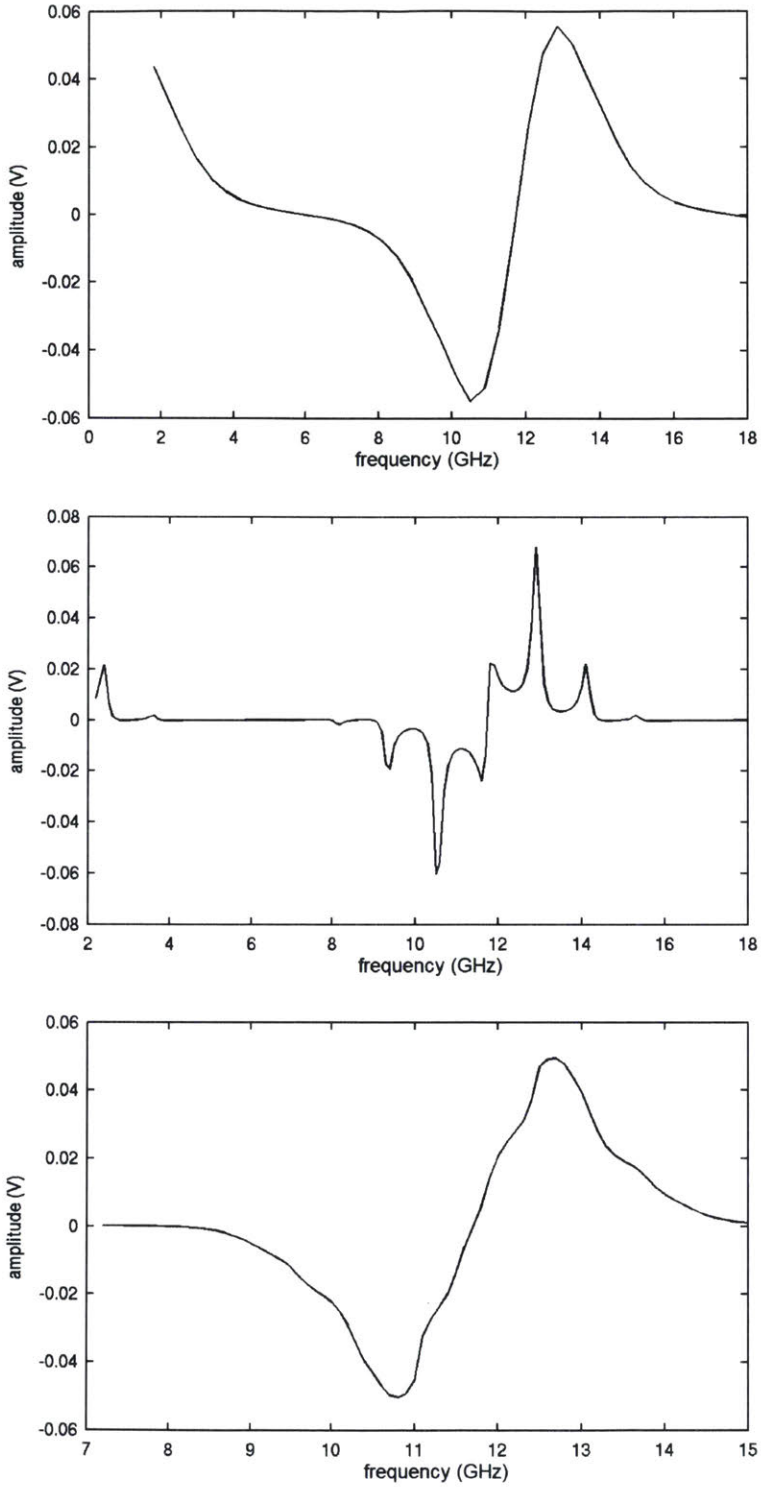

Figure 5-6: Top left: Error function at low modulation frequency (comparable to linewidth of resonant ring) Top right: high modulation frequency (20X linewidth) Bottom: CMOS low frequency modulation (including harmonics).77

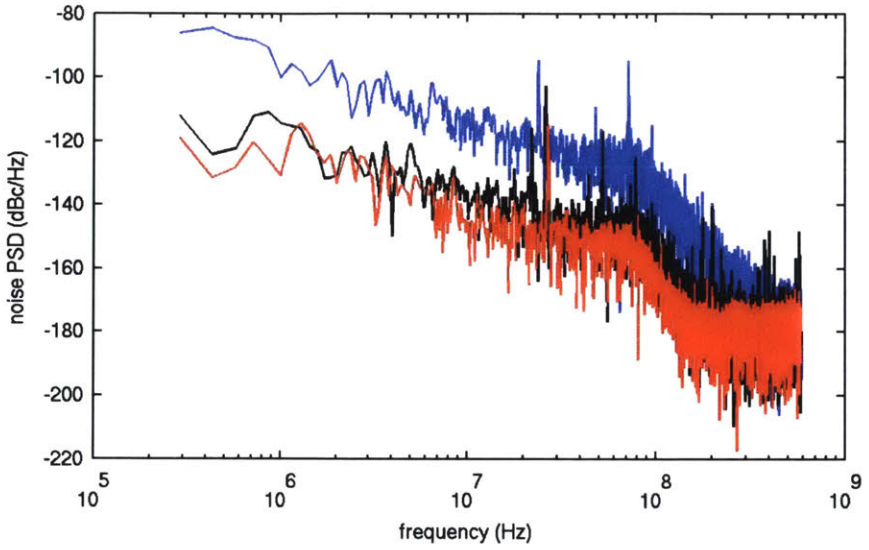

Figure 5-7: Phase noise PSD of PDH loop. Original laser output in blue, sine low frequency modulation in red, CMOS low frequency modulation in black.

polynomial phase shifter model(subsection 2.2.3), and simulate the PDH loop behavior with this non-ideality. We show in Figure 5-6 and 5-7 the error function of a few scenarios, and the resulting PDH performance. Compared to tabletop demonstrations, integrated silicon photonics have much more non-idealities for the sake of lower power and area, and these simulations can inform the designer what the trade space looks like.

5.2.4 Athermal Resonant Ring

To further verify the usefulness of this simulation tool, we can use the design parameters from a real-life experiment, and see if we can duplicate the results in our simulation. Using the design parameters from [60], we compare the resulting linewidths from a PDH locked to a nitride cavity verses a PDH locked to an athermal cavity.

As explained in the paper, in room temperature systems, the linewidth of a PDH loop is usually dominated by the frequency stability of the resonant ring. Temperature fluctuations impact the index of refraction and length of the waveguide, both of which alter the resonance frequency. We can modify the waveguide model by adding the temperature as an input,

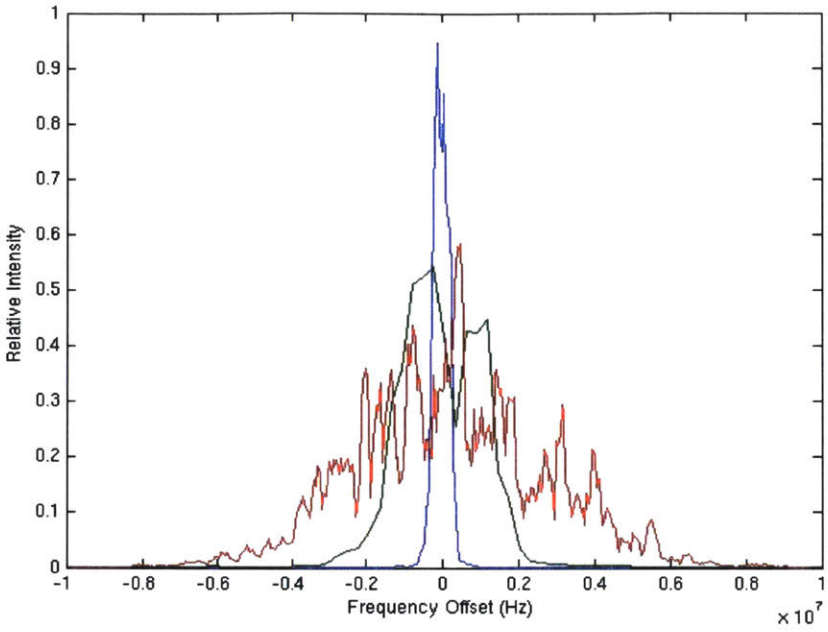

Figure 5-8: Linewidths of the free running CW laser (red), output of PDH locked to nitride cavity (green), and output of PDH locked to athermal cavity (blue).

and thermal dependency terms to the index of refraction and length. The exact power spectral density of the temperature is not known, but can be approximated by a $1/f$ noise distribution. The thermal dependency terms are reduced in the athermal resonant ring case to produce a narrower linewidth, as shown in figure 5-8.

5.3 Summary

This chapter presents two example systems, a WDM link and a PDH loop, and demonstrates how easily they can be simulated while accurately capturing important detail. By adding in measurement results from individual devices, we can simulate how they effect the system as a whole, and help the designer make design decisions in large and complex systems.

Chapter 6

Integrated Electro-optical Chip Design

In the earliest demonstrations of optical links with discrete components, the CMOS can be designed independent of the photonic device, as they are relatively isolated. For an electronic/photonic chip to be designed in a truly integrated fashion, there must be a photonic equivalent to every step of the CMOS design flow, and used in the same fashion with the same tools. Alongside the simulation toolkit, we also need include parametrized layout generation or p-cells, macro preparation for automated place and route, design rule checking (DRC) and layout vs. schematic checking (LVS).

6.1 Integration Methods

Traditional integration methods such as wirebond or bump bonding have a limited connection density, on the order of tens per millimeter squared. These approaches are quickly pad limited as process technology scales, so tighter integration methods are required, such as monolithic integration or 3D integration.

Monolithic integration leverages existing CMOS infrastructure, ranging from no change to the process [9], to a process that is customized for photonic applications [3]. Some advantages of this approach are accessibility, and less processing steps, which lead to lower costs. A big challenge for this approach are the constraints on the photonic device design,

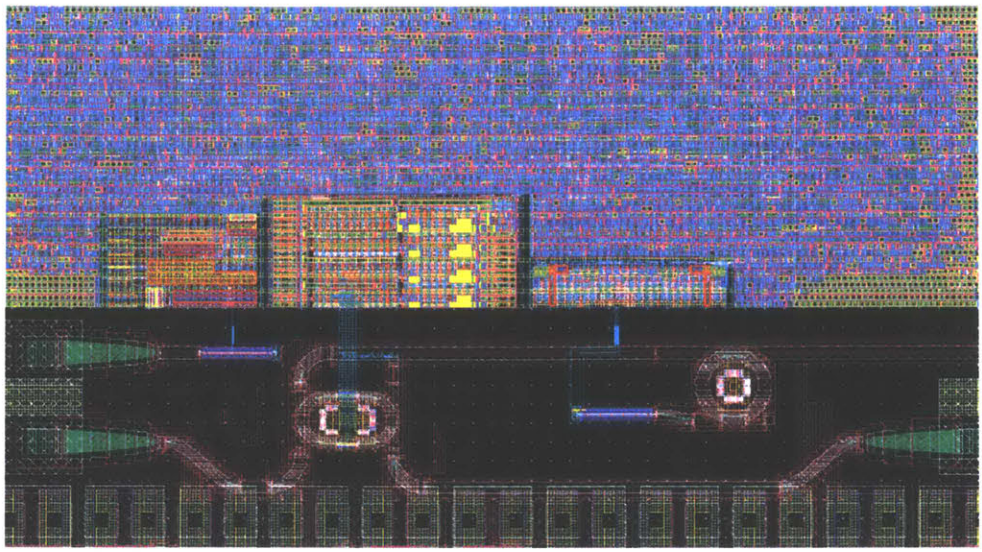

Figure 6-1: Layout of CMOS circuits on the same wafer layers as photonic devices.

as they and CMOS devices share the same wafer.

3D integration uses wafer bonding technology [162] [1] to connect separate wafers together. This allows the processing of the photonic wafer to be decoupled with the CMOS wafer, so there are more options (in terms of what elements can be used, doping profiles, etc.) for photonic device design, while at the same time allowing for more options on the CMOS side (more advanced nodes, bulk/SOI CMOS, etc.). [8] demonstrates that the technology for building chips with wafer bonding and thru-oxide vias (TOVs) at a high yield is maturing, and on the path for being accessible to designers.

6.2 Parametrized photonic layout generation and optimization

For layout of photonic structures, we have used p-cells to draw the photonic devices [161]. A p-cell lets the designer to input the design parameters of a device, and reflects the changes in the layout immediately. For instance, for a waveguide bend, the user and specify the waveguide width, bend radius, bend angle, etc. More parameters can be added later on if

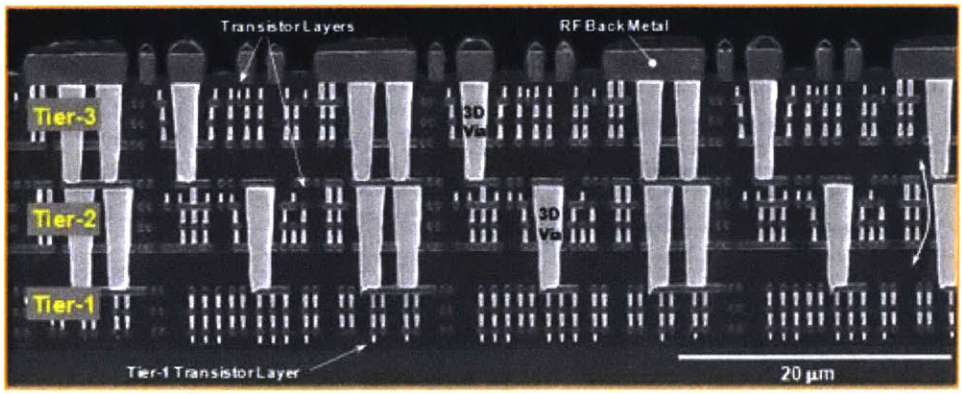

Figure 6-2: Cross-section SEM of three 150-nm 1.5V fully depleted SOI CMOS tiers showing oxide bonds and 3D via interconnects between circuit levels, including 3 transistor levels and 11 metal interconnect levels. [1]

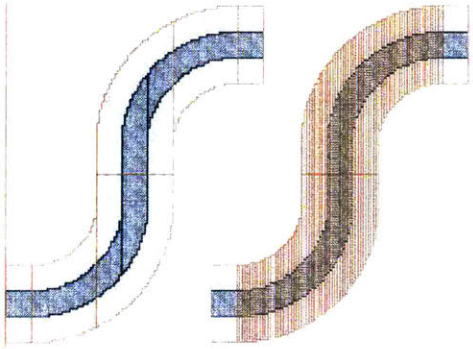

Figure 6-3: The waveguide on the left is drawn with polygons with many vertices; the waveguide on the right is drawn with just rectangles.

more degrees of freedom are needed. In stream-out, Cadence merges rectangles into many-vertex polygons (max 4000 vertices). So this means we can draw polygons with many vertices. One major benefit is redundant vertices are minimized, saving disk space. Also, Cadence displays simplified polygons when zoomed out, so the screen refreshes faster in a complex design. This effect is shown in Figure 6-3.

Larger structures are built hierarchically, such that higher level parameters are passed down to create lower level p-cell instances with the correct location, orientation, and other parameters. At the top level the designer writes a cadence SKILL script to instantiate all the photonic instances, so any changes in the lower level p-cell will be automatically reflected

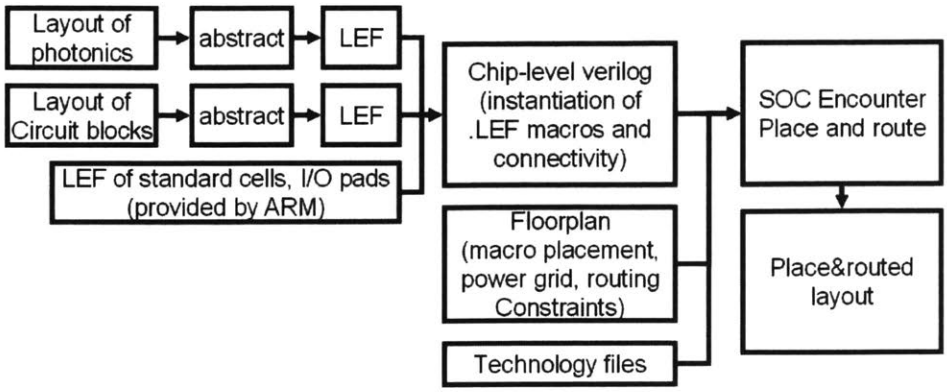

Figure 6-4: Integrated electric and photonic circuit design flow

in the overall design.

6.3 Design Automation of Electric and Photonic Integrated Circuits

For most commercial digital chips, the physical layout is done automatically with Computer Assisted Design (CAD) tools. The user starts with a behavioral description of the chip in Verilog that describes the functionality of the chip, then proceeds to synthesize the chip into a gate level design, where we have a netlist of logic gates. The next procedure is floor-planing, where the designer places the power wires, pads, and higher level module blocks of the chip. Finally a detailed place and route is performed, where the standard cell layout corresponding to each logic gate are placed and wired up. Modern CAD tools let the user adjust the optimization parameters, such as area, clock frequency, signal integrity etc, and warn the designer of bottlenecks and violations, so that many iterations can be quickly made, saving the designer a significant amount of time.

For photonics to be integrated in a complex chip, it also needs to be compatible with this CAD tool flow. This integrated electric and photonic circuit design flow is shown in Figure 6-4. We currently do not yet have the capability to synthesize the photonic structures needed based off of a behavioral description, that is in the works. Currently we rely on the

designer to decide exactly which photonic devices will be used, and how they are placed and optically connected. Beyond that step, we treat photonic blocks the same way as we treat logic gate standard cells.

To allow the CAD tool to place and route the photonic device, we need to create a macro description (using the industry standard LEF format) for each photonic device from the layout created in the method described in the p-cell section. This LEF file contains information about the device's size, metal layer geometries, and port geometries for electrical connections. The CAD tool needs to know the size of the device so that it can be tightly placed without overlapping with other devices. The metal layer geometries and port geometries allow the CAD tool to route signals to the correct ports as specified in the Verilog netlist.

As an example, a layout of a ring modulator is shown in Figure 6-5(a). After labeling the port names, an abstract can be generated, leaving only the essential layer information. Then from this abstract, we can create a LEF macro (abbreviated version shown in Figure **??**(b)), specifying the device name, size, port locations and metal geometries. To plug this back into the CMOS design flow, we simply reference these new libraries in the tool, add instantiations of photonic macros, and make connections to other macros, all as described in the Verilog code.

6.4 Simple design check using LVS and DRC

As we try to build truly integrated photonic-electrical circuits, LVS capability is crucial, since humans can only be error-free up to a certain complexity level. To indicate optical connectivity, we can use a layer that is unused by the electrical process, so the optical and electrical nets are independent of each other. We also add additional layers to help us extract optical devices and their parameters. Thus the extraction tool will be able to recognize photonic devices and compare the layout (Figure 6-6(a)) with the designed schematic (Figure 6-6(b)).

In addition to checking connectivity, by making the optical connectivity layer wider than the actual waveguide, LVS will detect a short if two waveguides are too close to each other.

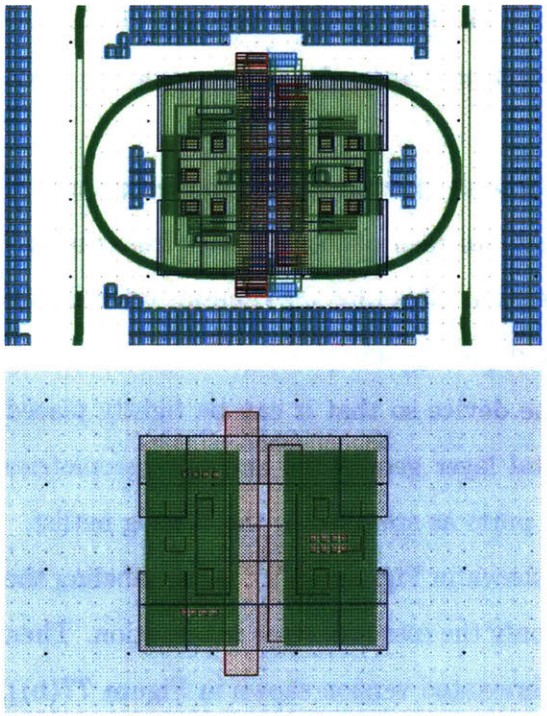

(a)

```
VERSION 5.6 ;
BUSBITCHARS "[]" ;
DIVIDERCHAR "/" ;

MACRO block_electronic_etch_row_1
  CLASS BLOCK ;
  ORIGIN -208 -1794 ;
  FOREIGN block_electronic_etch_row_1 208 1794 ;
  SIZE 2488 BY 165 ;
  SYMMETRY X Y R90 ;
  PIN heater_a_1
    DIRECTION INOUT ;
    USE SIGNAL ;
    PORT
      LAYER ua ;
        RECT 431 1870.5 436.5 1882 ;
    END
  END heater_a_1
...
  OBS
    LAYER m1 ;
      RECT 208 1794 2696 1959 ;
...
  END
END block_electronic_etch_row_1

END LIBRARY
```

(b)

Figure 6-5: (a) Layout and abstract views of example ring modulator. Note that lower level metal features such as metal fill have been blocked out, since port connections are made at higher levels. (b) Abbreviated macro description in LEF format of example ring modulator.

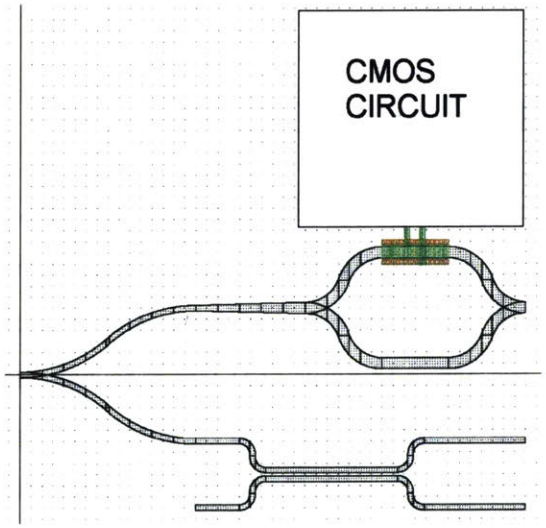

(a)

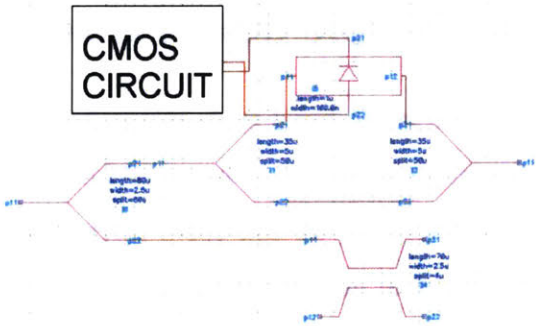

(b)

Figure 6-6: (a) Layout and (b) schematic of circuit with both photonic and electrical components.

Additional DRC checks may be made by adding rules to the DRC rules file. For example, we can check if the waveguides have the proper silicide, metal fill and dopant blocking layers overlapping them.

6.5 Summary

This chapter focuses on the integration of photonics with circuits from a design perspective. Using existing tools, we develop methods to draw photonic devices, verify the circuit and include the photonic devices within a standard CMOS place and route flow.

Appendix A

Code Samples

A.1 VerilogA Math Functions

```
//Complex number algebra in polar coordinates
//Jonathan Leu 2012

`include "constants.vams" //verilog A libraries - constants are pi, e, etc...
`include "disciplines.vams" //

//multiply module
// out = in1 * in2
module multiply(in1, in2, out);

        input        [0:1]        in1, in2;
        output        [0:1]        out;

        electrical        [0:1]        in1, in2, out;
        analog begin
                V(out[1]) <+ V(in1[1])*V(in2[1]);
                V(out[0]) <+ V(in1[0])+V(in2[0]);
        end
endmodule

//addition module
// out = in1 + in2
module addition(in1, in2, out);

        input        [0:1]        in1, in2;
        output        [0:1]        out;

        electrical        [0:1]        in1, in2, out;
        analog begin
                V(out[1]) <+ sqrt(pow(V(in1[1]),2)+pow(V(in2[1]),2)+2*V(in1[1])*V(in2[1])*cos(V(in1[0])-V(in2[0])));
                V(out[0]) <+ atan2((V(in1[1])*sin(V(in1[0]))+V(in2[1])*sin(V(in2[0]))),(V(in1[1])*cos(V(in1[0]))+V(in2[1])*cos(V(in2[0]))));
        end
endmodule
```

```
//exponent module
// out = exp(in)
module exponent(in, out);

        input        [0:1]        in;
        output        [0:1]        out;

        electrical        [0:1]        in, out;
        analog begin
                V(out[1]) <+ exp(V(in[1])*cos(V(in[0])));
                V(out[0]) <+ V(in[1])*sin(V(in[0]));
        end
endmodule

//polynomial module
// out = coeff*(in)^pwr
module polynom(in, pwr, coeff, out);

        input        [0:1]        in, coeff;
        input        pwr;
        output        [0:1]        out;
        electrical        pwr;
        electrical        [0:1]        in, out, coeff;
        analog begin
                V(out[1]) <+ pow(V(in[1]),V(pwr))*V(coeff[1]);
                V(out[0]) <+ V(in[0])*V(pwr)+V(coeff[0]);
        end
endmodule


//convert polar to cartiesian module
// out = [real, imaginary]
// in = [phase, mag]
module pol2cart(in, out);

        input        [0:1]        in;
        output        [0:1]        out;

        optical        [0:1]        in, out;
        analog begin
                E(out[0]) <+ E(in[1])*cos(E(in[0]));
                E(out[1]) <+ E(in[1])*sin(E(in[0]));
        end
endmodule

//convert cartiesian to polar module
// in = [real, imaginary]
// out = [phase, mag]
module cart2pol(in, out);

        input        [0:1]        in;
        output        [0:1]        out;

        optical        [0:1]        in, out;
        analog begin
                E(out[0]) <+ atan2(E(in[1]),E(in[0]));
                E(out[1]) <+ sqrt(E(in[0])*E(in[0])+E(in[1])*E(in[1]));
        end
```

```
endmodule


// below are cartesian modules!!!!
// [0] = real, [1] = imaginary
module cartadd(in1, in2, out);
        input        [0:1]        in1, in2;
        output        [0:1]        out;
        optical        [0:1]        in1, in2, out;
        analog begin
                E(out[0]) <+ E(in1[0]) + E(in2[0]);
                E(out[1]) <+ E(in1[1]) + E(in2[1]);
        end
endmodule

// [0] = real, [1] = imaginary
module cartmul(in1, in2, out);
        input        [0:1]        in1, in2;
        output        [0:1]        out;
        optical        [0:1]        in1, in2, out;
        analog begin
                E(out[0]) <+ E(in1[0])*E(in2[0])-E(in1[1])*E(in2[1]);
                E(out[1]) <+ E(in1[0])*E(in2[1]) + E(in1[1])*E(in2[0]);
        end
endmodule

// [0] = real, [1] = imaginary, returns in1/in2
module cartdiv(in1, in2, out);
        input        [0:1]        in1, in2;
        output        [0:1]        out;
        optical        [0:1]        in1, in2, out;
        analog begin
                E(out[0]) <+ (E(in1[0])*E(in2[0])+E(in1[1])*E(in2[1]))/(E(in2[0])*E(in2[0])+E(in2[1])*E(in2[1]));
                E(out[1]) <+ (E(in2[0])*E(in1[1]) - E(in2[1])*E(in1[0]))/(E(in2[0])*E(in2[0])+E(in2[1])*E(in2[1]));
        end
endmodule
%\end{verbnobox}
```

A.2 VerilogA Device Models

```
...
analog begin
    //calculate effective indices and effective loss based on applied voltages
    Va = V(vtop, vbot);
    neff = n0+n1*Va+n2*Va*Va+n3*pow(Va,3)+n4*pow(Va,4)+n5*pow(Va,5);
    ng = ng0+ng1*Va+ng2*Va*Va+ng3*pow(Va,3)+ng4*pow(Va,4)
          +ng5*pow(Va,5);
    aeff = a0+a1*Va+a2*Va*Va+a3*pow(Va,3)+a4*pow(Va,4)+a5*pow(Va,5);
    //calculate phase-shift and amplitude change in polar coordinates
    E(transfer[0]) <+ ((-1*neff*L*2*`M_PI*G_freq)/`P_C)%(2*`M_PI);
    E(transfer[1]) <+ exp(-aeff*L);
    // output delayed signals
    E(rightLight[0]) <+ absdelay(E(rightOutput[0]), L*ng/`P_C);
    E(rightLight[1]) <+ absdelay(E(rightOutput[1]), L*ng/`P_C);
    // and set backward propagation
    E(leftLight[2]) <+ absdelay(E(leftOutput[0]), L*ng/`P_C);
    E(leftLight[3]) <+ absdelay(E(leftOutput[1]), L*ng/`P_C);
end
...
```

Figure A-1: VerilogA phase-shifter model code. Va is the voltage applied across the phase shifter, and n0...n5, ng0...ng5, and a0...a5 are the coefficients governing the voltage to effective refractive index, effective group index, and effective loss respectively (as either calculated from device simulations or measured from experiment).

```
// set-up of code analogous to above, also see photodiode code below...
...
// electrical part:
    Vt  = `P_K*Temp/`P_Q;                          // kT/q = Thermal voltage [V]
    q_diode = - 2 * Cjo * Vbi * sqrt(1 - V(cap) / Vbi);  // diode charge
    if (V(cap) > Vbi) begin                        // diode must be used in reverse bias
        $strobe("photodiode voltage V(cap)>Vbi");
        $finish;
    end
    I(res) <+ Is * (limexp(V(res) / Vt) - 1);      // current through resistive branch [A]
    I(cap) <+ ddt(q_diode);                        // current through capacitive branch [A]
    V(rseries) <+ Rseries*(I(res)+I(cap));         // ohm's law equation for series

// optical part:
    Va = V(cap);
    neff = n0+n1*Va+...
...
// end of code analogous to above...
```

Figure A-2: VerilogA electrical reverse bias phase-shifter model code.

```
...
parameter real L = 0.0005;      // length
parameter real ng = 4.1963;     // group index
parameter real n0 = 2.1;        // refractive index with no heating
parameter real Zt = 57000;      // thermal impedance
parameter real R0 = 2000;       // Resistance
parameter real h = 1.9E-4;      // heat transfer coefficient
parameter real nT = 0.0001;     // change in index with temperature
 parameter real T0 = 293;       // ambient temperature
parameter real a0 = 0.0;        // waveguide loss
parameter real a1 = 0.0;        // voltage dependence of waveguide loss (da/dV)
...
optical [0:1] heaterPol;
optical [0:1] heaterCart;
thermal Htemp;
...
pol2cart convs1(heaterPol, heaterCart);
cartmul multout1(heaterCart, leftLight[1:0], rightOutput);
cartmul multout1B(heaterCart, rightLight[2:3], leftOutput);
...
analog begin
    Va = V(vtop, vbot);
    Temp(Htemp) <+ T0+ idt(Zt*Va*Va/R0-h*(Temp(Htemp)-T0),0);  // Waveguide temperature
    neff = n0+nT*Temp(Htemp);                  // Temperature induced phase change
    alphaeff = a0+a1*Va;                       // Loss
    // Calculate phase shift and amplitude change in polar coordinates
    E(heaterPol[0]) <+ (-1*neff*L*2*`M_PI*(G_freq/`P_C)%(2*`M_PI);
    E(heaterPol[1]) <+ limexp(alphaeff*1e-4*L);

    // Output delayed signals
    E(rightLight[0]) <+ absdelay(E(rightOutput[0]), L*ng/`P_C);
    E(rightLight[1]) <+ absdelay(E(rightOutput[1]), L*ng/`P_C);
    E(leftLight[2]) <+ absdelay(E(leftOutput[0]), L*ng/`P_C);
    E(leftLight[3]) <+ absdelay(E(leftOutput[1]), L*ng/`P_C);
end
...
```

Figure A-3: VerilogA thermal phase-shifter model code.

```
`include "../../../../cad/constants.vams"
`include "../../../../cad/disciplines.vams"

module Waveguide_Coupler(leftLight1, leftLight2, rightLight1, rightLight2);
  inout  [0:3]  leftLight1, leftLight2, rightLight1, rightLight2; // [0:1] is left side input, [2:3] is
  left side output
  optical [0:3]  leftLight1, leftLight2, rightLight1, rightLight2;

  // Physical Design Parameters, all units in SI
  parameter real kappa = 0.5;          // kappa is FIELD coupling
  parameter real G_freq = 1.93e14;  // reference frequency parameter passed in from top level
  simulation

  // Initialize intermediate points
  optical [0:1] Xcoup;
  optical [0:1] Xthru;
  optical [0:1] leftLig1X;
  optical [0:1] leftLig2X;
  optical [0:1] leftLig1T;
  optical [0:1] leftLig2T;
  optical [0:1] Xcoup2;
  optical [0:1] rightLig1X;
  optical [0:1] rightLig2X;
  optical [0:1] rightLig1T;
  optical [0:1] rightLig2T;

  analog begin
    // Calculate coupling matrix
    E(Xcoup[0]) <+ 0.0;
    E(Xcoup[1]) <+ -kappa;
    E(Xcoup2[0]) <+ 0.0;
    E(Xcoup2[1]) <+ -kappa;
    E(Xthru[0]) <+ sqrt(1-kappa*kappa);
    E(Xthru[1]) <+ 0;
  end
  // Forward propagating wave:
  cartmul in1X(leftLig1[0:1], Xcoup2, leftLig1X);
  cartmul in2X(leftLig2[0:1], Xcoup, leftLig2X);
  cartmul in1T(leftLig1[0:1], Xthru, leftLig1T);
  cartmul in2T(leftLig2[0:1], Xthru, leftLig2T);
  cartadd comb1(leftLig1T, leftLig2X, rightLig1[0:1]);
  cartadd comb2(leftLig1X, leftLig2T, rightLig2[0:1]);
  // Backward propagating wave
  cartmul Bin1X(rightLig1[2:3], Xcoup2, rightLig1X);
  cartmul Bin2X(rightLig2[2:3], Xcoup, rightLig2X);
  cartmul Bin1T(rightLig1[2:3], Xthru, rightLig1T);
  cartmul Bin2T(rightLig2[2:3], Xthru, rightLig2T);
  cartadd Bcomb1(rightLig1T, rightLig2X, leftLig1[2:3]);
  cartadd Bcomb2(rightLig1X, rightLig2T, leftLig2[2:3]);
endmodule
```

Figure A-4: VerilogA optical coupler model code. "cartadd" performs comples addition on the real and imaginary signals.

```
`include "../../../../cad/constants.vams"
`include "../../../../cad/disciplines.vams"

module PD_Electrical(p, n, inLight);
  inout [0:3]  inLight;
  inout        p, n;
  electrical   p, n;
  optical [0:3] inLight;

  // Declare an internal node and branches
  electrical inter;
  branch (p,inter) cap, res, photo;
  branch (inter,n) rseries;
  // Physical Design Parameters
  parameter real Temp=300;          // In Kelvins
  // Derived Parameter Declarations
  parameter real Is=1e-12;          // Reverse-bias saturation current [A]
  real Vt;                          // Thermal voltage [V]
  parameter real Vbi=1;             // Built-in voltage [V]
  parameter real Cjo=1e-15;         // Unbiased junction capacitance [F]
  parameter real tau=1e-100;        // response time constant 10ps
  parameter real Rseries = 1.0;     //series resistance of diode [Ohms]
  real q_diode;                     // Charge in diode [C]
  // Optical Constants
  parameter real responsivity = 0.8;
  analog begin
    // Calculate Derived Parameters
    Vt  = `P_K*Temp/`P_Q;                          // Thermal voltage [V]
    q_diode = - 2 * Cjo * Vbi * sqrt(1 - V(cap) / Vbi); // Charge
    if (V(cap) > Vbi) begin                        // Diode must be used in reverse bias
        $strobe("photodiode voltage V(cap)>Vbi");
        $finish;
    end
    // Calculate photocurrent, filter by time constant
    I(photo) <+ laplace_nd(-responsivity*(pow(E(inlig[1]),2)+pow(E(inlig[0]),2)), {1}, {1,1/tau});
                                                   // Photocurrent
    I(res) <+ Is * (limexp(V(res) / Vt) - 1);      // Current through resistive branch [A]
    I(cap) <+ ddt(q_diode);                        // Current through capacitive branch [A]
    V(rseries) <+ Rseries*(I(res)+I(cap)+I(photo)); // Ohm's law equation for series resistance
    // This model assumes no reflections
    E(inLight[2]) <+ 0.0;
    E(inLight[3]) <+ 0.0;
  end
endmodule
```

Figure A-5: VerilogA photo-detector model code.

Bibliography

[1] J. A. Burns, B. F. Aull, C.-L. Chen, C.-L. Chen, C. L. Keast, J. M. Knecht, V. Suntharalingam, K. Warner, P. W. Wyatt, and D.-R. W. Yost, "A wafer-scale 3-d circuit integration technology," *Electron Devices, IEEE Transactions on*, vol. 53, no. 10, pp. 2507–2516, 2006.

[2] C. Batten, A. Joshi, J. Orcutt, C. Holzwarth, M. Popovic, J. Hoyt, F. Kartner, R. Ram, V. Stojanovic, and K. Asanovic, "Building manycore processor-to-dram networks with monolithic cmos silicon photonics," *Micro, IEEE*, vol. PP, no. 99, p. 1, 2009.

[3] C. Gunn, "Cmos photonics for high-speed interconnects," *Micro, IEEE*, vol. 26, no. 2, pp. 58–66, 2006.

[4] Y. Vlasov, W. M. Green, and F. Xia, "High-throughput silicon nanophotonic wavelength-insensitive switch for on-chip optical networks," *Nature Photonics*, vol. 2, no. 4, pp. 242–246, 2008.

[5] J. Sun, E. Timurdogan, A. Yaacobi, E. S. Hosseini, and M. R. Watts, "Large-scale nanophotonic phased array," *Nature*, vol. 493, no. 7431, pp. 195–199, 2013.

[6] A. Khilo, S. J. Spector, M. E. Grein, A. H. Nejadmalayeri, C. W. Holzwarth, M. Y. Sander, M. S. Dahlem, M. Y. Peng, M. W. Geis, N. A. DiLello, J. U. Yoon, A. Motamedi, J. S. Orcutt, J. P. Wang, C. M. Sorace-Agaskar, M. A. Popović, J. Sun, G.-R. Zhou, H. Byun, J. Chen, J. L. Hoyt, H. I. Smith, R. J. Ram, M. Perrott, T. M. Lyszczarz, E. P. Ippen, and F. X. Kärtner, "Photonic adc: overcoming the bottleneck of electronic jitter," *Opt. Express*, vol. 20, pp. 4454–4469, Feb 2012.

[7] A. V. Krishnamoorthy and K. W. Goossen, "Optoelectronic-vlsi: photonics integrated with vlsi circuits," *IEEE Journal of Selected Topics in Quantum Electronics*, vol. 4, pp. 899–912, Nov 1998.

[8] K. T. Settaluri, S. Lin, S. Moazeni, E. Timurdogan, C. Sun, M. Moresco, Z. Su, Y. H. Chen, G. Leake, D. LaTulipe, C. McDonough, J. Hebding, D. Coolbaugh, M. Watts, and V. StojanoviÄĞ, "Demonstration of an optical chip-to-chip link in a 3d integrated electronic-photonic platform," in *European Solid-State Circuits Conference (ESSCIRC), ESSCIRC 2015 - 41st*, pp. 156–159, Sept 2015.

[9] C. Sun, M. T. Wade, Y. Lee, J. S. Orcutt, L. Alloatti, M. S. Georgas, A. S. Waterman, J. M. Shainline, R. R. Avizienis, S. Lin, *et al.*, "Single-chip microprocessor that communicates directly using light," *Nature*, vol. 528, no. 7583, pp. 534–538, 2015.

[10] J. Orcutt and R. Ram, "Photonic device layout within the foundry cmos design environment," *Photonics Technology Letters, IEEE*, vol. 22, pp. 544–546, April 2010.

[11] A. F. Oskooi, D. Roundy, M. Ibanescu, P. Bermel, J. Joannopoulos, and S. G. Johnson, "Meep: A flexible free-software package for electromagnetic simulations by the fdtd method," *Computer Physics Communications*, vol. 181, no. 3, pp. 687–702, 2010.

[12] J. Morikuni and S. Kang, "Optoelectronic simulation at the device and circuit level," in *Integrated Optoelectronics, 1994., Proceedings of IEE/LEOS Summer Topical Meetings:*, pp. 1_8–1_9, IEEE, 1994.

[13] T. Smy and P. Gunupudi, "Robust simulation of opto-electronic systems by alternating complex envelope representations," *Computer-Aided Design of Integrated Circuits and Systems, IEEE Transactions on*, vol. 31, no. 7, pp. 1139–1143, 2012.

[14] T. Smy, M. Freitas, and V. Ambalavanar, "Self-consistent opto-thermal-electronic simulation of micro-rings for photonic macrochip integration," in *Optical Interconnects Conference, 2012 IEEE*, pp. 68–69, IEEE, 2012.

[15] A. Lowery, O. Lenzmann, I. Koltchanov, R. Moosburger, R. Freund, A. Richter, S. Georgi, D. Breuer, and H. Hamster, "Multiple signal representation simulation of photonic devices, systems, and networks," *Selected Topics in Quantum Electronics, IEEE Journal of*, vol. 6, no. 2, pp. 282–296, 2000.

[16] B. Wang, I. O'Connor, E. Drouard, and L. Labrak, "Bottom-up verification methodology for cmos photonic linear heterogeneous system," in *Specification & Design Languages (FDL 2010), 2010 Forum on*, pp. 1–6, IET, 2010.

[17] S. Fathpour and B. Jalali, *Silicon photonics for telecommunications and biomedicine*. CRC Press, 2011.

[18] Lumerical, *INTERCONNECT Circuit Solver*. `https://www.lumerical.com/support/whitepaper/interconnect_circuit_solver`, 2012.

[19] PICWave, *PICWave, A photonic IC, laser diode and SOA simulator*. `http://www.photond.com/products/picwave.htm`, 2012.

[20] P. Martin, F. Gays, E. Grellier, A. Myko, and S. Menezo, "Modeling of silicon photonics devices with verilog-a," in *2014 29th International Conference on Microelectronics Proceedings-MIEL 2014*, 2014.

[21] K. Takeda, K. Honda, T. Takeya, K. Okazaki, T. Hiraki, T. Tsuchizawa, H. Nishi, R. Kou, H. Fukuda, M. Usui, *et al.*, "Comprehensive photonics-electronics convergent simulation and its application to high-speed electronic circuit integration on a si/ge photonic chip," in *SPIE OPTO*, pp. 938806–938806, International Society for Optics and Photonics, 2015.

[22] D. F. Gallagher and T. Felici, "Modelling of silicon and active photonic integrated circuits," in *Photonics Europe*, pp. 69961E–69961E, International Society for Optics and Photonics, 2008.

[23] VPI, *VPIcomponentMaker Photonic Circuits.* `http://www.vpiphotonics.com/Tools/PhotonicCircuits/`, 2012.

[24] M. Fiers, T. Van Vaerenbergh, K. Caluwaerts, D. Vande Ginste, B. Schrauwen, J. Dambre, and P. Bienstman, "Time-domain and frequency-domain modeling of nonlinear optical components at the circuit-level using a node-based approach," *JOSA B*, vol. 29, no. 5, pp. 896–900, 2012.

[25] E. D. Black, "An introduction to pound–drever–hall laser frequency stabilization," *American Journal of Physics*, vol. 69, no. 1, pp. 79–87, 2001.

[26] K. Kundert, H. Chang, D. Jefferies, G. Lamant, E. Malavasi, and F. Sendig, "Design of mixed-signal systems-on-a-chip," *Computer-Aided Design of Integrated Circuits and Systems, IEEE Transactions on*, vol. 19, no. 12, pp. 1561–1571, 2000.

[27] M. De Wilde, O. Rits, R. Bockstaele, J. M. Van Campenhout, and R. G. Baets, "Circuit-level simulation approach to analyze system-level behavior of vcsel-based optical interconnects," in *Photonics Fabrication Europe*, pp. 247–257, International Society for Optics and Photonics, 2003.

[28] A. Mekis, D. Kucharski, G. Masini, and T. Pinguet, "Computer-aided design for cmos photonics," *Silicon Photonics for Telecommunications and BiomedicineâĂİ Edited by S. Fathpour and B. Jalali*, 2011.

[29] K. Zhu, V. Saxena, and W. Kuang, "Compact verilog-a modeling of silicon traveling-wave modulator for hybrid cmos photonic circuit design," in *Circuits and Systems (MWSCAS), 2014 IEEE 57th International Midwest Symposium on*, pp. 615–618, IEEE, 2014.

[30] B. B. R. Moss, *High-speed modulation of resonant CMOS photonic modulators in deep-submicron bulk-CMOS.* PhD thesis, Massachusetts Institute of Technology, 2009.

[31] J. Rhim, Y. Ban, B.-M. Yu, J.-M. Lee, and W.-Y. Choi, "Verilog-a behavioral model for resonance-modulated silicon micro-ring modulator," *Optics express*, vol. 23, no. 7, pp. 8762–8772, 2015.

[32] G. Giustolisi, R. Mita, and G. Palumbo, "Behavioral modeling of statistical phenomena of single-photon avalanche diodes," *International Journal of Circuit Theory and Applications*, vol. 40, no. 7, pp. 661–679, 2012.

[33] B. Blanco-Filgueira, P. López, and J. Roldán, "A verilog-ams photodiode model including lateral effects," *Microelectronics Journal*, vol. 43, no. 12, pp. 980–984, 2012.

[34] A. V. Oppenheim, R. W. Schafer, J. R. Buck, *et al.*, *Discrete-time signal processing*, vol. 2. Prentice-hall Englewood Cliffs, 1989.

[35] S. L. Marple Jr, "Computing the discrete-time âĂIJanalyticâĂİ signal via fft," *Signal Processing, IEEE Transactions on*, vol. 47, no. 9, pp. 2600–2603, 1999.

[36] R. Amatya, *Optimization of tunable silicon compatible microring filters*. PhD thesis, Massachusetts Institute of Technology, 2006.

[37] J. D. Jackson and J. D. Jackson, *Classical electrodynamics*, vol. 3. Wiley New York etc., 1962.

[38] D. J. Griffiths and R. College, *Introduction to electrodynamics*, vol. 3. prentice Hall Upper Saddle River, NJ, 1999.

[39] L. N. Binh, *Photonic signal processing: techniques and applications*. CRC Press, 2008.

[40] T. A. Ramadan, R. Scarmozzino, and R. M. Osgood, "Adiabatic couplers: design rules and optimization," *Journal of lightwave technology*, vol. 16, no. 2, p. 277, 1998.

[41] C. T. DeRose, D. C. Trotter, W. A. Zortman, A. L. Starbuck, M. Fisher, M. R. Watts, and P. S. Davids, "Ultra compact 45 ghz cmos compatible germanium waveguide photodiode with low dark current," *Optics express*, vol. 19, no. 25, pp. 24897–24904, 2011.

[42] S. M. Sze and K. K. Ng, *Physics of semiconductor devices*. John Wiley & Sons, 2006.

[43] E. Timurdogan, C. M. Sorace-Agaskar, J. Sun, E. S. Hosseini, A. Biberman, and M. R. Watts, "An ultralow power athermal silicon modulator," *Nature communications*, vol. 5, 2014.

[44] M. Dasic, M. Popovic, *et al.*, "Minimum drop-loss design of microphotonic microring-resonator channel add-drop filters," in *Telecommunications Forum (TELFOR), 2012 20th*, pp. 927–930, IEEE, 2012.

[45] S. Shimotsu, S. Oikawa, T. Saitou, N. Mitsugi, K. Kubodera, T. Kawanishi, and M. Izutsu, "Single side-band modulation performance of a linbo 3 integrated modulator consisting of four-phase modulator waveguides," *Photonics Technology Letters, IEEE*, vol. 13, no. 4, pp. 364–366, 2001.

[46] M. Dentan and B. de Cremoux, "Numerical simulation of the nonlinear response of a p-i-n photodiode under high illumination," *Journal of Lightwave Technology*, vol. 8, pp. 1137–1144, Aug 1990.

[47] H. Bahrami, H. Sepehrian, C. S. Park, L. A. Rusch, and W. Shi, "Time-domain large-signal modeling of traveling-wave modulators on soi," *Journal of Lightwave Technology*, vol. 34, pp. 2812–2823, June 2016.

[48] D. E. Crivelli, H. S. Carter, and M. R. Hueda, "Adaptive digital equalization in the presence of chromatic dispersion, pmd, and phase noise in coherent fiber optic systems," in *Global Telecommunications Conference, 2004. GLOBECOM '04. IEEE*, vol. 4, pp. 2545–2551 Vol.4, Nov 2004.

[49] G. P. Agrawal, *Nonlinear fiber optics*. Academic press, 2007.

[50] S. J. Savory, "Digital filters for coherent optical receivers," *Optics Express*, vol. 16, no. 2, pp. 804–817, 2008.

[51] M. Tateda, N. Shibata, and S. Seikai, "Interferometric method for chromatic dispersion measurement in a single-mode optical fiber," *IEEE Journal of Quantum Electronics*, vol. 17, no. 3, pp. 404–407, 1981.

[52] P. Merritt, R. P. Tatam, and D. A. Jackson, "Interferometric chromatic dispersion measurements on short lengths of monomode optical fiber," *Journal of Lightwave Technology*, vol. 7, no. 4, pp. 703–716, 1989.

[53] C. Sorace-Agaskar, J. Leu, M. R. Watts, and V. Stojanovic, "Electro-optical co-simulation for integrated cmos photonic circuits with veriloga," *Opt. Express*, vol. 23, pp. 27180–27203, Oct 2015.

[54] R. Dekker, N. Usechak, M. Först, and A. Driessen, "Ultrafast nonlinear all-optical processes in silicon-on-insulator waveguides," *Journal of physics D: applied physics*, vol. 40, no. 14, p. R249, 2007.

[55] G. T. Reed and C. J. Png, "Silicon optical modulators," *Materials Today*, vol. 8, no. 1, pp. 40 - 50, 2005.

[56] J. Shao, X. Liang, and S. Kumar, "Comparison of split-step fourier schemes for simulating fiber optic communication systems," *IEEE Photonics Journal*, vol. 6, pp. 1–15, Aug 2014.

[57] W. Bogaerts, P. De Heyn, T. Van Vaerenbergh, K. De Vos, S. Kumar Selvaraja, T. Claes, P. Dumon, P. Bienstman, D. Van Thourhout, and R. Baets, "Silicon microring resonators," *Laser & Photonics Reviews*, vol. 6, no. 1, pp. 47–73, 2012.

[58] T. J. Johnson, M. Borselli, and O. Painter, "Self-induced optical modulation of the transmission through a high-q silicon microdisk resonator," *Opt. Express*, vol. 14, pp. 817–831, Jan 2006.

[59] M. Georgas, J. Leu, B. Moss, C. Sun, and V. Stojanovic, "Addressing link-level design tradeoffs for integrated photonic interconnects," in *Custom Integrated Circuits Conference (CICC), 2011 IEEE*, pp. 1–8, Sept 2011.

[60] E. S. Magden, M. Y. Peng, J. D. B. Bradley, G. Leake, D. D. Coolbaugh, L. A. Kolodziejski, F. X. KÃd'rtner, and M. R. Watts, "Laser frequency stabilization using pound-drever-hall technique with an integrated tio2 athermal resonator," in *2016 Conference on Lasers and Electro-Optics (CLEO)*, pp. 1–2, June 2016.

[61] J. Leu and V. StojanoviÄĞ, "Injection-locked clock receiver for monolithic optical link in 45nm soi," in *Solid State Circuits Conference (A-SSCC), 2011 IEEE Asian*, pp. 149–152, Nov 2011.

[62] J. Morikuni and S.-M. Kang, "Optoelectronic simulation at the device and circuit level," in *Integrated Optoelectronics, 1994., Proceedings of IEE/LEOS Summer Topical Meetings*, Jul 1994.

[63] T. Smy, M. Freitas, and V. Ambalavanar, "Self-consistent opto-thermal-electronic simulation of micro-rings for photonic macrochip integration," in *Optical Interconnects Conference, 2012 IEEE*, pp. 68–69, May 2012.

[64] A. Lowery, O. Lenzmann, I. Koltchanov, R. Moosburger, R. Freund, A. Richter, S. Georgi, D. Breuer, and H. Hamster, "Multiple signal representation simulation of photonic devices, systems, and networks," *Selected Topics in Quantum Electronics, IEEE Journal of*, vol. 6, pp. 282–296, March 2000.

[65] K. Kundert, H. Chang, D. Jefferies, G. Lamant, E. Malavasi, and F. Sendig, "Design of mixed-signal systems-on-a-chip," *Computer-Aided Design of Integrated Circuits and Systems, IEEE Transactions on*, vol. 19, pp. 1561–1571, Dec 2000.

[66] M. Dasic and M. Popovic, "Minimum drop-loss design of microphotonic microring-resonator channel add-drop filters," in *Telecommunications Forum (TELFOR), 2012 20th*, pp. 927–930, Nov 2012.

[67] S. Shimotsu, S. Oikawa, T. Saitou, N. Mitsugi, K. Kubodera, T. Kawanishi, and M. Izutsu, "Single side-band modulation performance of a linbo3 integrated modulator consisting of four-phase modulator waveguides," *Photonics Technology Letters, IEEE*, vol. 13, pp. 364–366, April 2001.

[68] B. Wang, I. O'Connor, E. Drouard, and L. Labrak, "Bottom-up verification methodology for cmos photonic linear heterogeneous system," in *Specification Design Languages (FDL 2010), 2010 Forum on*, pp. 1–6, Sept 2010.

[69] C. Batten, A. Joshi, J. Orcutt, A. Khilo, B. Moss, C. Holzwarth, M. Popovic, H. Li, H. Smith, J. Hoyt, F. Kartner, R. Ram, V. Stojanovic, and K. Asanovic, "Building manycore processor-to-dram networks with monolithic silicon photonics," *HOTI '08*, pp. 21–30, Aug. 2008.

[70] T. Barwicz, H. Byun, F. Gan, C. W. Holzwarth, M. A. Popovic, P. T. Rakich, M. R. Watts, E. P. Ippen, F. X. Kartner, H. I. Smith, J. S. Orcutt, R. J. Ram, V. Stojanovic, O. O. Olubuyide, J. L. Hoyt, S. Spector, M. Geis, M. Grein, T. Lyszczarz, and J. U. Yoon, "Silicon photonics for compact, energy-efficient interconnects," *J. Opt. Netw.*, vol. 6, no. 1, pp. 63–73, 2007.

[71] A. Abdi and M. Kaveh, "A space-time correlation model for multielement antenna systems in mobile fading channels," *IEEE J. Select. Aeras Commun.*, vol. 20, pp. 550–560, April 2002.

[72] J. del Alamo and D.-H. Kim, "Beyond cmos: Logic suitability of ingaas hemts," *Indium Phosphide & Related Materials, 2007. IPRM '07. IEEE 19th International Conference on*, pp. 51–54, May 2007.

[73] P. Alfke, "Efficient shift registers, lfsr counters, and long pseudo-random sequence generators," tech. rep., Xilinx, 1996.

[74] B. Wang, I. O'Connor, and E. Drouard, "Passive components modeling for optical network-on-chip," in *Passive Components and Fiber-Based Devices VII*, p. 798603, Optical Society of America, 2010.

[75] E. Alon, V. Stojanovic, and M. Horowitz, "Circuits and techniques for high-resolution measurement of on-chip power supply noise," *Solid-State Circuits, IEEE Journal of*, vol. 40, pp. 820–828, April 2005.

[76] B. Analui, D. Guckenberger, D. Kucharski, and A. Narasimha, "A fully integrated 20-gb/s optoelectronic transceiver implemented in a standard 0.13- um cmos soi technology," *Solid-State Circuits, IEEE Journal of*, vol. 41, pp. 2945–2955, Dec. 2006.

[77] M. Baker and R. Sarpeshkar, "Feedback analysis and design of rf power links for low-power bionic systems," *Biomedical Circuits and Systems, IEEE Transactions on*, vol. 1, pp. 28–38, March 2007.

[78] M. Baker and R. Sarpeshkar, "A low-power high-psrr current-mode microphone preamplifier," *Solid-State Circuits, IEEE Journal of*, vol. 38, pp. 1671–1678, Oct. 2003.

[79] R. Beausoleil, P. Kuekes, G. Snider, S.-Y. Wang, and R. Williams, "Nanoelectronic and nanophotonic interconnect," *Proceedings of the IEEE*, vol. 96, pp. 230–247, Feb. 2008.

[80] J. Croon, M. Rosmeulen, S. Decoutere, W. Sansen, and H. Maes, "An easy-to-use mismatch model for the mos transistor," *Solid-State Circuits, IEEE Journal of*, vol. 37, pp. 1056–1064, Aug 2002.

[81] C. Debaes, A. Bhatnagar, D. Agarwal, R. Chen, G. Keeler, N. Helman, H. Thienpont, and D. Miller, "Receiver-less optical clock injection for clock distribution networks," *Selected Topics in Quantum Electronics, IEEE Journal of*, vol. 9, pp. 400–409, March-April 2003.

[82] G. Dewey, M. Hudait, K. Lee, R. Pillarisetty, W. Rachmady, M. Radosavljevic, T. Rakshit, and R. Chau, "Carrier transport in high-mobility iiiŨv quantum-well transistors and performance impact for high-speed low-power logic applications," *Electron Device Letters, IEEE*, vol. 29, pp. 1094–1097, Oct. 2008.

[83] A. Emami-Neyestanak, D. Liu, G. Keeler, N. Helman, and M. Horowitz, "A 1.6 gb/s, 3 mw cmos receiver for optical communication," *VLSI Circuits Digest of Technical Papers, 2002. Symposium on*, pp. 84–87, 2002.

[84] K. Fukuda, H. Yamashita, G. Ono, R. Nemoto, E. Suzuki, N. Masuda, T. Takemoto, F. Yuki, and T. Saito, "A 12.3-mw 12.5-gb/s complete transceiver in 65-nm cmos process," *JSSC*, vol. 45, pp. 2838 –2849, dec. 2010.

[85] M. Georgas, J. Orcutt, R. Ram, and V. Stojanovic, "A monolithically-integrated optical receiver in standard 45-nm soi," in *ESSCIRC (ESSCIRC), 2011 Proceedings of the*, pp. 407 –410, sept. 2011.

[86] G. Gerosa, S. Gary, C. Dietz, D. Pham, K. Hoover, J. Alvarez, H. Sanchez, P. Ippolito, T. Ngo, S. Litch, J. Eno, J. Golab, N. Vanderschaaf, and J. Kahle, "A 2.2 w, 80 mhz superscalar risc microprocessor," *Solid-State Circuits, IEEE Journal of*, vol. 29, pp. 1440–1454, Dec 1994.

[87] S. Haykin and M. Moher, *Introduction to Analog & Digital Communications (Second Edition)*. John Wiley & Sons, 2007.

[88] C. Holzwarth, J. Orcutt, H. Li, M. Popovic, V. Stojanovic, J. Hoyt, R. Ram, and H. Smith, "Localized substrate removal technique enabling strong-confinement microphotonics in bulk si cmos processes," *Lasers and Electro-Optics, 2008 and 2008 Conference on Quantum Electronics and Laser Science. CLEO/QELS 2008. Conference on*, pp. 1–2, May 2008.

[89] B. Moss, *A 10 Gb/s Optical Modulator in 32 nm Bulk-CMOS*. PhD thesis, Massachusetts Institute of Technology, USA, 2009.

[90] U. Feiste, D. As, and A. Ehrhardt, "18 ghz all-optical frequency locking and clock recovery using a self-pulsating two-section dfb-laser," *Photonics Technology Letters, IEEE*, vol. 6, pp. 106 –108, jan 1994.

[91] W. Mao, Y. Li, M. Al-Mumin, and G. Li, "40 gbit/s all-optical clock recovery using two-section gain-coupled dfb laser and semiconductor optical amplifier," *Electronics Letters*, vol. 37, pp. 1302 –1303, 11 2001.

[92] M. Leiria, I. Kim, A. Cartaxo, and G. Li, "Experimental study of pattern-independent phase noise accumulation in an all-optical clock recovery chain based on two-section gain-coupled dfb lasers," *Lightwave Technology, Journal of*, vol. 26, pp. 1661 –1670, june15, 2008.

[93] W. Mao, Y. Li, M. Al-Mumin, and G. Li, "40 gbit/s all-optical clock recovery using two-section gain-coupled dfb laser and semiconductor optical amplifier," *Electronics Letters*, vol. 37, pp. 1302 –1303, 11 2001.

[94] K. Yvind, D. Larsson, L. Christiansen, J. Mork, J. Hvam, and J. Hanberg, "High-performance 10 ghz all-active monolithic modelocked semiconductor lasers," *Electronics Letters*, vol. 40, pp. 735 – 737, 10 2004.

[95] X. Wang, H. Yokoyama, and T. Shimizu, "Synchronized harmonic frequency mode-locking with laser diodes through optical pulse train injection," *Photonics Technology Letters, IEEE*, vol. 8, pp. 617 –619, may 1996.

[96] C. Boerner, C. Schubert, C. Schmidt, E. Hilliger, V. Marembert, J. Berger, S. Ferber, E. Dietrich, R. Ludwig, B. Schmauss, and H. Weber, "160 gbit/s clock recovery with electro-optical pll using bidirectionally operated electroabsorption modulator as phase comparator," *Electronics Letters*, vol. 39, pp. 1071 – 1073, 10 2003.

[97] O. Kamatani and S. Kawanishi, "Ultrahigh-speed clock recovery with phase lock loop based on four-wave mixing in a traveling-wave laser diode amplifier," *Lightwave Technology, Journal of*, vol. 14, pp. 1757 –1767, aug 1996.

[98] Y. Li, C. Kim, G. Li, Y. Kaneko, R. Jungerman, and O. Buccafusca, "Wavelength and polarization insensitive all-optical clock recovery from 96-gb/s data by using a two-section gain-coupled dfb laser," *Photonics Technology Letters, IEEE*, vol. 15, pp. 590 –592, april 2003.

[99] L. Mutter, V. Iakovlev, A. Caliman, A. Mereuta, A. Sirbu, and E. Kapon, "Phase-locked 1.3 x00b5;m vcsel arrays based on patterned tunnel junction," in *Lasers and Electro-Optics 2009 and the European Quantum Electronics Conference. CLEO Europe - EQEC 2009. European Conference on*, pp. 1 –1, 14-19 2009.

[100] F. Kefelian, S. O'Donoghue, M. Todaro, J. Mclnerney, and G. Huyet, "High repetition rate monolithic passively mode-locked semiconductor quantum-dot laser: Investigation of the locking regimes and the rf linewidth," in *Lasers and Electro-Optics, 2007. CLEO 2007. Conference on*, pp. 1 –2, 6-11 2007.

[101] Intel, *Core i7 Processor*, 2008. http://www.intel.com/products/processor/corei7/index.htm.

[102] IEEE Antenna and Propagation Society International Symposium and USNC/URSI National Radio Science Meeting, *Evolutionary Design of an X-Band Antenna for NASA's Space Technology 5 Mission*, vol. 3, 2004.

[103] M. Jeeradit, J. Kim, B. Leibowitz, P. Nikaeen, V. Wang, B. Garlepp, and C. Werner, "Characterizing sampling aperture of clocked comparators," in *VLSI Circuits, 2008 IEEE Symposium on*, pp. 68–69, June 2008.

[104] M. Jeeradit, J. Kim, B. Leibowitz, P. Nikaeen, V. Wang, B. Garlepp, and C. Werner, "Characterizing sampling aperture of clocked comparators," in *VLSI Circuits, 2008 IEEE Symposium on*, pp. 68 –69, june 2008.

[105] D.-H. Kim, J. del Alamo, J.-H. Lee, and K.-S. Seo, "Performance evaluation of 50 nm in0.7ga0.3as hemts for beyond-cmos logic applications," *Electron Devices Meeting, 2005. IEDM Technical Digest. IEEE International*, pp. 767–770, Dec. 2005.

[106] G. Konstadinidis, M. Rashid, P. Lai, Y. Otaguro, Y. Orginos, S. Parampalli, M. Steigerwald, S. Gundala, R. Pyapali, L. Rarick, I. Elkin, Y. Ge, and I. Parulkar, "Implementation of a third-generation 16-core 32-thread chip-multithreading sparcsÂő processor," *Solid-State Circuits Conference, 2008. ISSCC 2008. Digest of Technical Papers. IEEE International*, pp. 84–597, Feb. 2008.

[107] C. Kromer, G. Sialm, T. Morf, M. Schmatz, F. Ellinger, D. Erni, and H. Jackel, "A low-power 20-ghz 52-db-ohm transimpedance amplifier in 80-nm cmos," *Solid-State Circuits, IEEE Journal of*, vol. 39, pp. 885–894, June 2004.

[108] C. Kromer, G. Sialm, T. Morf, M. Schmatz, F. Ellinger, D. Erni, and H. Jackel, "A low-power 20-GHz 52-dB-Ohm transimpedance amplifier in 80-nm CMOS," *JSSC*, vol. 39, pp. 885–894, June 2004.

[109] B. Lee, B. Small, Q. Xu, M. Lipson, and K. Bergman, "Characterization of a 4 ?4 gb/s parallel electronic bus to wdm optical link silicon photonic translator," *Photonics Technology Letters, IEEE*, vol. 19, pp. 456–458, April1, 2007.

[110] W. Lee, "Wimax system parameters," in *LGE*, LG Electronics, March 2006.

[111] G. Li, X. Zheng, J. Lexau, Y. Luo, H. Thacker, T. Pinguet, P. Dong, D. Feng, S. Liao, R. Shafiiha, and et al., "Ultralow-power silicon photonic interconnect for high-performance computing systems," *Proceedings of SPIE*, vol. 7607, no. Optoelectronic Interconnects and Component Integration IX, pp. 760703–760703–15, 2010.

[112] M. Lipson, "Guiding, modulating, and emitting light on silicon-challenges and opportunities," *Lightwave Technology, Journal of*, vol. 23, pp. 4222–4238, Dec. 2005.

[113] B. Little and S. Chu, "Microring resonators for very large scale integrated photonics," *Lasers and Electro-Optics Society 1999 12th Annual Meeting. LEOS '99. IEEE*, vol. 2, pp. 487–488 vol.2, 1999.

[114] e. a. Long Chen, "High performance germanium photodetectors integrated on submicron silicon waveguides by low temperature wafer bonding," *Optics Express*, vol. 16(15), 2008.

[115] S. Mann, M. Georgas, and R. Janzen, "Water jets as pixels: Water fountains as both sensors and displays," *Multimedia, 2006. ISM'06. Eighth IEEE International Symposium on*, pp. 766–772, Dec. 2006.

[116] e. a. Mathieu Rouviere, "Integration of germanium waveguide photodetectors for intrachip optical interconnects," *Optics Engineering*, vol. 44(7), 2005.

[117] K. K. Moez, *Design of CMOS Distributed Amplifiers for Broadband and Wireless Communication Applications*. PhD thesis, University of Waterloo, 2006.

[118] S. Naffziger, G. Colon-Bonet, T. Fischer, R. Riedlinger, T. Sullivan, and T. Grutkowski, "The implementation of the itanium 2 microprocessor," *Solid-State Circuits, IEEE Journal of*, vol. 37, pp. 1448 - 1460, nov 2002.

[119] S. Naffziger, B. Stackhouse, T. Grutkowski, D. Josephson, J. Desai, E. Alon, and M. Horowitz, "The implementation of a 2-core, multi-threaded itanium family processor," *Solid-State Circuits, IEEE Journal of*, vol. 41, pp. 197 - 209, jan. 2006.

[120] A. Narasimha, B. Analui, Y. Liang, T. Sleboda, S. Abdalla, E. Balmater, S. Gloeckner, D. Guckenberger, M. Harrison, R. Koumans, D. Kucharski, A. Mekis, S. Mirsaidi, D. Song, and T. Pinguet, "A fully integrated 4 ?10-gb/s dwdm optoelectronic transceiver implemented in a standard 0.13 um cmos soi technology," *Solid-State Circuits, IEEE Journal of*, vol. 42, pp. 2736–2744, Dec. 2007.

[121] I. O'Connor, F. Tissafi-Drissi, D. Navarro, F. Mieyeville, F. Gaffiot, J. Dambre, M. de Wilde, D. Stroobandt, and M. Briere, "Integrated optical interconnect for on-chip data transport," *Circuits and Systems, 2006 IEEE North-East Workshop on*, pp. 209–209, June 2006.

[122] J. Orcutt, A. Khilo, M. Popovic, C. Holzwarth, B. Moss, H. Li, M. Dahlem, T. Bonifield, F. Kartner, E. Ippen, J. Hoyt, R. Ram, and V. Stojanovic, "Demonstration of an electronic photonic integrated circuit in a commercial scaled bulk cmos process," *Lasers and Electro-Optics, 2008 and 2008 Conference on Quantum Electronics and Laser Science. CLEO/QELS 2008. Conference on*, pp. 1–2, May 2008.

[123] F. Paillet and T. Karnik, "Low power and noise tolerant 20 gb/s cmos tia for short-distance optical interconnect," in *Mixed-Signal Design, 2003. Southwest Symposium on*, pp. 49–53, Feb. 2003.

[124] S. Palermo, A. Emami-Neyestanak, and M. Horowitz, "A 90 nm cmos 16 gb/s transceiver for optical interconnects," *Solid-State Circuits, IEEE Journal of*, vol. 43, pp. 1235–1246, May 2008.

[125] J. Polleux and C. Rumelhard, "Optical absorption coefficient determination and physical modelling of strained SiGe/Si photodetectors," in *High Performance Electron Devices for Microwave and Optoelectronic Applications, 8th IEEE International Symposium on*, pp. 167 –172, 2000.

[126] D. M. Pozar, *Microwave Engineering, 3rd Ed.* John Wiley & Sons, Inc., 2005.

[127] A. Rylyakov, C. Schow, B. Lee, W. Green, J. Van Campenhout, M. Yang, F. Doany, S. Assefa, C. Jahnes, J. Kash, and Y. Vlasov, "A 3.9ns 8.9mw 4x4 silicon photonic switch hybrid integrated with cmos driver," in *ISSCC*, pp. 222 –224, feb. 2011.

[128] NASA/DoD Conference of Evolution Hardware, *An Evolvable Antenna Platform Based on Reconfigurable Reflectarrays*, 2005.

[129] J. Sauer, D. Blumenthal, and A. Ramanan, "Photonic interconnects for gigabit multicomputer communications," *LTS, IEEE*, vol. 3, pp. 12–19, Aug 1992.

[130] D. Schinkel, E. Mensink, E. Kiumperink, E. van Tuijl, and B. Nauta, "A double-tail latch-type voltage sense amplifier with 18ps setup–hold time," *Solid-State Circuits Conference, 2007. ISSCC 2007. Digest of Technical Papers. IEEE International*, pp. 314–605, Feb. 2007.

[131] C. Schow, L. Schares, S. Koester, G. Dehlinger, R. John, and F. Doany, "A 15-gb/s 2.4-v optical receiver using a ge-on-soi photodiode and a cmos ic," *Photonics Technology Letters, IEEE*, vol. 18, pp. 1981–1983, Oct.1, 2006.

[132] D. Shaeffer and T. Lee, "A 1.5-v, 1.5-ghz cmos low noise amplifier," *IEEE Journal of Solid-State Circuits*, vol. 32, pp. 745–759, May 1997.

[133] e. a. Shijun Xiao, "Compact silicon microring resonantors with ultra-low propagation loss in the c band.," *Optics Express*, p. 15(22), 2007.

[134] K.-T. Shiu, S. Agashe, and S. Forrest, "A simple monolithically integrated optical receiver consisting of an optical preamplifier and a p-i-n photodiode," *Photonics Technology Letters, IEEE*, vol. 18, pp. 956–958, April 2006.

[135] V. Stojanovic, V. Oklobdzija, and R. Bajwa, "Comparative analysis of latches and flip-flops for high-performance systems," in *Computer Design: VLSI in Computers and Processors, 1998. ICCD '98. Proceedings. International Conference on*, pp. 264–269, Oct 1998.

[136] e. a. T. Barwicz, "Three-dimensional analysis of scattering losses due to sidewall roughness in microphotonic waveguides," *Journal of Lightwave Technology*, vol. 23(9), 2005.

[137] e. a. Tao Yin, "31ghz ge n-i-p waveguide photodetectors on silicon-on-insulator substrate," *Optics Express*, vol. 44(7), 2005.

[138] Y. Vlasov, W. Green, S. Assefa, J. van Campenhout, Y.-H. Kim, and F. Xia, "Silicon integrated nanophotonics for on-chip optical interconnects," *Group IV Photonics, 2008 5th IEEE International Conference on*, pp. 221–221, Sept. 2008.

[139] e. a. Yiming Li, "Process-variation-and-random-dopants-induced threshold voltage fluctuations in nanoscale cmos and soi devices," *Microelectronic Engineering*, vol. 84, 2007.

[140] I. Young, E. Mohammed, J. Liao, A. Kern, S. Palermo, B. Block, M. Reshotko, and P. Chang, "Optical I/O technology for tera-scale computing," in *ISSCC*, pp. 468 – 469,469a, feb. 2009.

[141] I. Young, E. Mohammed, J. Liao, A. Kern, S. Palermo, B. Block, and P. Reshotko, M. Chang, "Optical i/o technology for tera-scale computing," *International Solid-State Circuits Conference*, pp. 468–469, 2009.

[142] I. Young, E. Mohammed, J. Liao, A. Kern, S. Palermo, B. Block, M. Reshotko, and P. Chang, "Optical i/o technology for tera-scale computing," *Solid-State Circuits, IEEE Journal of*, vol. 45, pp. 235 –248, jan. 2010.

[143] Y. Zhao, "Optimal linear transformation of space-time block coding with channel covariance feedback," Master's thesis, University of Toronto, 2003.

[144] E. Alon, V. Stojanovic, and M. Horowitz, "Circuits and techniques for high-resolution measurement of on-chip power supply noise," *Solid-State Circuits, IEEE Journal of*, vol. 40, pp. 820 – 828, april 2005.

[145] S. Assefa, F. Xia, W. Green, C. Schow, A. Rylyakov, and Y. Vlasov, "Cmos-integrated optical receivers for on-chip interconnects," *Selected Topics in Quantum Electronics, IEEE Journal of*, vol. 16, pp. 1376 –1385, sept.-oct. 2010.

[146] A. Emami-Neyestanak, D. Liu, G. Keeler, N. Helman, and M. Horowitz, "A 1.6 gb/s, 3 mw cmos receiver for optical communication," *VLSI Circuits Digest of Technical Papers, 2002. Symposium on*, pp. 84–87, 2002.

[147] S. Goswami, J. Silver, T. Copani, W. Chen, H. Barnaby, B. Vermeire, and S. Kiaei, "A 14mw 5gb/s cmos tia with gain-reuse regulated cascode compensation for parallel optical interconnects," in *Solid-State Circuits Conference - Digest of Technical Papers, 2009. ISSCC 2009. IEEE International*, pp. 100 –101,101a, feb. 2009.

[148] J.-S. Kim, C. S. Oh, H. Lee, D. Lee, H.-R. Hwang, S. Hwang, B. Na, J. Moon, J.-G. Kim, H. Park, J.-W. Ryu, K. Park, S.-K. Kang, S.-Y. Kim, H. Kim, J.-M. Bang, H. Cho, M. Jang, C. Han, J.-B. Lee, K. Kyung, J.-S. Choi, and Y.-H. Jun, "A 1.2V 12.8GB/s 2Gb mobile wide-I/O DRAM with 4x128 I/Os using TSV-based stacking," in *ISSCC*, pp. 496 –498, feb. 2011.

[149] F. Liu, D. Patil, J. Lexau, P. Amberg, M. Dayringer, J. Gainsley, H. Moghadam, X. Zheng, J. Cunningham, A. Krishnamoorthy, E. Alon, and R. Ho, "10 gbps, 530 fj/b optical transceiver circuits in 40 nm cmos," in *VLSI Circuits (VLSIC), 2011 Symposium on*, pp. 290 –291, june 2011.

[150] S. Mukhopadhyay, R. Joshi, K. Kim, and C.-T. Chuang, "Variability analysis for sub-100nm PD/SOI sense-amplifier," *ISQED*, pp. 488–491, March 2008.

[151] A. Narasimha, B. Analui, Y. Liang, T. Sleboda, and C. Gunn, "A fully integrated 4Ã£10gb/s dwdm optoelectronic transceiver in a standard 0.13 mu;m cmos soi," in *Solid-State Circuits Conference, 2007. ISSCC 2007. Digest of Technical Papers. IEEE International*, pp. 42 –586, feb. 2007.

[152] S. Palermo, A. Emami-Neyestanak, and M. Horowitz, "A 90 nm cmos 16 gb/s transceiver for optical interconnects," *Solid-State Circuits, IEEE Journal of*, vol. 43, pp. 1235–1246, May 2008.

[153] K.-L. Wong and C.-K. Yang, "Offset compensation in comparators with minimum input-referred supply noise," *JSSC*, vol. 39, pp. 837 – 840, may 2004.

[154] S.-H. Woo, H. Kang, K. Park, and S.-O. Jung, "Offset voltage estimation model for latch-type sense amplifiers," *Circuits, Devices Systems, IET*, vol. 4, pp. 503 –513, nov 2010.

[155] J. S. Yun, M. Seo, B. Choi, J. Han, Y. Eo, and S. M. Park, "A 4gb/s current-mode optical transceiver in 0.18um cmos," in *Solid-State Circuits Conference - Digest of Technical Papers, 2009. ISSCC 2009. IEEE International*, pp. 102 –103, feb. 2009.

[156] A. Joshi *et al.*, "Silicon-photonic clos networks for global on-chip communication," in *Proceedings of NoCS '09*, p. 91, may 2009.

[157] R. J. Riedlinger, R. Bhatia, L. Biro, B. Bowhill, E. Fetzer, P. Gronowski, and T. Grutkowski, "A 32nm 3.1 billion transistor 12-wide-issue Itanium; processor for mission-critical servers," in *ISSCC '11*, pp. 84 –86, feb. 2011.

[158] G. Kurian, J. E. Miller, J. Psota, J. Eastep, J. Liu, J. Michel, L. C. Kimerling, and A. Agarwal, "ATAC: a 1000-core cache-coherent processor with on-chip optical network," in *Proceedings of PACT '10*, (New York, NY, USA), pp. 477–488, ACM, 2010.

[159] S. Beamer, C. Sun, Y.-J. Kwon, A. Joshi, C. Batten, V. Stojanović, and K. Asanović, "Re-architecting DRAM memory systems with monolithically integrated silicon photonics," in *Proceedings of ISCA '10*, (New York, NY, USA), pp. 129–140, ACM, 2010.

[160] D. Vantrease, R. Schreiber, M. Monchiero, M. McLaren, N. P. Jouppi, M. Fiorentino, A. Davis, N. Binkert, R. G. Beausoleil, and J. H. Ahn, "Corona: System implications of emerging nanophotonic technology," in *Proceedings of ISCA '08*, (Washington, DC, USA), pp. 153–164, IEEE Computer Society, 2008.

[161] C. Debaes, A. Bhatnagar, D. Agarwal, R. Chen, G. Keeler, N. Helman, H. Thienpont, and D. Miller, "Receiver-less optical clock injection for clock distribution networks," *Selected Topics in Quantum Electronics, IEEE Journal of*, vol. 9, pp. 400–409, March-April 2003.

[162] A. W. Topol, D. C. L. Tulipe, L. Shi, D. J. Frank, K. Bernstein, S. E. Steen, A. Kumar, G. U. Singco, A. M. Young, K. W. Guarini, and M. Ieong, "Three-dimensional integrated circuits," *IBM Journal of Research and Development*, vol. 50, pp. 491–506, July 2006.